Universiteit Gent
Faculteit Ingenieurswetenschappen en Architectuur
Vakgroep Elektronica en Informatiesystemen
Vakgroep Informatietechnologie

Light Absorption Enhancement and Electronic Properties of Thin-Film Solar Cells

Versterking van lichtabsorptie en elektronische eigenschappen van dunnefilmzonnecellen

---

Aimi Abass

Proefschrift ingediend tot het behalen van de graad van
Doctor in de Ingenieurswetenschappen:
Toegepaste Natuurkunde
Academiejaar 2013-2014

Universiteit Gent
Faculteit Ingenieurswetenschappen en Architectuur
Vakgroep Elektronica en Informatiesystemen
Vakgroep Informatietechnologie

Promotors:

Prof. Bjorn Maes	University of Mons, Ghent University
Prof. Marc Burgelman	Ghent University

Examination Committee:

Prof. Jan Van Campenhout (Voorzitter)	Ghent University
Prof. Bjorn Maes (Promotor)	University of Mons, Ghent University
Prof. Marc Burgelman (Promotor)	Ghent University
Dr. Ounsi El Daif	Qatar Environment and Energy Research Institute
Dr. Branko Kolaric	University of Mons
Prof. Jeroen Beeckman	Ghent University
Prof. Zeger Hens	Ghent University

Universiteit Gent
Faculteit Ingenieurswetenschappen en Architectuur

Vakgroep Elektronica en Informatiesystemen
Vakgroep Informatietechnologie
Sint Pietersnieuwstraat 41, B-9000 Gent, België

Tel.: +32-9-331.49.00
Fax.: +32-9-331.48.99

This work was supported by the IWT Institute for the Promotion of Innovation by Science and Technology in Flanders via the SBO project SiLaSol

Dankwoord

I have been greatly blessed during the past four years of my PhD with the opportunity to know personally, work with, and learn from most likely the best set of friends, colleagues and promotors a PhD student can ever wish for. I will not, even for a second, trade the time I have spent in Gent University to be in any other institute (except for the fact that VUB has better cafeteria). In these front pages of my PhD book, I shall endeavor to describe those who I wholeheartedly wish to acknowledge and thank.

I am deeply indebted to my promotor Bjorn Maes. His guidance, patience, deep reservoir of photonics knowledge, relentless support, and more patience allowed me to reach where I am today. I greatly appreciate his trust in me and all the computing arsenal I was entrusted with. I am very thankful how graciously he responded to a bachelor student from Indonesia who mistakenly applied for a PhD position 6-7 years ago. And also, how he is always willing to discuss ideas of mine (with great patience) no matter how silly it turned out to be. It is truly great privilege for me to be a student under his supervision.

I would like to express my deepest appreciation and gratitude to my other promotor Marc Burgelman who shared so much of his knowledge, experience, stories, and a great collection of dutch proverbs with great humor and passion. I am honored to be his last PhD student. I sincerely hope I was not too big of a last hurdle for him. Studying under Marc was truly inspirational for both my academic and daily life. I will always remember fondly the day he back tracked the waterspoortban to see if I am still alive or not.

To (effectively my third promotor) Samira Khelifi who with great patience shared with me so much of her in depth knowledge of semiconductors and taught me almost everything I know about the measurement setups and the electrical part of solar cells: Thank you so very much for all time youve spent answering my questions, looking at my unphysical SCAPS def files that are sometimes unrelated to your project, and sharing your wise perspective on so many things. It was truly a great privilege to learn from you these past four years. Thank you also for the nutritional supplements you always generously provide for the office.

I have the wonderful opportunity to work with great people who I wish to acknowledge here. Special thanks to my good friend Said Rahimzadeh Kalaleh Rodriguez whom I have the great honor to work with in several projects. I wish

to thank him and his other half Marina for all the inspiring and great scientific and also nonscientific interactions we had. My thanks to Jaime Gómez Rivas, Christos Trompoukis, Sven Leyre, Khai Quang Le, Jan Deckers, Erki Karber, Zeger Hens, Tangi Aubert, Jeroen Beeckman and Thomas Ako. I have learned so much from them during the time we have worked together and it was truly a great pleasure for me.

I wish to also thank my PhD jury members: Zeger Hens, Jeroen Beeckman, Ounsi El Daif, Branko Kolaric, Jan Van Campenhout. for the time they took to read and judge my PhD work. Their suggestions and questions made it possible for me to improve my thesis even further.

I have aIso been surrounded by what I think to be the best colleagues one can wish for in an office. I wish to thank Stefan for the warmth of his friendship, great humor, advices, and his stack of chili sauce and good wine which he always shared ever so generously. I must thank him also for sharing his latex, linux and GIMP knowledge with me. I thank Koen (the great-outdoor-window-always-opened guy) for the helpful discussions and assisting me with the measurement setup, SCAPS, the ever so wonderful plot it all (PIA). It was a great boost for me in the start of my PhD. I wish to thank Toon whom I almost continuously annoyed for the past 4 years. Thank you for your great friendship and all the interesting discussion we had, and also for effectively helping me in my diet. I wish to solemnly thank John for his cheerful bright mood, the biryani, his sincere brotherhood, and sharing his great knowledge of device fabrication and the biriyani. I want to thank Filip Strubbe for being the new best office mate ever whom I wished would have moved even earlier. I express my gratitude to Glenn for sharing the glories of the most wonderful city in Belgium: Geraardsbergen (home of the mattentaart), carrots, dark chocolates, and all the interesting scientific banters. To Caspar and Stijn, thank you for the daily friendly banters, the nice discussions, and the cookies. I hope you two will like the new mousepad, if the cover goes out you could still use one of the 182 spare surfaces. Special thanks to Woesty who kindly provided me valuable advice for the thesis writing and presentation, and supplied honey. I wish to thank Marnix Vermassen for his continuing assistance, support and friendship. I truly appreciate his readiness to help even during his busy times. My thanks to Muriel for patiently helping me with the printing of my thesis book and all the administration for my PhD defense. I wish to also thank Filip Beurnis, Patrick, Kristiaan (for all the Christmas cookies), Jeroen, Alex (for somehow inspiring me to finish the last exploot run) , Tom, Manoj, Inge, Michel (chili loving and effectively irish), Oksana, Masoumeh, Varsenik, Oliver (blue phase-latex-DnD guru), Yi, Muhammad (for the Iranian delicacies), and Lieven. The office/lab is a brighter place with these people around.

I have also been blessed with the great support from outside the university. I wish to express my deepest gratitude to the International Church Community of Ghent for being a second family for me. My special thanks to my fellow ICCG brothers and sisters: the great gaming Decans (Geoffrey and Kseniya), the loving Dros (Pieter and Mariale and PA and Santiago), The very warm and dear to my heart Proots (su-chef/pastor Leo and chef Anneke) who has been with me through

so many good and bad times, The awesome Maertens (Willem and Inge), the cool Dunsters (Cole and Jenny and Cameron and Harrison and Barbara mcferrin(to be revised)), the wonderful Strobbes (Karel and Elke), the hip Hutapeas (Lenny and Wira), the kind Kiteyis(Fragrance and Peter), the impeccable Reibeiros (Antonio and Giselene) , the magnificent Liras (Victor and Nanda), the other very warm Proots (Tim and Erika), the artistic De craenes(Tom and Naomi), Martine, Janneke, my great friend Bart (game master) and his other half Önnela, the great painter Eyram, Kofi, Jacob, Naomi, Merry, Silviana, Andrew, Jamie, good ol Erik, Peter, Benson, Yhuri, Charry, Donna, the inspiring Rene, Jacobus, Julia, Christine, Lucas, Wagner and so many others. The warmth and sincere friendship you all brought to my life was truly a blessing for me. I cannot ask for better extended family members. My thanks to the Kusmanto family (Juliando, Lanny, Aswin and Hans) and the Djudzmans (Ann and Francis) for their ever so kind nature and for always being willing to lend an ear and help (and invite for dinner). My gratitude also to the people in the Indonesian student association for all the fun times we had. Special thanks to Pande, Arima, Arifin, and Kiki rita for their wonderful friendship. To the best brazilian scientist I've ever known Emiliano, best armenian scientist Tigran, and best svenska scientist Wondwosnt, I thank you for all the inspiring and warm discussions and also strong camaraderie. I always learn a thing or two each time I chat with you.

I wish to thank my family for the strong love they gave me. I thank my mother and father who have always supported me in every way they can. I thank especially my brother for flying in just to see a 20 minute presentation of mine and for the red computational ferarri of a laptop that I carry around with great pride. I hope to continue to make these people proud.

To my dearly beloved Magda Xanthina who made my life more full and joyful: thank you for your prayers, for bearing my burdens with me, for all the loving support through the tough times and being such a sunshine that motivates me to go on.

I truly thank God for the many blessings, guidance and joy throughout the 4 years of the PhD.

Ghent, September 1 2014
Aimi Abass

Table of Contents

List of Acronyms

A

a-Si	Amorphous Silicon
AM 1.5G	The Air Mass 1.5 G condition (for terrestrial solar spectrum measurement)
AFM	Atomic Force Microscopy
AC	Alternating Current
AIC	Aluminum Induced Crystallization

B

BZ	Brillouin Zone
BSF	Back Surface Field
BSDF	Bidirectional scattering distribution function

C

c-Si	Crystalline silicon
C-V	Capacitance Voltage measurement
C-f	Capacitance frequency measurement

D

DIG	Dual Interface Gratings

E

EM	Electromagnetic

F

FSF	Front Surface Field
FEM	Finite Element Method
FC	Fully Coherent

H

HIT	Heterojunction with Intrinsic Thin layer

I

ITO	Indium Tin Oxide

L

LDOS	Local Density Of States
LSPR	Localized Surface Plasmon Resonance
LC	Liquid Crystal
LED	Light Emitting Diode
LIC	Laser Induced Crystallization

M

MPP	Maximum Power Point
MIA	Measure-It-All, in-house solar cell measurement programme at ELIS, developed by Johan Verschraegen.

N

NW	Nanowire

O

OPC	One Pass Coherent

P

poly-Si	Polycrystalline Silicon
PIA	Plot-It-All, in-house software tool for the interpretation of C-f-T mesurements and admittance Analysis, developed at ELIS by Koen Decock.
PML	Perfectly Matched Layer
PLE	Photoluminescence Enhancement
PECVD	Plasma-Enhanced Chemical Vapor Deposition

Q

Q-factor	Quality factor
QNR	Quasi Neutral Region
QD	Quantum Dot

R

RA	Rayleigh Anomaly

S

SLR	Surface Lattice Resonance

SCL	Space Charge Layer
SILAR	Successive Ion Layer Absorption and Reaction
SRH	Shockley-Read-Hall
SPP	Surface Plasmon Polariton

T

TE	Transverse Electric
TM	Transverse Magnetic
TEM	Transverse Electric Magnetic
TIR	Total Internal Reflection

U

UV	Ultra Violet

W

WPP	Waveguide Plasmon Polariton
WIR	Weighted Integrated Reflection

List of Symbols

Symbol	Description	Units
A	Area	cm^2
A_{tot}	Total absorption	-
A_{first}	First pass absorption	-
B	Magnetic induction	T
σ	Carrrier capture cross-section	cm^2
c	Speed of light	m/s
c_0	Speed of light in vacuum	2.998×10^8 m/s
C_j	Junction capacitance	nF
D	Electric displacement field	C/m^2
d	Thickness	μm
D	Diffusion constant	μm/s
ϵ	permittivity	F/m
ϵ_0	Vacuum permittivity	8.854×10^{-12} F/m
e	Electron charge	1.602×10^{19} C
E	Electric field	V/m^{-1}
$E_{x,y,z}$	(x,y,z)-component of electric field	V/m^{-1}
E	Energy	eV
E_g	Band gap energy	eV
EQE	External quantum efficiency	-
f	Frequency	Hz
FF	Fill Factor	-
ϕ_c	Phase shift	-
G	Grating vector component	rad/μm
g	Grain size	μm
H	Magnetic field	
$H_{x,y,z}$	(x,y,z)-component of magnetic field	V/m^{-1}
h	Planck constant	4.135×10^{15} eV s
$\hbar$	Reduced Planck constant $h/2\pi$	6.582×10^{16} eV s

Symbol	Description	Units
$I_{overlap}$	Overlap integral	-
J	current density	mA/cm^2
J	Short circuit current density	mA/cm^2
J_{sc}	Short circuit current density	mA/cm^2
J_L	Light current	mA/cm^2
J_0	Diode saturation current	mA/cm^2
k	Wave vector	rad/μm
$\mathbf{k}_G$	Grating wave vector	rad/μm
$k_{//}$	In plane wave vector component	rad/μm
k_{guided}	Wave vector component in the guiding direction	rad/μm
k_t	Transversal wave vector component	rad/μm
k_0	Vaccuum wave vector $2\pi/\lambda_0$	rad/μm
k	Boltzmann constant	8.617×10^5 eV/K
L	Diffusion length	μm
L_{mono}	Effective monocrystalline diffusion length	μm
L_{poly}	Effective polycrystalline diffusion length	μm
λ	Wavelength	nm
λ_0	Free space wavelength	nm
μ	Permeability	H/m
μ_0	Vacuum permeability	$4\pi \times 10^{-7}$ H/m
n	Refractive index	-
$n_{cladding}$	Cladding refractive index	-
n_{core}	Core refractive index	-
n_e	Electron Concentration	cm^{-3}
n_h	Hole Concentration	cm^{-3}
$N_{D,A}$	Donor/Acceptor doping concentration	cm^{-3}
N_t	Trap state concentration	cm^{-3}
$N_{c,v}$	Conduction/Valence band density of states	cm^{-3}
ω	Radial frequency $2\pi f$	Hz
ω_{esc}	Attempt to escape frequency	Hz
p	Momentum	kg m/s
P	Period	nm
q	Electron charge	1.602×10^{19} C
ρ_V	Volumetric free charge density	C/cm^{-3}
r	Position	m
R_{tot}	Total reflection	-
R_{first}	First pass reflection	-
R_s	Series resistance	Ω
R_{sh}	Shunt resistance	Ω
R_{sq}	Sheet resistance	Ω

Symbol	Description	Units
S	Poynting vector	W/cm^2
S_b	Contact recombination velocity	cm/s
S_{GB}	Grain boundary recombination velocity	cm/s
τ	Life time	s
t	Time	s
T	Temperature	K
T_c	Critical temperature	K
T_{tot}	Total transmittance	-
T_{first}	First pass transmittance	-
$\tilde{u}_{ext}$	External applied voltage	Volts
V_{oc}	Open circuit voltage	Volts
$q\tilde{u}_{p,n}$	Local shift of the quasi-Fermi level as a response to an ac-voltage signal	eV
V_t	Thermal voltage	Volts
V_{mpp}	Maximum power point voltage	Volts
V_{bi}	Built in voltage	Volts
w	width	μm
ζ	Ideality factor	
x	x-position	μm
y	y-position	μm
z	z-position	μm

Nederlandse samenvatting –Summary in Dutch–

Zonnecellen genereren elektrisch vermogen via foton-absorptie. Voor een duurzame toekomst in een wereld met een groeiende energie-vraag wordt de efficiëntie van zonnecellen zeer belangrijk om het grote vermogen van de zon te gebruiken. Echter, een hoge efficiëntie is nutteloos wanneer de kosten te hoog zijn. Voor deze combinatie van lage kosten en hoge efficiëntie wordt veel onderzoek verricht naar:

1. het bereiken van een sterke absorptie met weinig materiaal,
2. het identificeren en gebruiken van goedkopere, geschikte materialen.

Met betrekking tot het eerste punt bieden nano-structuren belangrijke mogelijkheden, daar ze sterk geoptimaliseerd kunnen worden voor een optimale lichtabsorptie.

Veel verschijnselen kunnen de absorptie verhogen, zoals verstrooiing, antireflectie via Fabry-Perot modes of graduele index-variaties, diëlektrische of plasmonische modes enzoverder. Vaak echter zorgt de optimale excitatie van het ene verschijnsel voor een vermindering van het andere. Het is zelfs moeilijk om hetzelfde verschijnsel over een breed golflengte-gebied te gebruiken. Om deze problemen te verbeteren stellen we dubbele interface-roosters voor (dual interface gratings, DIGs) en combinaties met diffuse reflectoren. De eerste methode gebruikt de excitatie van geleide modes, terwijl de tweede het gebruik van anti-reflectie en diffusie optimaliseert. In deze structuren wordt de werking van de verscheidene componenten opgesplitst, zodat ze meer flexibel kunnen samenwerken.

Verschillende variaties van dubbele interface-roosters worden onderzocht. Een belangrijke uitdaging is het bereiken van een rijk Fourierspectrum, terwijl de geometrie niet te complex wordt. Hiervoor stellen we DIGs voor met meerdere periodes, zodat koppeling met hoge- en lage-orde modes efficiënt verloopt. Verder bestuderen we het effect van asymmetrie (blazing), hetgeen de excitatie van nog meer modes mogelijk maakt, zonder andere golflengtes of invalshoeken te benadelen.

Om combinaties van roosters met diffuse reflectoren te bestuderen, ontwikkelen we een rekenmethode (one-pass coherent, OPC), die men voor een grote klasse van structuren kan gebruiken. De OPC-methode gebruikt golfberekeningen voor het rooster, terwijl de diffuse reflector via een vereenvoudigd lichtstralen-model gesimuleerd wordt, hetgeen zorgt voor een beperkt rekendomein.

Met de OPC-methode tonen we aan dat beperkte coherentie kan leiden tot een gemiddeld sterkere absorptie dan voor perfect coherent licht. Bij perfecte coherentie kan men koppelen naar quasi-geleide modes die zorgen voor een sterkere absorptie. Deze verzameling resonanties werkt echter over een beperkt golflengtegebied, en voor de niet-resonante gebieden verkrijgt men een vermindering van absorptie. Dientengevolge, voor bepaalde materiaal-diktes kan incoherent licht een gemiddeld grotere efficiëntie verwezenlijken. Hiervoor spelen tevens de eigenschappen van de diffuse reflector een belangrijke rol. In de structuren met zowel roosters als diffuse reflectoren tonen we aan dat beide elementen kunnen samenwerken, wanneer bepaalde criteria voldaan zijn.

Een gerelateerd onderdeel van het werk behelst de versterking van licht-emissie via plasmonische of metallische elementen. Versterkte emissie kan bijvoorbeeld nuttig zijn voor een volgende generatie zonnecellen die gebruik maken van conversie van golflengtes (up/down-conversion). Daarnaast heeft men aangetoond dat een efficiënte zonnecel eveneens een efficiënte emitter moet zijn, hetgeen betekent dat niet-radiatieve recombinaties geen beperking vormen.

In dit verband bestuderen we zogenaamde hyride plasmonisch-fotonische modes. Verscheidene hybride modes zijn bekend, maar wij werken met periodieke roosters van metallische nanodeeltjes, die een interactie bewerkstelligen tussen de gelokaliseerde plasmon-resonanties (localized surface plasmon resonance) en de diffractiemodes (Rayleigh anomaly). Het hoofddoel is het verkrijgen van een hybride mode die de beste eigenschappen van de oorspronkelijke modes overneemt. Ons doel is vaak het verwerven van een sterk nabije-veld, met toch nog een brede veld-distributie en lage verliezen. Het optimaliseren van deze eigenschappen is zeer nuttig wanneer men een sterke interactie wenst met een bepaald volume absorbers of emitters. We tonen numeriek aan hoe de geometrie bepaalde eigenschappen (dispersie, bandbreedte enz.) kan controleren, en deze resultaten komen overeen met experimenten van medewerkers.

Als een extensie op deze resultaten werkten we mee aan een structuur die de plasmonische deeltjes in contact brengt met twee andere functionele lagen. Aan de ene kant nemen we een laag kwantum-deeltjes (quantum dots, QDs), aan de andere kant werd een laag vloeibare kristallen geplaatst (liquid crystals, LCs). De emissie van de QDs wordt sterk beïnvloed door de koppeling met de plasmonische modes. Zeer interessant is echter dat deze emissie geregeld kan worden door de LCs, daar hun eigenschappen veranderen met de temperatuur. Onze berekeningen tonen aan dat de polarizatie van de modes in dit systeem cruciaal is om de werking te begrijpen.

In parallel met de fotonische eigenschappen van zonnecellen, werken we aan de elektronische eigenschappen, en dit meer specifiek voor dunne-film, polykristallijne silicium (poly-Si) zonnecellen. Dit type cellen heeft potentieel als alternatief voor de traditionele multi- en monokristallijne cellen, maar heeft nog bepaalde structurele en materiaalproblemen. In dit werk bepalen we doelwaarden voor verschillende parameters die nodig zijn om een bepaalde efficiëntie te bereiken. We vinden bijvoorbeeld dat grotere korrelgroottes (meer dan een paar micrometer) niet meer nodig zijn, indien de recombinatie aan de korrelgrenzen binnen de perken bli-

jft. Deze simulaties gebruiken experimenteel relevante korrelgrootte-distributies en netwerk-modellen. Hiermee tonen we aan dat de breedte van de distributie niet zo belangrijk blijkt in de beperking van de efficiëntie.

We verrichten tevens een vergelijkende experimentele studie van poly-Si cellen met p-type en n-type dopering. C-V metingen bestuderen de dopingconcentratie, terwijl C-f-T metingen de defect-niveaus bepalen. Hydrogenatie blijkt de defect-concentratie in de p-type cellen te reduceren. Daarnaast hebben de p-type cellen meer defect-niveaus dan n-type, zodat n-type in dit opzicht potentieel interessant lijkt.

English summary

Solar cells generate electrical power from incoming photon absorption. To maintain a sustainable future under a growing world energy demand, highly efficient solar cells are of great importance. They play a key role in utilizing the immense power from the sun. Having high efficiency solar cells however, is meaningless if the costs are too high. In response to this demand for high efficiency while being economically feasible, much research work is done in parallel on:

1. obtaining strong absorption with as less active material as possible,

2. identifying and utilizing less costly materials suitable for solar cells.

With regards to the first point nanostructures offer key opportunities as they can be tailored to maximize the intensity and transit time of light in the active material to improve absorption.

There are many phenomena that can enhance absorption for example: scattering, antireflection via Fabry-Perot or gradual refractive index transitions, dielectric waveguide modes, and plasmonic based modes. Oftentimes however, the requirements for optimum excitation of one phenomenon can be at the expense of another. Even more troubling, there are already conflicting requirements to excite the same phenomenon in different wavelength ranges. To alleviate these problems we propose the usage of dual interface gratings (DIGs) and diffuser-grating structures. The former enhance absorption by relying on guided mode excitation while the latter focusses on antireflection and scattering management. In such structures, the responsibility of different optical components is split, enabling more flexibility in optimizing each.

Different variants of the dual interface grating structures were explored. One main point of discussion is the light trapping potential of multiperiodic DIGs, which have a rich Fourier spectrum, while maintaining a straightforward geometry. Multiperiodic DIGs can be tailored to give stronger coupling to higher-order guided modes, without sacrificing the coupling efficiency to lower order modes. We further studied the effect of introducing a weak blazing in a triangular DIG system. The weak blazing leads to efficient excitation of more photonic phenomena without sacrificing the absorption at other wavelengths and at larger angles.

To efficiently address combined diffuser-grating structures, we developed the one pass coherent (OPC) calculation method, which can also handle more general structures with other wave and ray optics segments. The OPC calculations take

wave effects into account where they matter the most, while evading a large computational domain to model e.g. rough diffusers or other ray optics component. A general rough diffuser is handled directly via the reflected wavefront instead of its geometry. A single plane wave calculation sweep provides all the information to calculate any kind of bottom diffuser.

With the OPC method, we demonstrate that limited coherence can lead to a stronger absorption on average over a fairly broad wavelength range for an important range of Si thicknesses. A loss of phase relation between incoming waves and waves reflected from the back in effect exchanges a discrete set of leaky waveguide states in the active material film with a broadband continuum of allowable photonic states. Though one loses the strong absorption provided by leaky guided modes at resonant wavelengths, a more broadband absorption enhancement becomes possible and can on average improve the absorption performance. Therefore, the back reflector in advanced thin-film devices needs careful consideration. We proceed to show that combined front grating-back diffuser structures give stronger absorption enhancement than single element devices in an important range of active material thicknesses.

Another part of our work is in the context of plasmonic light emission enhancement. Emission enhancement is also a point of interest for solar cell applications as it can be used to improve photon up/down conversion processes that may be employed to tailor the spectrum of incoming photons and to potentially utilize solar radiation in a more efficient manner. Furthermore, a solar cell which reaches the Shockley-Queisser operation limit should also behave as a very efficient LED at open circuit voltage, indicating that it is not limited by non-radiative recombination processes.

In this work, we expand upon a novel approach to overcome the challenges in plasmonic light-matter interaction enhancement that was introduced recently utilizing hybrid plasmonic-photonic modes. The hybrid modes we focus on arise in metallic nanoantenna arrays from the interaction between the localized surface plasmon resonance (LSPR) of the individual nanoparticles and the Rayleigh anomaly (RA) diffraction or waveguide mode. The main point of interest of these hybrid modes is the possibility to mix desirable attributes of the different interacting bare resonances can be mixed in the hybrid resonance. One can in effect have a mode with a relatively strong near field enhancement while maintaining an extended field distribution and low loss. A hybrid mode with such characteristics is of great interest when one wishes to enhance and control the emission of a volumetric distribution of emitters. The dispersion, linewidth, and associated stop-gap of a hybrid plasmonic-photonic mode are demonstrated here to be widely tunable by controlling the energy detuning between the interacting bare resonances. This energy detuning can be controlled through the geometry of the nanoantennas.

In a side step from the solar cell application, we further proceed to demonstrate active tuning of the emission enhancement resonant wavelength and directionality provided by a hybrid plasmonic-photonic mode. The hybrid mode in question arises from the interaction between a thin quantum dot (QD) layer film with an aluminum nanodisk array placed on top of the layer. This system supports ra-

diative coupling between the LSPR of each nanodisk and a waveguide mode in the quantum dot emitter layer which resulted in the hybrid mode. The tunability was achieved by covering the array with liquid crystal (LC) molecules whose orientation can be tuned via a voltage or temperature change. By controlling the LC molecule orientation, one can thus control the refractive index of the LC layer. The dispersion, linewidth, and excitation strength of this hybrid mode are all affected by the LC molecule orientation, which we control via temperature. We show that the tuning depends on the relative orientation of the dominant mode polarization with the LC optical axis.

Having investigated various light management schemes that can enhance solar cells, we examine the limiting factors which hinder efficient current extraction from polycrystalline silicon thin-film solar cells of a few micrometers thick. Thin-film polycrystalline silicon (poly-Si) solar cells have much promise as an economical alternative to multi- and monocrystalline wafer based cells. However, structural deficiencies still limit the performance of these poly-Si cells. Here, we provide target values for recombination parameters and grain size that should be met to obtain the desired cell efficiency. It is found that, with grain boundary recombination velocity $S_{GB} \leq 10^4$ cm/s, achieving a larger grain size beyond several μm in diameter does not bring a significant benefit. Simulations of cells with exponential grain diameter distributions and realistic recombination parameters were done through network modelling to examine the performance of each individual grain under nonhomogeneous conditions. Our results show that grain size inhomogeneity is not expected to severely limit the solar cell efficiency.

A comparative experimental study between thin-film poly-Si cells with boron doped p-type and arsenic doped n-type absorber layer was also done. C-V measurements were performed to study the apparent doping concentration of the samples. C-f-T measurements were subsequently used to deduce the defect density distribution in both samples. Hydrogenation is found to be able to reduce the defect concentration in the p-type absorber cells. The p-type absorber cells exhibit more defect states than n-type thin poly-Si films. Judging from the type of observed defect states alone, n-type absorbers may carry more promise than p-type absorbers.

1 Introduction

1.1 Introduction

In recent decades, advancement in fabrication technology has reached a stage where it is possible to control the structure of various important materials down to the nanoscale regime ($< 1\mu$m) for large scale practical purposes [1–4]. This paves the way for myriads of new electronic and photonic devices and also gives opportunities to further enhance existing devices. As a result a stimulating atmosphere develops, sparking global research efforts on various novel nanostructures which often reveal useful phenomena relevant for different applications.

The field of photonics in particular has propelled greatly as a result. With more control over geometry in the nanoscale, novel ways to tailor the flow of light become available from which diverse functionalities arise. One can strongly enhance various light matter-interaction phenomena through strong confinement of light and optical path length increase. Large enhancements of transmission, absorption, emission and nonlinear effects have been demonstrated with various nanostructures, reaching levels never seen before with naturally existing materials [5, 6]. As a result, there is a large spark of interest in studying and applying photonic nanostructures in various devices to enhance the devices' performance.

These recent developments are recognized by many as key in answering various growing necessities of the modern world, including the necessity for green sources of electrical energy. In the efforts to maintain a sustainable future under a growing world energy demand, highly efficient solar cells are of great importance.

Solar cells generate electrical power from incoming photon absorption and thus they are key in utilizing the immense power from the sun. 1.08×10^{14} kW power from the sun reaches the surface of the earth [7]. If 0.1% of this energy could be converted at an efficiency of only 10%, it would be four times the worlds total generating capacity of about 3000 GW [7]. This great renewable energy potential from the sun is a strong drive to increase the efficiency of solar cells. Having high efficiency solar cells however, is meaningless if the costs are too high. Currently, there are already multi-junction solar cells that reach close to 45% efficiency, though in the end they remain as labscale demonstrations due to their high costs [8, 9]. In response to this demand of high efficiency while being economically feasible, much research work is done in parallel on:

1. identifying and utilizing less costly materials suitable for solar cells,

2. improving light trapping and utilizing as less active material as possible.

With regards to the latter research direction, photonic nanostructures offer key opportunities as they can be engineered to maximize the intensity and transit time of photons in the active material and thus to improve absorption.

Many light flow control strategies have since been investigated for light trapping purposes in solar cells. By enhancing light absorption, one potentially reaches higher efficiency or one utilizes less active material, which could decrease the cost of solar cells. These structures increase absorption in the solar cell active material by: reducing front surface reflection, inducing strong scattering, providing access to guided modes, and also inducing strong electromagnetic field enhancement in the active layer [10–14]. Most of the structures that have been suggested, however, are limited in their capability to simultaneously excite different photonic phenomena in the broad solar spectrum of interest. To complicate matters, different solar cell materials have different limitations and light trapping needs and thus require specific photonic enhancement schemes.

To address these photonic challenges for solar cell absorption enhancement, in this thesis, we study combinations of various photonic elements in a single solar cell configuration. This combination approach is key in overcoming the limitations of each individual element, and thus it promises stronger absorbing cells with higher efficiencies. Both coherent and incoherent scattering elements are considered. To support the study involving incoherent scattering elements, a new calculation method to handle structures with wave and ray optics segments is developed. The conditions under which multiple photonic elements complement each other are identified and further explored.

Work has also been done on the electrical properties of thin polycrystalline silicon (poly-Si) films for solar cell purposes. This material carries much promise as an economical alternative for solar cells due to its potentially low fabrication

cost. However, it is challenged by structural defects, which affect carrier transport [15–17]. The carrier diffusion length requirement in order to obtain the desired performance under the influence of other parameters was investigated. We subsequently study in detail the effect of grain boundary recombination and varying grain size distribution in such a poly-Si thin-film solar cell. Furthermore, we performed capacitance-voltage and admittance spectroscopy measurements to study the doping density and defect distribution in poly-Si cells with n-type and p-type absorbers. This is a first step in identifying which doping type in the absorber layer would lead to a better solar cell.

In the general context of light-matter interaction enhancement, light flow control via plasmonic resonances is an especially attractive approach due to its strong near field enhancement [18]. The strong near field of plasmonic resonances stems from the coupling between photons and charge carriers of the plasmonic structure. Aside from improving absorption, one can utilize this strong near field property of plasmonic resonances to also improve other light-matter interaction phenomena such as light emission. Emission enhancement is a point of interest for solar cell applications as it can be used to improve photon up/down conversion processes that may be employed to tailor the spectrum of incoming photons and to potentially utilize solar power in a more efficient manner. Furthermore, a solar cell which reaches the Shockley-Queisser operation limit should also be a very efficient LED at open circuit voltage, indicating that it is not limitted by nonradiative recombination processes [19].

When one wishes to enhance emission over an extended volume of emitters, utilizing pure plasmonic resonances is not optimal. The strong near field enhancement by plasmonic resonances is connected to the strong confinement of the mode [18]. The positive effect of emission enhancement typically only occurs within the short characteristic decay length of the plasmonic mode field profile. For localized surface plasmon resonances (LSPR) in metal nanoparticles, this decay length is typically about 40 nm [18]. Aside from this, plasmonic nanoantenna structures which relies on LSPR offer limited control over the direction of emitted photons. This is due to the fact that inherently an LSPR couples to a continous set of radiation modes.

A novel approach to overcome the challenges in plasmonic light-matter interaction enhancement was introduced recently and expanded upon in this work. Instead of relying on pure plasmonic resonances, we consider hybrid plasmonic-photonic modes. We utilize the fact that photonic modes which overlap in space and in wavelength can interact with each other and form a new hybrid mode, which carries mixed characteristics from the different bare modes. Here, we study the hybridization between localized surface plasmon resonances of an array of metallic nanoantennas with Rayleigh anomaly (RA) diffraction and waveguide modes. As will be shown, such hybrid modes can still have a strong near field enhancement

while having a fairly extended field profile and low loss. Strong emission enhancement of a volumetric distribution of emitters is possible with a sharp linewidth and controlled directionality [20–22]. The emission directionality offered by hybrid plasmonic-photonic modes is stronger than localized surface plasmon resonances. This is due to the fact that the hybrid modes couple only to specific discrete radiation modes.

1.2 Outline

This work is structured as follows. In the next chapter the background concepts and numerical calculation methods relevant for the photonic part of the work are discussed. Various guided modes of light are presented along with methods to couple them with incoming and outgoing radiation. Important plasmonic modes relevant to the work are introduced. Finally, the basics of finite element calculations are discussed.

In chapter 3 we outline the background concepts for solar cells. The rationale behind semiconductor solar cell structures and its basic operation are discussed. Important charge carrier recombination mechanisms relevant to the poly-Si cells are introduced. The capacitance-voltage and admittance spectroscopy techniques to probe doping density and defect distribution in the cell are presented. Finally, a review of the dominant existing solar cell technologies is presented.

In chapter 4 we consider dual interface grating (DIG) structures for light trapping purposes in thin-film solar cells. These structures are formed by having grating structures at the front and back of a solar cell. We focus, in particular, on the use of triangular dual-interface grating structures with different materials. The benefits of forming a multiperiodic supercell with the DIG system are examined. Multiperiodic DIG structures are demonstrated to offer strong coupling efficiency enhancement to multiple guided modes simultaneously and thus they enhance absorption over a broad wavelength range. We further proceed to demonstrate how weak blazing of the DIG structure may lead to a very efficient excitation of modes that are not accessible in symmetric structures.

In chapter 5 we propose a simulation technique, which we developed, to efficiently address structures with wave optics and ray optics segments. Our method takes into account coherent effects where they matter the most while circumventing the need to fully implement the ray optics section of the structure. The extensive ray optics segments are avoided in our calculations by working directly with the wavefront coming out of them instead of their geometry. We discuss the effect of limited coherence on solar cell absorption. We show that the loss of phase relation can lead to an increase of absorption on average in the presence of a diffracting element in the structure, if certain geometrical conditions are met. We proceed to study light trapping of structures with both rough diffusers and gratings, each at a

different interface. More specifically, we examine combined structures with gratings at the front and rough diffusers at the back for both poly- and mono-crystalline thin-film Si solar cells.

In chapter 6 we present our study on the properties of hybrid plasmonic-photonic modes arising from the coupling of LSPR with either (RA) diffraction or waveguide modes. We demonstrate for the case of plasmonic surface lattice resonances, that their dispersion, linewidth, and associated stop-gap can be tuned by controlling the energy detuning between the interacting bare resonances. We further discuss the usage of liquid crystals to actively tune hybrid plasmonic-photonic modes. The tuning of extinction and photoluminescence (PLE) enhancement properties of hybrid plasmonic-photonic modes are experimentally and theoretically demonstrated.

In chapter 7 we examine poly-Si cells with varying intra-grain diffusion length and grain size distributions through numerical simulations. In particular, we consider the effect of other parameters such as thickness, doping density, and grain boundary recombination velocity. These calculations show the carrier diffusion length requirements to obtain the desired cell performance and the effect of grain size.

Finally, in chapter 8 we summarize and present an outlook.

1.3 Publications

1.3.1 Publications in international journals

The work performed during the PhD contributed to a number of publications in international refereed journals:

1. Aimi Abass, Said R.K. Rodriguez, Thomas Ako, Tangi Aubert, Zeger Hens, Jeroen Beeckman, Jaime Gómez Rivas, and Bjorn Maes. *Active liquid crystal tuning of plasmonic enhanced light emission from quantum dots*. (Submitted).

2. Aimi Abass, Said R.K. Rodriguez, Jaime Gómez Rivas, and Bjorn Maes. *Tailoring dispersion and eigenfield profiles of plasmonic surface lattice resonances*. ACS Photonics, Vol.1, pp. 6168. 2014.

3. Sven Leyre, Jan Cappelle, Guy Durinck, Aimi Abass, Geert Deconinck, Peter Hanselaer. *The use of the adding-doubling method for the optical optimization of planar down shifting layers for solar cells*. Optics Express Vol. 22, Issue S3, pp. A765-A778. 2014.

4. Aimi Abass, Christos Trompoukis, Sven Leyre, Marc Burgelman, and Bjorn Maes. *Modeling combined coherent and incoherent scattering structures*

for light trapping in solar cells. Journal of Applied Physics. Vol. 114. pp. 033101. 2013.

5. Marc Burgelman, Koen Decock, Samira Khelifi, and Aimi Abass. *Advanced electrical simulation of thin-film solar cells*. Thin Solid Films, Vol.535, pp. 296-301. 2013.

6. Erki Karber, Aimi Abass, Samira Khelifi, Marc Burgelman, Atanas Katerski and Malle Krunks. *Electrical characterization of all-layers-sprayed solar cell based on ZnO nanorods and extremely thin CIS absorber*. Solar Energy, Vol. 91, pp. 48-58. 2013.

7. Aimi Abass, Dries Van Gestel, Koen Van Wichelen, Bjorn Maes and M Burgelman. *On the diffusion length and grain size homogeneity requirements for efficient thin-film polycrystalline silicon solar cells*. J. Phys. D: Appl. Phys. Vol.46. pp.045105. 2013.

8. Aimi Abass, Khai Quang Le, Andrea Alù, Marc Burgelman and Bjorn Maes. *Dual-interface gratings for broadband absorption enhancement in thin-film solar cells*. Physical Review B. Vol. 85. pp.115449. 2012.

9. Khai Le Quang, Aimi Abass, Bjorn Maes, Peter Bienstman and Andrea Alù. *Comparing plasmonic and dielectric gratings for absorption enhancement in thin-film organic solar cells*. Optics Express. Vol. 20. pp.A39-A50. 2012.

10. Said R.K. Rodriguez, Aimi Abass, Bjorn Maes, Olaf TA Janssen, Gabriele Vecchi and Jaime Gómez Rivas. *Coupling bright and dark plasmonic lattice resonances*. Physical Review X. Vol. 1. pp.021019. 2011.

11. Aimi Abass, Honghui Shen, Peter Bienstman and Bjorn Maes. *Angle insensitive enhancement of organic solar cells using metallic gratings*. Journal Of Applied Physics. Vol. 109. pp.023111. 2011.

1.3.2 Contributions in international conferences

A list of our conference talks / proceeding contributions:

1. Aimi Abass, Said R.K. Rodriguez, Jaime Gómez Rivas, and Bjorn Maes. *Surface lattice resonances in plasmonic nanorod arrays*. Meta14 The 5th International Conference on Metamaterials, Photonic Crystals and Plasmonics, Singapore, 2014.

2. Islam Abdo, Christos Trompoukis, Aimi Abass, Bjorn Maes, Rafik Guindi, Valérie Depauw, Dries Van Gestel, Ivan Gordon, and Ounsi El Daif. *Combining periodic nanoimprint lithography and disorder for light trapping in*

polycrystalline silicon solar cells on foreign substrates. 28th European Photovoltaic Solar Energy Conference and Exhibition, Paris, France, 2013.

3. Aimi Abass, and Bjorn Maes. *Modeling coherent and incoherent light-trapping elements in solar cells*. 34th Progress In Electromagnetic Research Symposium (PIERS), Stockholm, Sweden, 2013.

4. Aimi Abass, and Bjorn Maes. *One pass coherent calculations to model structures with both wave and ray optics segments*. 9th International Symposium on Modern Optics and Its Applications (ISMOA), Bandung, Indonesia, p.PP-24, 2013.

5. Aimi Abass, and Bjorn Maes. *Combining light trapping structures to enhance thin-film solar cells*. 9th International Symposium on Modern Optics and Its Applications (ISMOA), Bandung, Indonesia, p.CP-08, 2013.

6. Aimi Abass, Marc Burgelman and Bjrn Maes. *Combining rough diffuser with periodic nanostructures for light trapping purposes*. Optical Nanostructures and Advanced Materials for Photovoltaics. Optical Society of America, Eindhoven, The Netherlands, paper PT2C.6, 2012.

7. Honghui Shen, Aimi Abass, Marc Burgelman and Bjorn Maes. *Tailored and tapered metallic gratings for enhanced absorption or transmission*. 14th International Conference on Transparant Optical Networks. University of Warwick Coventry, United Kingdom, p.Mo.B5.4, 2012 (invited).

8. Aimi Abass, Marc Burgelman and Bjorn Maes. *Dual-interface grating supercells for broadband absorption*. Photovoltaic technical conference: thin-film & advanced silicon solutions. Aix En Provence, France, 2012.

9. Honghui Shen, Aimi Abass, Marc Burgelman and Bjorn Maes. *Thin-film solar cells with combined metallic enhancements*. Micro- and nano-photonic materials and devices. Trento, Italy, p.103-104, 2012.

10. Khai Le Quang, Aimi Abass, Bjorn Maes, Peter Bienstman and Andrea Alù. *Using localized plasmon resonances to enhance absorption efficiency in thin-film organic solar cells*. Optical Nanostructures and Advanced Materials for Photovoltaics. Optical Society of America, Austin, Texas, USA, p.paper PThD3, 2011.

11. Aimi Abass, Khai Le Quang, Peter Bienstman, Andrea Alù, Bjorn Maes and Marc Burgelman. *Combining front and back grating structures for broadband absorption enhancement in thin-film silicon solar cells*. Optical Nanostructures and Advanced Materials for Photovoltaics. Optical Society of America, Austin, Texas, USA, p.paper PWC4, 2011.

12. Aimi Abass, Bjorn Maes, Dries Van Gestel, Koen Van Wichelen and Marc Burgelman. *Effects of inhomogeneous grain size distribution in polycrystalline silicon solar cells*. Energy Procedia. Elsevier. Vol. 10. 2011. 55-60.

13. Aimi Abass, Honghui Shen, Khai Quang Le, Peter Bienstman, and Bjorn Maes. *On the angular dependent nature of absorption enhancement in organic solar cells by metallic nanostructures*. 8th International Symposium on Modern Optics and Its Applications (ISMOA), Indonesia, p.PP-07, 2011.

14. Khai Quang Le, Bjorn Maes, Peter Bienstman and Aimi Abass. *Plasmonic nano-antennas for absorption enhancement in thin-film silicon solar cells*. Euro Physics Conference Abstracts. Vol. 35A. 2011

15. Aimi Abass, Honghui Shen, Peter Bienstman, Bjorn Maes, *Increasing polymer solar cell efficiency with triangular silver gratings*. Optical Society of America (OSA) Topical Meeting on Optical Nanostructures for Photovoltaics (PV). Karlsruhe, Germany, p.PWA5, 2010 (invited).

16. Khai Quang Le, Aimi Abass, Bjorn Maes, Peter Bienstman, *Analytical study of enhanced optical absorption of molecules near silver nanoparticles*. Optical Society of America (OSA) Topical Meeting on Optical Nanostructures for Photovoltaics (PV). Karlsruhe, Germany, p.PWB5, 2010

References

[1] K. Ogai, Y. Kimura, R. Shimizu, J. Fujita, and S. Matsui. *Nanofabrication of grating and dot patterns by electron holographic lithography*. Applied Physics Letters, 66(12):1560–1562, 1995.

[2] M. Deubel, G. Von Freymann, M. Wegener, S. Pereira, K. Busch, and C. Soukoulis. *Direct laser writing of three-dimensional photonic-crystal templates for telecommunications*. Nature Materials, 3(7):444–447, 2004.

[3] B. D. Gates, Q. Xu, M. Stewart, D. Ryan, C. G. Willson, and G. M. Whitesides. *New approaches to nanofabrication: molding, printing, and other techniques*. Chemical Reviews, 109(2):1171–1196, 2005.

[4] J. Fischer and M. Wegener. *Three-dimensional direct laser writing inspired by stimulated-emission-depletion microscopy (Invited)*. Opt. Mater. Express, 1(4):614–624, 2011.

[5] F. Flory, L. Escoubas, and G. Berginc. *Optical properties of nanostructured materials: a review*. Journal of Nanophotonics, 5(1):052502–052502–20, 2011.

[6] M. Kauranen and A. V. Zayats. *Nonlinear plasmonics*. Nature Photonics, 6(11):737–748, NOV 2012.

[7] W. E. Council. *World Energy Resources: 2013 Survey*. World Energy Council, 14 Warwick Street London W1B 5LT, 1st edition, 2013.

[8] M. A. Green, K. Emery, Y. Hishikawa, W. Warta, and E. D. Dunlop. *Solar cell efficiency tables (version 43)*. Progress in Photovoltaics: Research and Applications, 22(1):1–9, 2014.

[9] K. Tanabe. *A Review of Ultrahigh Efficiency III-V Semiconductor Compound Solar Cells: Multijunction Tandem, Lower Dimensional, Photonic Up/Down Conversion and Plasmonic Nanometallic Structures*. Energies, 2(3):504–530, 2009.

[10] K. R. Catchpole and A. Polman. *Plasmonic solar cells*. Optics Express, 16(26):21793–21800, 2008.

[11] Z. Yu, A. Raman, and S. Fan. *Fundamental limit of light trapping in grating structures*. Optics Express, 18(S3):A366–A380, 2010.

[12] V. E. Ferry, M. A. Verschuuren, H. B. T. Li, E. Verhagen, R. J. Walters, R. E. I. Schropp, H. A. Atwater, and A. Polman. *Light trapping in ultrathin plasmonic solar cells*. Optics Express, 18(13):A237–A245, 2010.

[13] A. Abass, H. Shen, P. Bienstman, and B. Maes. *Angle insensitive enhancement of organic solar cells using metallic gratings*. Journal of Applied Physics, 109(2):023111–7, 2011.

[14] X. Meng, V. Depauw, G. Gomard, O. El Daif, C. Trompoukis, E. Drouard, C. Jamois, A. Fave, F. Dross, I. Gordon, and C. Seassal. *Design, fabrication and optical characterization of photonic crystal assisted thin film monocrystalline-silicon solar cells*. Optics Express, 20(S4):A465–A475, 2012.

[15] I. Gordon, D. Van Gestel, K. Van Nieuwenhuysen, L. Carnel, G. Beaucarne, and J. Poortmans. *Thin-film polycrystalline silicon solar cells on ceramic substrates by aluminium-induced crystallization*. Thin Solid Films, 487(1-2):113–117, 2005.

[16] I. Gordon, L. Carnel, D. Van Gestel, G. Beaucarne, and J. Poortmans. *8on aluminum-induced crystallization and thermal CVD*. Progress in Photovoltaics, 15(7):575–586, 2007.

[17] I. Gordon, L. Carnel, D. Van Gestel, G. Beaucarne, and J. Poortmans. *Fabrication and characterization of highly efficient thin-film polycrystalline-silicon solar cells based on aluminium-induced crystallization*. Thin Solid Films, 516(20):6984–6988, 2008.

[18] S. A. Maier. *Plasmonics: Fundamentals and Applications*. Springer, New York, USA, 2007.

[19] O. D. Miller, E. Yablonovitch, and S. R. Kurtz. *Strong Internal and External Luminescence as Solar Cells Approach the Shockley-Queisser Limit*. Photovoltaics, IEEE Journal of, 2(3):303–311, 2012.

[20] S. R. K. Rodriguez, G. Lozano, M. A. Verschuuren, R. Gomes, K. Lambert, B. D. Geyter, A. Hassinen, D. V. Thourhout, Z. Hens, and J. G. Rivas. *Quantum rod emission coupled to plasmonic lattice resonances: A collective directional source of polarized light*. Applied Physics Letters, 100(11):111103, 2012.

[21] S. R. K. Rodriguez, S. Murai, M. A. Verschuuren, and J. G. Rivas. *Light-Emitting Waveguide-Plasmon Polaritons*. Physical Review Letters, 109:166803, 2012.

[22] G. Lozano, D. J. Louwers, S. R.K. Rodriguez, S. Murai, O. T. Jansen, M. A. Verschuuren, and J. Gomez Rivas. *Plasmonics for solid-state lighting: enhanced excitation and directional emission of highly efficient light sources*. Light Science and Applications, 2:e66, 2013.

2
Basic photonic concepts

This chapter summarizes the basic concepts in photonics that are most relevant to the work. Lossless guided propagation of light is discussed in section 2.1. The conditions for radiative coupling to guided modes is then described in section 2.2. Section 2.3 dwells on the limitations and the challenge of achieving efficient higher order diffraction coupling to guided modes. The nature of propagating surface plasmon polaritons is reviewed in section 2.4. Section 2.5 introduces localized surface plasmon resonances, which can be found in nanoparticles with enough free charge. The principles behind the direct coupling of emitted photons to a certain photonic mode are briefly given in section 2.6. Section 2.7 outlines the basics of the finite element method, which is used extensively in this work.

2.1 Guided modes of light

In photonic applications controlling the flow of light is essential. All the various photonic devices rely on having a sufficient number of photons to either reach a certain location or pass through a certain route. Typically, the aim is to have light significantly interact with matter only at an intended location or throughout its whole travel path. One example of photonic devices for communication applications is the fiber optic cable. Through the fiber, light signals which carry information travel from one point to another without significant loss of intensity. Another example is the use of photonic chips for sensing applications through which light probes a refractive index change. This data is then used to infer the concentration

of a certain compound in the surroundings. For energy harvesting applications, which is the main interest of this work, one is interested to boost absorption by utilizing photonic structures that increase the amount of photons entering the active layer and their travel time in there. In all of these applications, it is necessary for light to be adequately confined in space as it propagates along the desired route. This confined propagation is precisely what is meant by the term guided.

Photons are energy quanta of electromagnetic (EM) waves which are governed by the Maxwell equations [1]:

$$\begin{aligned} \nabla \cdot \mathbf{D} &= \rho_V \\ \nabla \cdot \mathbf{B} &= 0 \\ \nabla \times \mathbf{E} &= -\frac{\partial \mathbf{B}}{\partial t} \\ \nabla \times \mathbf{H} &= \frac{\partial \mathbf{D}}{\partial t} + \mathbf{J} \end{aligned} \tag{2.1.1}$$

where $\mathbf{E}$ is the electric field, ρ_V is the volumetric free charge density, $\mathbf{B}$ is the magnetic induction, $\mathbf{H}$ is the magnetic field, ϵ is the permittivity, $\mathbf{D} = \epsilon\mathbf{E}$ is the electric displacement field, and $\mathbf{J}$ is the current density. Equivalently, EM waves are probability wave function of photons [2]. One of the many ways to force EM waves (therefore photons) to propagate in a guided manner is by directly having reflecting boundaries at the side walls of a guiding core. One simple example of this is the propagation of EM waves through a large hollow metal cylinder as shown in Figure 2.1a. When an EM wave impinges on an air-metal interface, its oscillating electric field will move free electrons at the metal surface. The resulting oscillating charge movement may in turn produce a new EM wave which interferes with the incoming wave and effectively results in efficient reflection. How well the electrons can move in correspondence with the field oscillation depends on the metal properties and the frequency of the wave. The metal hollow cylinder in Figure 2.1a can thus act as a waveguide. Its walls can reflect incoming EM waves and thus prevents EM waves in its hollow core from escaping.

Having reflective metal boundaries, however, is not the only way to force EM waves to propagate in a confined space. To achieve a lossless guiding of light, one can utilize the fact that there is a momentum mismatch between photons propagating freely in different dielectric materials [3]. The canonical momentum of a photon $\mathbf{p}$ follows the expression $\mathbf{p} = \frac{h\mathbf{k}}{2\pi}$ where $\mathbf{k}$ is the wavevector of the photons wavefunction (EM wave) and h is the planck constant. Photons travelling in a higher refractive index material effectively have larger momentum as $|\mathbf{k}|$ depends linearly on the refractive index n. The propagation of photons from one material to another with different refractive index would thus require a change in momentum. The required momentum change is typically imparted to the photons at the interface between the two materials but not without limitations. The momentum

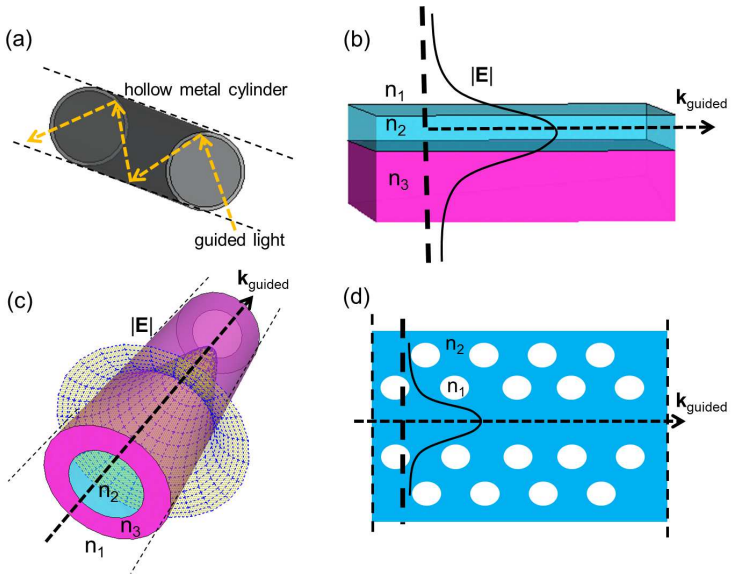

Figure 2.1: Possible waveguiding structure examples: (a) hollow metalic tube waveguide, (b) slab dielectric waveguide, (c) dielectric cylindrical waveguide, and (d) photonic crystal waveguide.

change a photon can experience at an interface has a certain directionality restriction dictated by the Maxwell equations. Thus, provided that the interface does not impart the necessary momentum change for photons to leave a certain material, one can maintain EM waveguiding.

The basic principle behind such waveguiding lies in the continuity conditions for the **E** and **H** field. At an interface between two materials, the component of **E** and **H** field parallel to that interface must be continuous when there are no free surface charges or currents. That is to say, when an EM wave hits a flat interface, only the momentum component perpendicular to the interface can change. The necessity of having these field components parallel to an interface continuous dictates the parallel momentum component $k_{//}$ to be identical at both sides of the interface. If $k_{//}$ of the incoming EM wave from one material is greater than the allowed momentum of propagating EM plane waves in the other material, then the incoming EM wave will be completely reflected back provided that nothing on the interface changes the $k_{//}$ component. This phenomenon is known as total internal reflection (TIR) and can be used to guide EM waves.

Wave guiding by utilizing such momentum discrepancy is readily achieved by having a refractive index contrast. As higher refractive index dielectric media can sustain EM plane waves with higher momentum, one can therefore sustain guiding in a high index dielectric material by surrounding it with lower index cladding

materials. Examples of such waveguides are shown in Figure 2.1b and c which depict a dielectric slab and cylindrical waveguide respectively. In those structures, $n_2 > n_3 \geq n_1$. The boundaries of the waveguide shown in Figure 2.1b and c cannot modify the momentum of EM waves propagating in the guiding direction $\mathbf{k}_{guided}$ which is parallel to the guiding boundaries. Thus, guided EM waves in those structures would have

$$|\mathbf{k}_{guided}| \geq \frac{2\pi n_{cladding}}{\lambda_0} \tag{2.1.2}$$

where λ_0 is the free space wavelength, $n_{cladding}$ is the cladding material refractive index which in the case of Figure 2.1b and c are n_1 and n_3. Equation (2.1.2) is basically the TIR condition at the interfaces. In the field of communications, guiding via TIR is preferable than with metals, as dielectrics do not have ohmic losses which could disrupt the information that is carried.

Instead of relying only on refractive index constrast, which is a material property, it is also possible to guide EM waves by engineering the momentum requirement of the cladding material. The idea is to surround the intended guiding core with artificial materials that do not support the propagation of EM waves in a certain frequency range [4]. One can obtain such a material by periodic patterning and forming a photonic crystal as shown in Figure 2.1d. The periodicity of the material restricts the allowable EM wave modes of propagation, which will be discussed in more detail in section 2.2. When engineered correctly, it is possible to have a complete photonic bandgap such that no mode of propagation is allowed for a certain frequency range [4, 5]. In practice, a complete photonic bandgap is not necessary to guide light if one only wants to guide EM waves with a certain polarization or prevent the waves from escaping to a certain direction. One of the most attractive reasons to guide light with this approach is the increased flexibility in tuning the guided modes momentum and field extension, as there is no fundamental minimum momentum requirement that depends on the material properties like the TIR condition.

When the guiding core size is comparable to the wavelength, one has to additionally take into account the discrete nature of allowable wavevectors (momentum) for guided EM waves, as in the case of other (quantum) systems [3]. This discrete nature stems from the fact that a guided wave should preserve its wavefront as it propagates along the waveguide structure. Having the wavefront preserved during propagation would mean that the wave function is an eigenmode of the structure or a superposition of lossless eigenmodes. Hence the term guided mode. The field profile of guided modes will not change except by a phase factor if there are no loss mechanisms.

A guided EM wave electric field profile $\mathbf{E}(\mathbf{r}, t)$ with a certain angular frequency ω has several mathematical properties. First it fulfills the master frequency

domain (Helmholtz) wave equation which follows from the Maxwell equations [3]:

$$\nabla \times \nabla \times \tilde{\mathbf{E}}(\mathbf{r},\omega) - (k_0 n(\mathbf{r}))^2 \tilde{\mathbf{E}}(\mathbf{r},\omega) = 0 \tag{2.1.3}$$

where $\mathbf{E}(\mathbf{r},t) = \tilde{\mathbf{E}}(\mathbf{r},\omega)\exp(-i\omega t)$, $k_0 = \omega/c_0$, and where $c_0 = \frac{1}{\sqrt{\mu_0 \epsilon_0}}$ is the speed of light in vacuum. $n(\mathbf{r}) = \sqrt{\epsilon_r(\mathbf{r})\mu_r(\mathbf{r})}$ is the refractive index function which describes the guiding structure with ϵ_r and μ_r being the relative permittivity and permeability respectively. The Helmholtz wave equation can be restated as an eigenvalue problem:

$$\hat{Z}\tilde{\mathbf{E}}(\mathbf{r},\omega) = \left(\frac{\omega}{c_0}\right)^2 \tilde{\mathbf{E}}(\mathbf{r},\omega) \tag{2.1.4}$$

with $\hat{Z} = \frac{1}{n(\mathbf{r})^2}\nabla \times \nabla\times$. Here $\left(\frac{\omega}{c_0}\right)^2$ is the eigenvalue and $\tilde{\mathbf{E}}(\mathbf{r},\omega)$ is the eigenfunction. Therefore, the frequency of a guided mode is an eigenfrequency of the operator $\hat{Z}$. Often, the frequency of an eigenmode wavefunction is refered to as an eigenfrequency of the system.

More than just fulfilling (2.1.3), the spatial dependence of a guided mode EM field profile can be expressed in the form:

$$\tilde{\mathbf{E}}(\mathbf{r}) = \vec{\Psi}(x,y)\exp(-i\beta z) \tag{2.1.5}$$

for a guided mode with the z-direction as the guiding direction, and $\beta = |\mathbf{k}_{guided}|$. For ease in reference, the dependence of $\tilde{\mathbf{E}}$ on ω is omitted. Furthermore, $\vec{\Psi}(x,y)$ is a spatially bounded function in the case of a guided mode. In other words, the electromagnetic field profile is constricted to the vicinity of the guiding structure (at least bounded in one direction depending on the guiding structure).

Utilizing (2.1.5) the Helmholtz wave equation (2.1.3) can be expressed as:

$$\left(\frac{\partial^2}{\partial x^2} + \frac{\partial^2}{\partial y^2}\right)\vec{\Psi}(x,y) + (k_0 n(\mathbf{r}))^2 \vec{\Psi}(x,y) = \beta^2 \vec{\Psi}(x,y) \tag{2.1.6}$$

This equation can be further shortened to the form of:

$$\hat{\Xi}\vec{\Psi}(x,y) = \beta^2 \vec{\Psi}(x,y) \tag{2.1.7}$$

where $\hat{\Xi} = \left(\frac{\partial^2}{\partial x^2} + \frac{\partial^2}{\partial y^2}\right)\vec{\Psi}(x,y) + (k_0 n(\mathbf{r}))^2$ is an operator. In this form β^2 and $\vec{\Psi}$ can be recognized as the eigenvalue and the eigenfunction of the operator $\hat{\Xi}$. The spatial profile of a guided mode must therefore be an eigenfunction of $\hat{\Xi}$.

Note that EM wave eigenmodes of a certain structure do not necessarily have to be guided. In a similar manner, freely propagating plane waves are actually eigenmodes of a homogeneous system of constant refractive index, as plane waves propagate in such systems with their wavefront preserved. If the wavefront is not preserved, then the propagating wave must have additional nonguided components that are interfering with any available guided components. Note that a

waveguide structure can also support nonguided eigenmodes which would preserve their own wavefront as they propagates. However, the contribution that each nonguided component gives to the total field would change as they propagate due to the propagation loss.

In the case of slab waveguides, the eigenfield profiles are analytically known. There the wavefront phase requirement is satisfied by [3]:

$$k_t = \frac{m2\pi - 2\phi_{c1} - 2\phi_{c2}}{2d} = \sqrt{k_0 n_{core}^2 - |\mathbf{k}_{guided}|^2} \tag{2.1.8}$$

where $m = 0, 1, 2...$; ϕ_{c1} and ϕ_{c2} are the phase shifts due to TIR at the top and bottom cladding boundaries respectively, d is the thickness of the waveguide, n_{core} is the refractive index of the waveguide core, k_t is the transversal k-vector component in the guiding core. Equation (2.1.8) restricts k_t to discrete values and thus also forces $\mathbf{k}_{guided}$ to be discrete. For more complicated structures, analytical solutions are not necessarily available and one resorts to numerical approaches.

Aside from the previous examples, there are also types of guided modes which exist only at interfaces. One example of this is the Surface Plasmon Polariton (SPP) mode which exists on a metal-dielectric interface. The SPP mode is a guided mode which is achieved through a sustained coupling of photons with the metal conduction electrons at the metal surface. Another type of interface mode that is of great interest is the plasmonic Surface Lattice Resonance (SLR) which is a hybrid between the localized surface plasmon resonance and Rayleigh anomaly diffraction. The SLR modes are explained in detail in chapter 6.

2.2 Leaky guided modes

By virtue of time reversal symmetry, one can see that guided modes cannot be excited by radiation impinging from the cladding. One needs to either introduce a certain scatterer that can impart sufficient momentum to the incoming wave (Figure 2.2a) or engineer the guided modes to have a radiative nature by modifying the guiding structure throughout. In solar cells or light emitting diode applications, the latter is preferred as this would ensure a more spatially homogeneous device performance than otherwise. In principle, once the coupling of a guided mode with radiation is allowed, the term 'guided' no longer strictly applies. However, since such modes still involve a localization of light intensity, the term 'leaky' guided modes will be used to describe them (alternatively, many prefer to use the term quasi-guided modes).

The presence of any loss mechanism in the waveguide structure would force the corresponding guided modes to have an imaginary component in their wavevector. Such lossy guided modes maintain their field profile shape though they suffer from amplitude decay as they propagate. Inherent material absorption in the guiding structure also contributes to the guided mode's total loss rate.

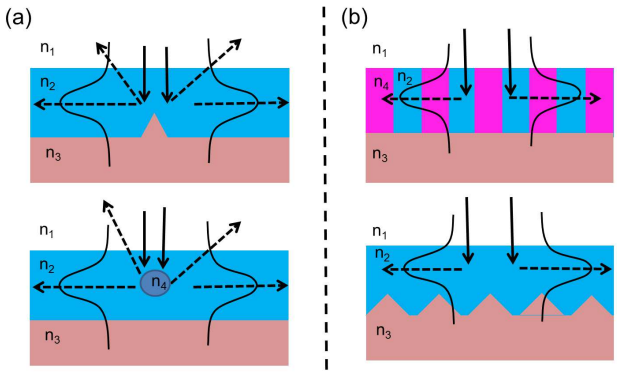

Figure 2.2: Coupling of radiation to guided modes through (a) single and (b) periodic scattering structures.

Although one can simply introduce a random rough pattern to make guided modes radiative, doing so would not give the capability of tailoring the coupling efficiency and coupling length between radiation and guided modes. In cases where it is desirable to further optimize these guided mode properties, one can instead utilize an ordered periodic pattern (gratings) either in the geometry or in the comprising material properties as shown in Figure 2.2b.

To understand the effect of periodic perturbations on guided modes, let us take the case of a normal slab waveguide to which we impart such a perturbation in its geometry or refractive index as in Figure 2.2b. The effect of introducing periodicity to the guided modes is illustrated step by step in Figure 2.3. Figure 2.3a shows a dispersion diagram that depicts the angular frequency ($\omega = 2\pi f$) versus wavevector ($\mathbf{k} = \mathbf{p}/\hbar$) relation of a non-radiative waveguide mode and the light line of the cladding material in an unperturbed system. The light line shows the relationship $\frac{\omega}{c} = |\mathbf{k}|$ where c is the speed of light in that medium. The light line basically indicates the $|\mathbf{k}|$ value beyond which an EM wave is evanescent (at certain or all directions depending on the magnitude of the k component at each direction). As mentioned in the previous section, a guided mode's momentum in an unperturbed waveguide structure is larger than the maximum allowable momentum for propagating waves in the cladding. Thus, a guided mode's dispersion would lie below the light line ($|\mathbf{k}| > \frac{\omega}{c_{cladding}}$) as depicted in Figure 2.3a.

Upon introduction of periodicity to the waveguide structure, however weak a perturbation it is, the Bloch theorem states that the eigenmodes must be pseudo periodic in nature and can be described with [4]:

$$\Theta(\mathbf{k}, \mathbf{r}) = \tilde{\Theta}(\mathbf{r}) \exp(-i\mathbf{k} \cdot \mathbf{r}) \tag{2.2.1}$$

where $\tilde{\Theta}(\mathbf{r})$ is a periodic function with the same periodicity as the unit cell of the

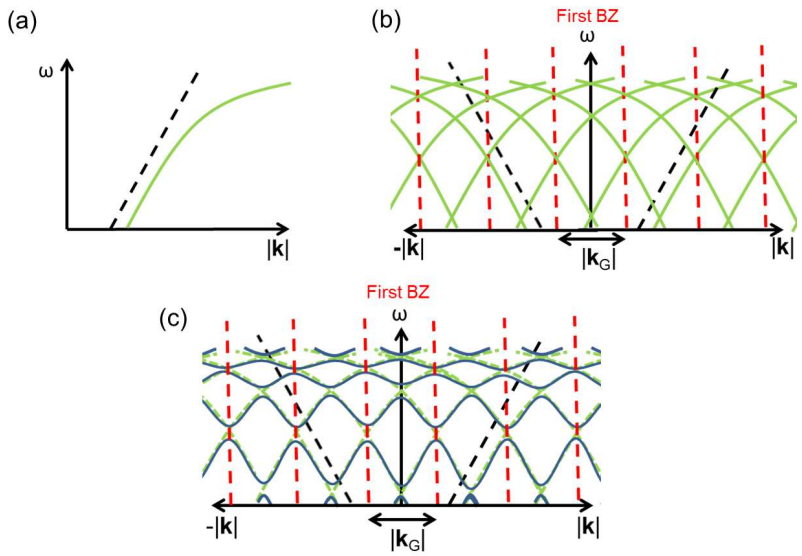

Figure 2.3: Dispersion evolution of a waveguide mode upon introduction of a periodic perturbation. (a) Guided mode dispersion diagram sketch in an unpatterned system. (b) Effect of periodicity on a guided mode dispersion. (c) Effect of both periodicity and perturbation on a guided mode dispersion.

system and for the case of 1D periodicity can thus be expressed as

$$\tilde{\Theta}(\mathbf{r}) = \sum_{m=-\infty}^{\infty} A(\mathbf{k} - m\mathbf{k}_G)\exp(-i\mathbf{k}_G \cdot \mathbf{r}) \tag{2.2.2}$$

where $\mathbf{k}_G = \frac{2\pi}{P}\hat{\mathbf{a}}$ with P is the periodicity and $\hat{\mathbf{a}}$ is the unit lattice vector of the periodic system, and m is an integer. Note that the Bloch wave function would fulfill $\Theta(\mathbf{k}, \mathbf{r}) = \Theta(\mathbf{k} + m\mathbf{k}_G, \mathbf{r})$. Thus, the Bloch theorem dictates that there would be identical waveguide modes that differ by the term $\exp(-i\mathbf{k}_G \cdot \mathbf{r})$ in their wavefunction in the presence of periodicity. As a result, looking at the first Brilouin zone (BZ), the introduced periodicity effectively folds the dispersion diagram of the waveguide modes as shown in Figure 2.3b.

In reality, the introduced perturbation also affects the eigenmode field profile. One common signature of this is a split of the crossings we see in Figure 2.3b [4]. This splitting effect is shown in Figure 2.3c. A physical intuition behind the splitting can be obtained through examining the nature of the crossings. Each dispersion crossing in Figure 2.3b essentially indicates the existence of two degenerate modes which travel in opposite directions. The contra-propagation of these modes forms two possible standing wave patterns: symmetric and anti-symmetric. The two possible standing wave patterns may in general have a differing energy distri-

bution depending on the structure. This therefore corresponds to different resonant frequencies for each possibility and thus the splitting.

Due to the dispersion folding effect by the periodicity, there now exists guided modes at certain wavelengths with momentum above the cladding material light line. However, even in the regime where there is no momentum restriction on coupling to radiation, radiative coupling may still be unallowed or unefficient. Field profile symmetry also determines the radiative nature of eigenmodes. For example, at $k_{//} = 0$, one of the resulting eigenmodes at the splitting points has no net in-plane dipole moment due to the anti-symmetric field profile distribution of its in-plane electric field component within one cell period. Such guided modes do not couple to any radiation though they cross the $k_{//} = 0$ point, and are thus labelled 'dark'. In contrast, leaky guided modes which do couple to radiation at $k_{//} = 0$ are labelled 'bright'.

Fulfilling the momentum requirement and not having a completely anti-symmetric in-plane eigenfield profile distribution are still not enough to guarantee efficient radiation to leaky guided mode coupling. For incoming radiation to excite a leaky guided mode, there also needs to be a correspondence between the scattered wave, generated by the interaction between incoming radiation and the structure, with the eigenfield profile of the leaky guided modes. Another way to see why dark modes cannot couple to normal incident plane waves is the fact that the scattering of a symmetric wavefront by a symmetric structure cannot result in an antisymmetric profile.

2.3 Higher order coupling processes

Resonant coupling processes through conventional gratings in which radiation modes couple to guided modes through higher order diffraction tend to have a low efficiency [6]. Eigenfield profiles of waveguide modes arising from fundamental and higher order processes are shown in Figure 2.4. The higher the diffraction coupling order, the lower the coupling efficiency. The reason behind this is the low scattered and modal field overlap which makes the coupling inefficient. As shown in Figure 2.4, eigenmodes related to higher order processes have more oscillations within one cell period or along the core thickness. Providing a scattered field profile with a stronger oscillating behavior to match higher order diffraction processes would typically require a pattern of similar periodicity. Lowering the periodicity of our gratings however, would just mean shifting the first order resonant wavelength.

Another way to improve higher order diffraction coupling is to superpose different grating patterns of varying periodicity $\frac{P}{m}$ with $m = 1, 2, 3, ...$ By doing so, one introduces stronger higher order fourier components to the grating structure [6, 7]. Each periodicity component will serve to provide the necessary scat-

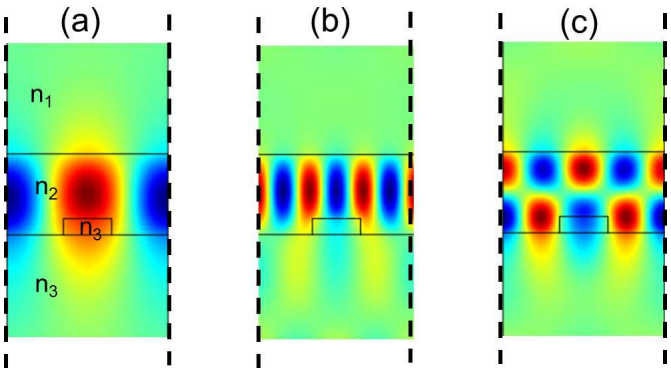

Figure 2.4: Guided mode field profiles in a slab waveguide arising from (a) fundamental diffraction coupling order, (b) higher diffraction coupling order, and (c) higher order waveguide mode with higher diffraction coupling order

tered field profile for higher order diffraction coupling. One can essentially tune which transition would be more efficient than others by making the grating Fourier component corresponding to that particular transition stronger than the other components. Relying on this approach however, often leads to an overly complicated grating geometry that is difficult to fabricate. In chapter 4 we provide various ideas to optimize these types of situations.

2.4 Propagating surface plasmon polariton

Photons may have a sustained coupled propagation with other particles such as phonons, excitons and electrons. This is due to the fact that photons are basically propagating electric and magnetic field disturbances, which can affect the surrounding. Such coupled propagations with photons are labeled polaritons. One type of polariton that is of great interest to the work here is the surface plasmon polariton (SPP).

A SPP is the coupled propagation of photons and an electron cloud (plasmon) at an interface between two materials [8]. An SPP mode requires one of the materials to have relatively free electrons whose mobility can react adequately to the oscillation of the EM wave coupled to them. For EM waves at optical frequencies, SPP modes are typically supported by metal-dielectric interfaces. SPP modes can also be supported in the THz frequency regime by semiconductor-dielectric interfaces provided that the semiconductor is doped sufficiently [9]. One of the simplest types of SPP modes is found on a flat metal-dielectric interface as shown in Figure 2.5. The SPP mode is an eigenmode of the EM wave equation in such semi-infinite metal-dielectric systems. In such a flat interface system, the SPP dis-

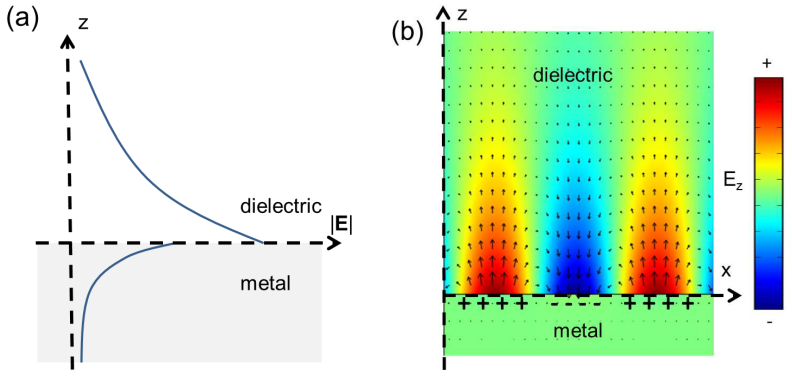

Figure 2.5: (a) $|\boldsymbol{E}|$ cross-section and (b) xz cross-section of the z-electric field component E_z of a surface plasmon polariton mode on a flat interface with propagation in the x-direction.

persion lies below the light line and thus does not couple to radiation. Physically, the huge momentum that SPP modes have comes from the fact that plasmons are also involved in the propagation contributing to the total momentum. The magnitude of a wavevector of a SPP mode k_{SPP} on a flat interface is expressed with the equation:

$$k_{\mathrm{SPP}} = \frac{\omega}{c}\sqrt{\frac{\epsilon_1\epsilon_2}{\epsilon_1+\epsilon_2}} \tag{2.4.1}$$

which can be obtained simply from solving the boundary conditions set by Maxwell equations at the interface. ϵ_1 and ϵ_2 is the metal and dielectric permittivity respectively. Figure 2.5a shows the expontentially decaying nature of the mode as the distance from the interface increases. Figure 2.5b shows a typical field profile of an SPP mode as it propagates along with the surface charge. The field profile is expressed with the equation:

$$E_z(x,z,\omega) = -A\frac{k_{SPP}}{\omega\epsilon_0\epsilon_2}\exp\left(-i(k_{SPP}x - k_{t2}z + \omega t)\right) \tag{2.4.2}$$

$$E_x(x,z,\omega) = iA\frac{k_{t2}}{\omega\epsilon_0\epsilon_2}\exp\left(-i(k_{SPP}x - k_{t2}z + \omega t)\right) \tag{2.4.3}$$

for $z > 0$ and

$$E_z(x,z,\omega) = -A\frac{k_{SPP}}{\omega\epsilon_0\epsilon_1}\exp\left(-i(k_{SPP}x + k_{t1}z + \omega t)\right) \tag{2.4.4}$$

$$E_x(x,z,\omega) = -iA\frac{k_{t1}}{\omega\epsilon_0\epsilon_1}\exp\left(-i(k_{SPP}x + k_{t1}z + \omega t)\right) \tag{2.4.5}$$

for $z < 0$ where A is the amplitude constant, $k_{ti} = \sqrt{(k_0 n_i)^2 - k_{SPP}^2}$ is the transversal k-vector component which will have a purely imaginary value for SPP

modes and will be the cause of the exponential decay in the transversal direction. As $\frac{k_{t1}}{k_{t2}} = -\frac{\epsilon_1}{\epsilon_2}$ the continuity of E_x is fulfilled.

On a flat interface SPP modes are only supported for Transverse Magnetic (TM) polarization where the electric field is in the propagation plane of the mode (xz plane in Figure 2.5b). The continuity conditions from Maxwell equations do not allow confinement of an EM wave with Tranverse Electric (TE) polarization to the metal-dielectric interface.

Light propagating in the form of SPP modes can be confined to a volume much smaller than the diffraction limit as a consequence of having a large parallel momentum component [8]. This tight confinement translates to a large field intensity near the metal interface. Inherently, SPP modes have a field component that goes into the metal and therefore they experience absorption losses there. However, a majority part of the SPP eigenfield lies on the dielectric side of the interface. Thus, the strong confinement and large field intensity that SPP modes offer are attractive for enhancing various light-matter interaction processes close to the metal interface. Many applications of SPP modes improving various light-matter interaction phenomena have been demonstrated throughout the years [8, 10–12]. In many such applications, the SPP mode is coupled to radiation via grating structures following the same principles as other guided modes described before. In chapter 4 we will show the usage of SPP modes to improve absorption in solar cells.

2.5 Localized surface plasmon resonance

Nanoparticles can also sustain plasmonic modes that are localized in nature. EM waves incoming to the nanoparticles can interact with the electron cloud in them as shown in Figure 2.6. At a certain frequency of the driving EM wave charge accumulation at the surface of the particle will be optimal and in turn these charges affect the surrounding EM field as shown in Figure 2.6b. This phenomenon is called the localized surface plasmon resonance (LSPR) [8]. As for propagating SPP modes, LSPRs also have the characteristic of having a high near field intensity due to the high surface charge accumulation. The characteristics of LSPRs are highly dependent on the nanoparticle geometry as the plasmon movement is constrained by it. One typically observes LSPRs for visible light with metal nanoparticles. The LSPR excitation may even have a strong dependence on the polarization of the EM wave if the shape of the particle is not symmetric.

Depending on its size, a nanoparticle may support higher order LSPRs. These higher order LSPR resonances are either perfectly dark (give zero net dipole moment), or only weakly coupling with radiation. They contribute to emission quenching near metal nanoparticles. However, since higher order LSPRs are typically more confined to the metal surface than the fundamental order, one can avoid their quenching effect by positioning the emitter further from the surface.

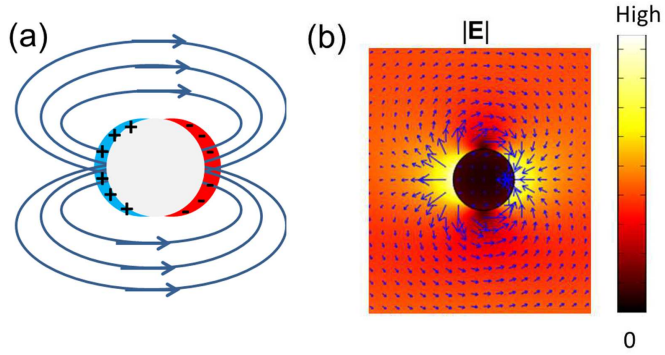

*Figure 2.6: (a) Sketch of **E** field and charge distribution of a localized surface plasmon resonance (LSPR). (b) |**E**| field plot of the LSPR excited by a plane wave incoming from the bottom.*

The LSPR phenomenon is quite attractive for broadband absorption and scattering enhancement purposes [13, 14]. Fundamental order LSPRs tend to have a very broad bandwidth which can easily stretch to several hundreds of nanometer in linewidth due to its high losses. The coupling of free EM waves to the LSPR tends to be independent of the wavevector k (having a flat dispersion) if the nanoparticle is symmetric. This flat dispersion characteristic indicates that the LSPR has many radiative loss routes possible and can scatter light to various directions. The fundamental order LSPR in fact gives a very strong scattering effect. This is to be expected as the surface charge built up at the resonance frequency would generate a strong dipole moment.

2.6 Emission to photon eigenstates

When a photon is emitted from a certain source, it occupies one of the possible photonic states of the system, which has a specific eigenfield profile pertaining to that state. The more photon states available for an emitter, the shorter the radiative decay time of that emitter will be. As for classical EM eigenmodes, these photon states are dependent on the system. Thus, an emitter's radiative decay time can be controled by tailoring the surrounding material and geometry which would in turn determine the allowable photon states or eigenmodes in the system. Following from the Fermi Golden rule, which describes the transition rate between quantum states, the spontaneous photon emission rate Γ of an emitter can be expressed as [15]:

$$\Gamma(\omega, \mathbf{r}, \mathbf{n}_e) = \frac{\pi \mu^2 \omega}{3\hbar\epsilon_0} N(\omega, \mathbf{r}, \mathbf{n}_e) \tag{2.6.1}$$

where μ is the transition dipole moment, $\mathbf{n}_e$ is the dipole moment orientation, $\mathbf{r}$ is the position of the emitter, $N(\omega, \mathbf{r}, \mathbf{n}_e)$ is the photon local density of states (LDOS). In terms of normal modes (normalized eigenfield profile) in the system, the LDOS can be expressed as:

$$N(\omega, \mathbf{r}, \mathbf{n}_e) = 3 \sum_{\xi,\omega'} |\mathbf{n}_e \cdot \mathbf{u}_{\xi,\omega'}|^2 \delta(\omega' - \omega) \tag{2.6.2}$$

where ξ is the mode label and $\mathbf{u}_{\xi,\omega}$ are the normal modes. The summation in (2.6.2) runs through all the possible normal modes in the system for all possible frequencies ω, thus, it contains the contribution of each possible photon transition.

As a consequence of the term $|\mathbf{n}_e \cdot \mathbf{u}_{\xi,\omega}|^2$ in equation (2.6.2), the emission of a photon from a certain emitter would depend on the eigenfield profile of each available mode in the system. This term also shows that the emission of a photon depends on the emitter spatial position relative to the the eigenfield profile intensity distribution. There would be no photon emission to states whose eigenfield profile intensity is zero at the emitter position. On the other hand, placing an emitter at positions where the eigenfield intensity of available modes is high would result in a high emission rate to those modes or photonic states. In chapter 7 of the thesis, spontaneous emission enhancement utilizing plasmonic nanostructures is demonstrated. The eigenmodes of plasmonic structures tend to have a strong near field intensity, which translates to a high LDOS and to a faster radiative decay rate.

2.7 Finite element calculations for electromagnetic wave problems

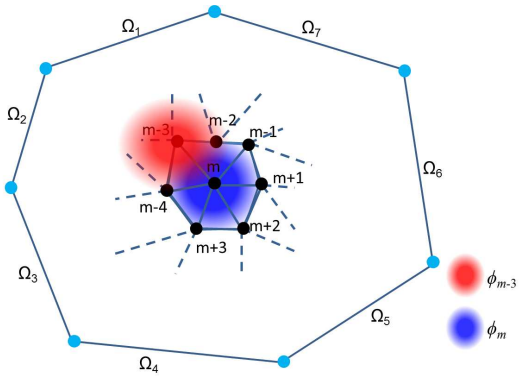

Figure 2.7: Discretized computational domain sketch

The photonic calculations in this work were largely done using finite elements through the commercial program COMSOL. A section in this chapter is thus ded-

icated to briefly summarize the finite element method. For simplicity in notation, here only scalar single frequency waves are considered and the $\exp(-i\omega t)$ frequency dependent term is omitted in the equations below.

In finite elements one utilizes a discrete amount of spatially localized functions to approximate the true solution in a certain domain [16]. Suppose that $E(\mathbf{r})$ is a solution of the Helmholtz (2.1.3) at a single frequency in a certain structure described by $n(\mathbf{r})$. Suppose additionally that $E(\mathbf{r})$ fulfills the conditions $F_l(E(\mathbf{r}))_{\Omega_l}$ imposed at the boundaries Ω_l of the system (Figure 2.7). The finite element method subdivides the domain of interest into a finite amount of node points and will approximate the true solution $E(\mathbf{r})$ with the function

$$\Psi = \sum_m \alpha_m \phi_m(\mathbf{r} - \mathbf{r}_m) \tag{2.7.1}$$

where ϕ_m are local basis functions that only exist in a spatial region around a node with the index m as shown in Figure 2.7, $\mathbf{r}_m$ is the position of node m, and α_m is the amplitude of that particular basis function which will be calculated. Thus, $\sum_{\text{around}m} \alpha_m \phi_m(\mathbf{r}-\mathbf{r}_m)$ approximates the true solution $E(\mathbf{r})$ in the spatial region around node m. Essentially there is still a lot of freedom in choosing the node positions (meshing) and the form of ϕ_m. One can even define different forms of ϕ_m at different nodes. However, as ϕ_m is meant to fulfill the Maxwell equation in this case, care should be taken such that one does not pick a mathematical form that cannot fulfill the continuity conditions set by Maxwell. These choices can heavily affect how good one can approximate the real solution and how fine the spatial discretization should be.

Once the domain of interest is subdivided into m nodes (meshed) and for each element m is assigned, what is left to do is finding the best set of α_m which would minimize the difference between $E(\mathbf{r})$ and Ψ, the residual error. One can do this by inserting (2.7.1) to the left hand side of (2.1.3) and search for a set of α_m with which the residual error would be orthogonal to the basis functions. This approach is known as the Galerkin finite element method. Having the residue to be orthogonal to the basis functions means that the best possible set of α_m is already used and that the error can only be reduced if we introduce other basis functions that are orthogonal to the ones used. Mathematically this means we try to fulfill the equation:

$$\int \phi_n \left(\nabla \times \nabla \times \left[\sum_m \alpha_m \phi_m \right] - (k_0 n(\mathbf{r}))^2 \left[\sum_m \alpha_m \phi_m) \right] \right) dV = \int \phi_n R dV = 0 \tag{2.7.2}$$

for all ϕ_m where R is the residual error. From this condition, one obtains expressions for the interior points. The expressions at the domain edges depend on the imposed boundary conditions. One ends up with a matrix system that can be

solved with any matrix solver:

$$\begin{bmatrix} M_{11} & M_{12} & \cdots & M_{1m} \\ M_{21} & \ddots & \ddots & \vdots \\ \vdots & \ddots & \ddots & \vdots \\ M_{n1} & \cdots & \cdots & M_{nm} \end{bmatrix} \begin{bmatrix} \alpha_1 \\ \alpha_2 \\ \vdots \\ \alpha_m \end{bmatrix} = \begin{bmatrix} b_1 \\ b_2 \\ \vdots \\ b_n \end{bmatrix} \tag{2.7.3}$$

where M_{nm} components are obtained from the lefthand side integral of (2.7.2). The right hand side vector b_n gives additional contributions from imposed boundary conditions at the edges of the computational domain and internal source terms (e.g. contribution from point dipole sources). We have $b_n = 0$ at interior nodes which are not connected to a computational boundary and do not have any additional source term. Note that one can have more basis components in each spatial element m such that $\Psi = \sum_m \alpha_m \phi_m + \beta_m \varphi_m + ...$ This is the case when one wishes to include higher order terms in order to improve accuracy. In such cases one would also need to ensure that the residue is zero for all the terms at each node.

The research done in this work involves field calculations for both driven and undriven systems. In driven system calculations we simulate plane waves interacting with various structures of interest. Typically, performing such simulations requires one to set an excitation condition at a certain boundary in the computational domain. Such boundary conditions are often known as port boundary conditions. Care should be taken to avoid unphysical reflection of returning waves at such boundaries. Implementation techniques of various excitation boundary conditions can be found in the literature [16].

Another way to simulate a certain incoming wave interacting with structures of interest is by utilizing the scattered field formulation. In this formulation, the total field $\tilde{\mathbf{E}}_{\mathrm{total}}$ is reformulated as $\tilde{\mathbf{E}}_{\mathrm{total}} = \tilde{\mathbf{E}}_{\mathrm{input}} + \tilde{\mathbf{E}}_{\mathrm{scat}}$ where $\tilde{\mathbf{E}}_{\mathrm{input}}$ and $\tilde{\mathbf{E}}_{\mathrm{scat}}$ is the input field and the scattered field respectively. $\tilde{\mathbf{E}}_{\mathrm{input}}$ is a known solution of the Helmholtz equation in a system described by $n_0(\mathbf{r})$ while $\tilde{\mathbf{E}}_{\mathrm{total}}$ is the solution of a system described by $n(\mathbf{r}) = n_0(\mathbf{r}) + \Delta n(\mathbf{r})$. In such a formulation, one solves for the scattered field. We thus solve the reformulated Helmholtz equation:

$$\nabla \times \nabla \times \tilde{\mathbf{E}}_{\mathrm{scat}}(\mathbf{r}) - \left(k_0 n_0(\mathbf{r})\right)^2 \tilde{\mathbf{E}}_{\mathrm{scat}}(\mathbf{r}) = k_0^2 \Delta n(\mathbf{r}) \tilde{\mathbf{E}}_{\mathrm{input}}(\mathbf{r}) \tag{2.7.4}$$

where $\tilde{\mathbf{E}}_{\mathrm{input}}$ fulfills:

$$\nabla \times \nabla \times \tilde{\mathbf{E}}_{\mathrm{input}}(\mathbf{r}) - \left(k_0 n_0(\mathbf{r})\right)^2 \tilde{\mathbf{E}}_{\mathrm{input}}(\mathbf{r}) = 0 \tag{2.7.5}$$

The advantage of this formulation is the possibility to readily define throughout the whole domain any $\tilde{\mathbf{E}}_{\mathrm{input}}$ that we desire.

In the undriven system calculations we seek to find the eigenmodes of the structures. As mentioned before these eigenmodes are functions that fulfill (2.1.3) and all the boundary conditions of the system without any external source of input

or excitation within the domain. In the approximate discretized system, we search for the eigenvalues and eigenvectors of the matrix equation (2.7.3). Methods to find eigenvalues and eigenvectors of a matrix can be found in literature [17].

The work done here also focuses heavily on investigating nanostructures with certain periodicities. Such systems are numerically addressed by just simulating a single cell period with additional conditions imposed at the appropriate boundaries to account for the periodicity. The imposed condition to account for periodicity is an equation that connects the field at one boundary to the field at the corresponding boundary pair. One thus additionally imposes the equation:

$$\tilde{\mathbf{E}}_{\Omega_A} = \tilde{\mathbf{E}}_{\Omega_B} \exp(i\theta) \tag{2.7.6}$$

where $\mathbf{E}_{\Omega_A}$ and $\mathbf{E}_{\Omega_B}$ are the field at the correlated Ω_A and Ω_B boundaries respectively. Through this equation we are forcing the field at the Ω_A boundary to have a definite relation with the field at the Ω_B boundary multiplied by a certain phase term of our choosing. The phase term $\exp(i\theta)$ depends on what is simulated. In the case of simulating incoming plane wave with angled incidence, the boundary condition phase term should match the phase term of the incoming plane wave. Such periodic boundary conditions with additional phase dependence are known as Floquet-Bloch periodic boundary conditions.

The EM wave calculations done in this work typically involve open homogeneous domains that stretch to infinity. To model such open domains, Perfectly Match Layers (PML) are employed at the computational domain boundaries. A PML is essentially a numerical artificial layer that attenuates waves propagating inside it due to its added absorption capability in its material properties. With proper choice of artificial material properties, the reflection between the PML with the normal computational domain can be minimized and waves entering the PML can be efficiently attenuated within a limited PML thickness.

A more in depth discussion on finite element methods for electromagnetic applications and the utilized boundary conditions is found in the literature [16].

References

[1] J. D. Jackson. *Classical Electrodynamics*, volume 2011. Wiley, third edition, 1998.

[2] M. O. Scully and M. S. Zubairy. *Quantum Optics*. Cambridge University Press, first edition, 1997.

[3] A. Yariv and P. Yeh. *Photonics: Optical Electronics in Modern Communications*. Oxford University Press, USA, 6 edition, 2006.

[4] J. D. Joannopoulos, S. G. Johnson, J. N. Winn, and R. D. Mead. *Photonic Crystals: Molding the Flow of Light*. Princeton University Press, Princeton, 2nd edition, 2008.

[5] T. Krauss, R. DeLaRue, and S. Brand. *Two-dimensional photonic-bandgap structures operating at near infrared wavelengths*. Nature, 383(6602):699–702, 1996.

[6] J. W. Goodman. *Introduction to Fourier optics*. McGraw-Hill Higher Education, second edition, 1996.

[7] E. R. Martins, J. Li, Y. Liu, J. Zhou, and T. F. Krauss. *Engineering gratings for light trapping in photovoltaics: The supercell concept*. Physical Review B, 86(4):041404, 2012.

[8] S. A. Maier. *Plasmonics: Fundamentals and Applications*. Springer, New York, USA, 2007.

[9] J. G. Rivas, M. Kuttge, P. H. Bolivar, H. Kurz, and J. A. Sánchez-Gil. *Propagation of Surface Plasmon Polaritons on Semiconductor Gratings*. Physical Review Letters, 93:256804, 2004.

[10] A. Abass, H. Shen, P. Bienstman, and B. Maes. *Angle insensitive enhancement of organic solar cells using metallic gratings*. Journal of Applied Physics, 109(2):023111–7, 2011.

[11] A. G. Brolo. *Plasmonics for future biosensors*. Nature Photonics, 6(11):709–713, 2012.

[12] M. Kauranen and A. V. Zayats. *Nonlinear plasmonics*. Nature Photonics, 6(11):737–748, 2012.

[13] K. R. Catchpole and A. Polman. *Plasmonic solar cells*. Optics Express, 16(26):21793–21800, 2008.

[14] H. Shen, P. Bienstman, and B. Maes. *Plasmonic absorption enhancement in organic solar cells with thin active layers*. Journal of Applied Physics, 106(7), 2009.

[15] L. Novotny and B. Hecht. *Principles of Nano-Optics*. Cambridge University, Cambridge, 2006.

[16] J. Jin. *The Finite Element Method in Electromagnetics*. Wiley-IEEE Press, third edition, 2014.

[17] E. Isaacson. *Analysis of Numerical Methods*. Courier Dover Publications, first edition, 1994.

3
Basic solar cell concepts

3.1 Introduction

This chapter discusses basic semiconductor and solar cell concepts relevant to the work. Section 3.2 describes the current and voltage generation process in solar cells. The relevant carrier recombination mechanisms which will impede a solar cell performance are presented in Section 3.3. Section 3.4 elaborate on the relevant measurement methods used in this work to characterize thin-film poly-Si solar cells. Section 3.5 gives a brief summary of the current solar cell technologies.

3.2 Solar cell operation

The conversion of sunlight to electrical power firstly involves the generation of electron-hole pairs, which carry negative and positive charge respectively, at the expense of absorbed photons. These generated carriers, however, can recombine and release their energy as heat (nonradiative recombination) or photons (radiative recombination) without contributing to an external current. There needs to be a mechanism that separates generated electron-hole pairs and forces them to recombine only through an external circuit.

Another main factor that should be considered in a solar cell is its output voltage, which is affected by the energy each electron has as it goes to the external circuit. Without enough voltage the solar cell device does not produce significant power even though it generates current. In most solid materials high energy free

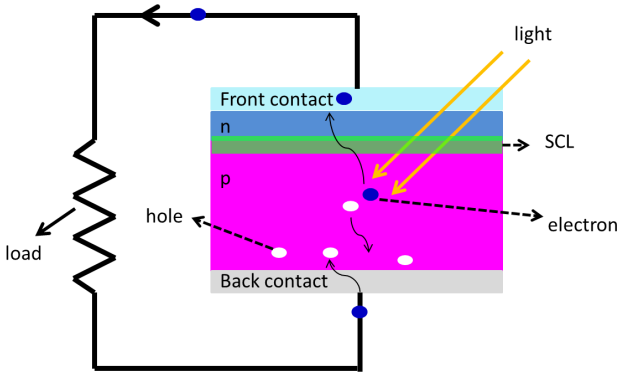

Figure 3.1: pn junction solar cell

carriers would quickly lose their energy as heat (as lattice vibrations or phonons) due to collisions with their surroundings. This is a thermalization process which can occur in a very short time scale. In silicon an excited hot electron in the conduction band falls to the bottom of the band typically within 1 ps or less [1, 2]. If there are no restrictions, thermalization could limit the voltage output of a solar cell as the charge carriers would be left with a very low potential energy.

To avoid severe energy loss from carrier thermalization, one can opt for materials which have a significant energy bandgap and impede this process at the band edge. A significant energy distance between allowable states would minimize the energy loss probability due to thermalization as the process would require the simultaneous excitation of multiple phonons. However, care must be taken as a significant bandgap also means that one forbids the absorption of low energy photons which translates to less generated light current.

These two requirements of charge carrier separation and ensuring a sufficient potential energy can be met with semiconductor structures. Semiconductor materials can have a bandgap close to 1.34 eV, which is the optimal value in the Shockley-Queisser limit for solar cells [3]. A semiconductor pn junction also has a significant electric field in its space charge layer (SCL), which can separate charge carriers. These advantages have made semiconductor based solar cells a popular option.

Figure 3.1 shows a diagram of the solar cell current generation process for a typical pn junction cell. It presents a photon absorption process that leads to electron hole pair generation in the p-type absorber layer. The electrons which are minority charge carriers have to diffuse to the space charge layer (SCL) before being able to contribute to an external current. During this diffusion process, generated electrons may recombine with the holes in the absorber layer through various mechanisms that are discussed later. A long minority carrier diffusion

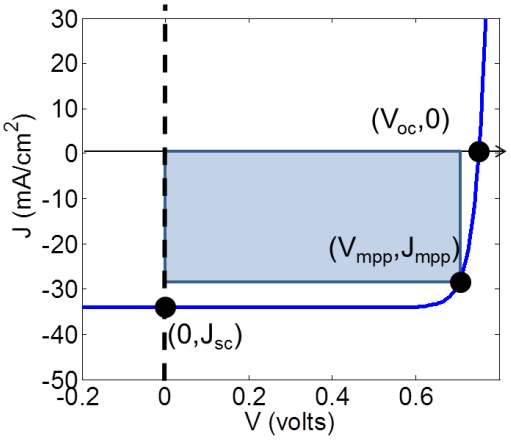

Figure 3.2: current voltage ($J-V$) characteristics of a pn junction solar cell

length is needed to have a good solar cell.

Generated electrons that reach the SCL are swept by the electric field to the n-type layer. On the other hand, holes in the p-type absorber layer with insufficient kinetic energy will be prevented from reaching the n-type layer. The SCL electric field basically allows the passage of minority carriers from each layer while blocking majority carriers. If the two layers are connected with an external circuit as shown in Figure 3.1, excess carriers in both layers ideally induce an external current due to the potential difference, before they will recombine. A typical plot of an ideal current-voltage ($J-V$) characteristic of a pn junction solar cell is shown in Figure 3.2. There, the current per unit area J flowing out of a solar cell is described by the equation [4]:

$$J = J_0 \left[\exp\left(\frac{eV}{\zeta kT} \right) - 1 \right] - J_L \tag{3.2.1}$$

where k is the Boltzman constant, e is the electron charge, V is the applied voltage and J_L is the light induced current per unit area. Both ζ and J_0, which are the diode ideality factor and saturation current per unit area respectively, are discussed in detail in the next section. J_L is given by:

$$J_L = q \int_0^{\lambda_m} \Phi(\lambda) EQE(\lambda) d\lambda \tag{3.2.2}$$

where $\Phi(\lambda)$ is the solar spectral distribution, $EQE(\lambda)$ is the external quantum efficiency. $EQE(\lambda)$ can be obtained from semiconductor transport calculations provided we know the carrier generation rate (photon absorption profile) throughout the cell and the diffusion constants. For the case of crystalline-silicon (c-Si)

cells with bandgap of E_g = 1.12 eV and the AM 1.5G solar radiation spectrum, the photocurrent is about 42 mA/cm^2 when all electron hole pairs created by photon absorption are separated and collected at the contacts (EQE=1). In practice, this ideal photocurrent is almost attained in the very best c-Si cells.

The first term in equation (3.2.1) describes the forward bias diode current which counteracts the light generated current flow. This first term is physically due to the voltage difference between the p and n contacts which generate an electric field that counteracts the junction electric field. As the forward voltage increases, the electric field of the junction would become weaker and majority carrier diffusion, which passes the SCL, would become more significant. Due to this, generated charge carriers are more likely to recombine before contributing to an external current. If the recombination mainly happens in the bulk quasi neutral region (QNR), the diode ideality factor will be $\zeta = 1$.

At a certain forward voltage V_{oc} the solar cell device will behave in an open circuit condition ($J = 0$) and there is no electrical current flowing out of the solar cell. An ideal value is $V_{oc} = E_g/q$ however it is lower due to recombination. For c-Si solar cells, recombination in practice limits the V_{oc} to about 0.7 V. A solar cell is thus a high current, low voltage device. Hence solar cells are always connected in series in panels, to obtain practical output voltage.

As can be seen from Figure 3.2, a solar cell device has an optimum operating voltage point at which it has the most power output. Beyond this optimum point the recombination current would be too big and one extracts too little current though there is higher voltage. The efficiency of the solar cell is:

$$\eta = \frac{J_{mpp} V_{mpp}}{P_{inc}} \tag{3.2.3}$$

where V_{mpp} is the optimum forward voltage point and J_{mpp} is the current per unit area at V_{mpp} . P_{inc} is the incoming solar radiation power on the cell.

In the presence of an additional shunting path with shunt resistance R_{sh} and additional external series resistance R_s in the circuit, the $J - V$ characteristic expression is modified into

$$J = J_0 \left[\exp\left(\frac{qV - JR_sA}{nkT} \right) - 1 \right] + \frac{qV + JR_sA}{R_{shA}} - J_L \tag{3.2.4}$$

A useful measure that indicates whether a solar device is operating optimally or under the influence of strong parasitic effects is the fill factor FF:

$$FF = \frac{J_{mpp} V_{mpp}}{J_{sc} V_{oc}} \tag{3.2.5}$$

The FF is a measure of the 'squareness' of a solar cell J-V characteristic. A low FF can indicate the presence of strong parasitic effects or additional recombination mechanisms.

An additional shunting path with relatively large shunt resistance will mainly cause a detriment to the FF factor if ($R_{sh}A \geq V_{oc}/J_{sc}$). When $R_{sh}A < V_{oc}/J_{sc}$, then the V_{oc} is also affected. In the presence of a significant series resistance, a shunting path with low shunt resistance also causes a significant decrease in the photocurrent due to the parasitic term ($\frac{qV+JR_sA}{R_{shA}}$) in (3.2.4). A parasitic external series resistance also mainly reduces FF when $R_sA \ll V_{oc}/J_{sc}$. At large parasitic series resistance $R_sA \geq V_{oc}/J_{sc}$, J_{sc} is also significantly reduced and $FF \approx 0.25$.

3.3 Recombination mechanisms in solar cells

There are many possible carrier recombination routes that can hinder a solar cell's performance. Carrier recombination can occur in the bulk, at interfaces, and even in the SCL. Most of the possible recombination routes are nonradiative in nature. Furthermore, in most solar cells, nonradiative mechanisms are stronger, with some exceptions in few direct bandgap semiconductors and organic materials, e.g. GaAs and more generally III-V compounds. These recombination mechanisms may manifest themselves in the modification of the diode saturation current J_0 and ideality factor ζ or even another saturation current term. Strong recombination mechanisms can decrease the J_{sc}, V_{oc}, and FF of a solar cell device. Different recombination mechanisms have different effects on the solar cell parameters.

In the presence of significant recombination in both the QNR and SCL regions, the current voltage relation can be described with:

$$J = J_{01}\left[\exp\left(\frac{qV}{1kT}\right) - 1\right] + J_{02}\left[\exp\left(\frac{qV}{2kT}\right) - 1\right] - J_L \tag{3.3.1}$$

The additional second diode current term with ideality factor $\zeta = 2$ describes the recombination in the SCL. J_{01} follows the expression

$$J_{01} = \frac{qDn_i^2}{N_d}\frac{1}{L} \tag{3.3.2}$$

where D is the diffusion constant, N_d is the doping constant and L is the carrier diffusion length. J_{02} follows:

$$J_{02} = \frac{q\pi Dn_iV_t}{F_{max}}\frac{1}{L^2} \tag{3.3.3}$$

where n_i is the intrinsic charge concentration, $V_t = \frac{kT}{q}$ is the thermal voltage and F_{max} is the maximum electric field in the SCL region. There may still be other recombination components that require another modification of the $J - V$ expression. To a certain a limit, the presence of other recombination mechanisms

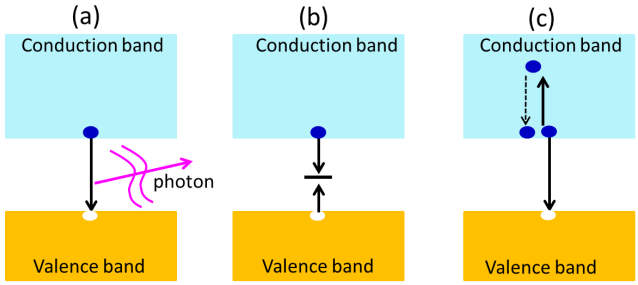

Figure 3.3: Possible recombination mechanisms in semiconductors: (a) band to band radiative recombination, (b) nonradiative recombination through a defect, (c) non-radiative Auger recombination.

can still be modeled with the two diode model with different ideality factors and saturation currents.

There are some mechanisms that affect the bulk diffusion length of charge carriers. One of them is the band to band radiative recombination, which is more dominant in direct bandgap materials (Figure 3.3a). In indirect bandgap materials, this radiative recombination is less likely to occur as it would need to involve a phonon excitation due to the momentum mismatch between the carrier states at the band edge. Typically, radiative recombination is more preferable than nonradiative recombinations due to the chance to still manipulate the re-emitted photon. However, most re-emitted photons from band to band recombination have the bandgap energy due to the thermalization process, and are thus less likely to be reabsorbed. As minority charge carriers move in the bulk of an absorber layer by diffusion, they can encounter bulk defects which may act as recombination centers (Figure 3.3b). These defects are spatially localized and can occur due to unintentionally introduced impurities or lattice imperfections. Such defects can act as trap states within the bandgap. Recombination through defect levels in the bandgap region is widely known as Shockley-Read-Hall recombination and is expressed by:

$$U_{SRH} = v_{th} N_t \frac{\sigma_n \sigma_p (n_e n_h - n_i^2)}{\sigma_n (n_e + n_t) + \sigma_p (n_h + p_t)} \tag{3.3.4}$$

where $p_t = n_i \exp\left(\frac{E_i - E_t}{kT}\right)$, $n_t = n_i \exp\left(\frac{E_t - E_i}{kT}\right)$, E_t is the defect level energy, E_i is the intrinsic level energy, n_e is the electron concentration, n_h is the hole concentration, n_i is the intrinsic carrier concentration, N_t is the defect concentration, σ_n and σ_p are the electron and hole capture cross-sections. An important general rule of thumb of SRH recombination can be seen by inspecting the simple case

$\sigma_n = \sigma_p = \sigma$ where one finds:

$$U_{SRH} = v_{th} N_t \frac{\sigma(n_e n_h - n_i^2)}{n_e + n_h + 2n_i \cosh\left(\frac{E_t - E_i}{kT}\right)} \tag{3.3.5}$$

From the cosh term in the denominator of (3.3.5), we see that SRH recombination will only be effective when the defect energy is close to the midgap $E_t \approx E_i$. Trap states close to a band edge (shallow traps) will not effectively contribute to the recombination. Thus, a large amount of deep level defects in a certain material will translate to a smaller carrier diffusion length. Deep level trap states tend to be the dominant cause of recombination in indirect bandgap materials such as Si. This is due to the fact that there is no momentum restriction for the carrier trapping process by spatially localized defects.

Though shallow traps do not effectively contribute to recombination, they can affect the charge/doping concentration of the semiconductor layer. The occupation probability of a defect level by electrons f_t is governed by the equation:

$$f_t = \frac{\sigma_n n_e + \sigma_p p_t}{\sigma_n(n_e + n_t) + \sigma_p(n_h + p_t)} \tag{3.3.6}$$

The occupation of a defect level by holes (the absence of electrons) is expressed by $1 - f_t$. How the trap states will affect the doping concentration depends on the type of traps, and the position of the Fermi level. For example an acceptor type defect in an n-type semiconductor contributes as an acceptor dopant, and a donor like defect in a p-type semiconductor acts as a donor dopant.

Carrier recombination can also occur without the emission of photons and phonons (at least indirectly). An electron and a hole can recombine by giving their energy directly to a nearby carrier (Figure 3.3c). This carrier will be excited to a higher energy state, though often it will quickly lose its energy afterwards by thermalization. Such recombination occurs when the carrier density is high either due to high level injection or doping. Under strong sunlight concentration, the carrier generation (injection level) may also be high enough to make this mechanism significant. This recombination process is known as Auger recombination.

The band to band, SRH, and Auger recombination mechanisms affect the $J-V$ characteristic of the cell by influencing the carrier lifetime. In the presence of these mechanisms, the carrier lifetime is expressed by:

$$\frac{1}{\tau} = \frac{1}{\tau_R} + \frac{1}{\tau_T} + \frac{1}{\tau_{Aug}} \tag{3.3.7}$$

where τ is the effective lifetime, τ_R is the lifetime of the radiative recombination process, τ_T is the lifetime of the SRH recombination, and τ_{Aug} is the lifetime of the Auger recombination. The diffusion length is affected by these mechanisms through the relation:

$$L = \sqrt{D\tau} \tag{3.3.8}$$

Under low injection conditions (normal sunlight illumination of a solar cell), the radiative and Auger minority carrier recombination mechanisms depend on the doping density (shown here for n-type, but there is a similar dependence for p-type) as such:

$$\begin{aligned} \tau_R &= \frac{\text{const}}{N_D} \\ \tau_{Aug} &= \frac{\text{const}}{N_D^2} \end{aligned} \tag{3.3.9}$$

This dependence is to be expected as one requires the existence of other charge carriers. The higher power dependence of Auger recombination lifetime (τ_{Aug}) on doping density is understood as this mechanism involves more than one majority carrier charge particle. As the doping process at times leads to the introduction of additional unwanted trap states, one also finds that the SRH lifetime is lower for highly doped layers; though this is not fundamentally the case and depends on the fabrication process. In general, as one goes to high doping concentration, the lifetime of the minority carrier decreases. At lattice discontinuities of a semiconductor

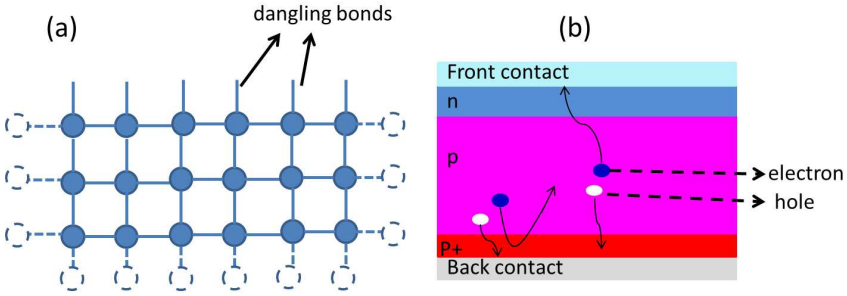

Figure 3.4: (a) Dangling bonds at a lattice discontinuity. (b) An example solar cell device with a BSF layer (P+) at the back contact

there are dangling bonds which can act as trap states that support efficient carrier recombination (Figure 3.4a). Due to this the carrier concentration tends to be low near a semiconductor interface and this promotes carrier diffusion from the bulk towards the interface. The metal contact-semiconductor interface in a solar cell device can also have such interface trap states, which act as efficient recombination centers for minority carriers. In the case of a flat solar cell structure where the current flow is 1D in nature, the effect of contact surface recombination along with finite thickness of the cell can be lumped into an effective change of the diffusion length through the expression [5, 6]:

$$L_{mono} = L \frac{\cosh\left(\frac{d'}{L}\right) + \frac{SL}{D}\sinh\left(\frac{d'}{L}\right)}{\sinh\left(\frac{d'}{L}\right) + \frac{SL}{D}\cosh\left(\frac{d'}{L}\right)} \tag{3.3.10}$$

where L is the diffusion length, d' is the width of the quasi neutral region, L_{mono} is the new effective diffusion length which takes into account the contact recombinations and the finite thickness of the cell. The L in the expression (3.3.2) will be be replaced by this L_{mono}.

To avoid the recombination of minority carriers at the contacts, another semiconductor junction, which has an electric field that repels minority carriers from the contacts, can be introduced. This is done by doping the region close to the contact higher than the rest of the layer as shown in Figure 3.4b. This higher doping region close to the contact is often referred to as a back or front surface field layer (BSF or FSF, respectively), depending whether it is on the front or back contact of the cell. Introducing such a BSF or FSF layer effectively decreases the surface contact recombination S.

The BSF and FSF layers are typically very highly doped often reaching $N_d \geq 10^{19}$ cm^{-3}. This high doping is needed to generate a strong enough electric field that effectively repels minority carriers. Due to this high doping, there is a high defect concentration and significant Auger recombination which results in a low minority carrier diffusion length in the BSF layer. Generated charge carriers in the BSF layer are most likely to recombine. Due to this, these layers are typically very thin. The boundary between the BSF and the normal layer is also typically made very abrupt to avoid additional recombination centers in the main absorber layer.

Naturally, a layer of semiconductor polycrystalline material consists of grains, with boundaries that have interface defects. This is one of the reasons why polycrystalline materials tend to have a lower diffusion length as compared to its monocrystalline counterpart. The grain boundaries in the polycrystalline material can be efficient recombination sites if not properly passivated. Brendel and Rau have calculated the influence of grain boundary recombination on the effective carrier diffusion length [5]. The diffusion length of a single polycrystalline layer consisting of vertically oriented grains can be described with the equation:

$$L_{poly} = \frac{L_{mono}}{\sqrt{1 + \frac{2S_{GB}L_{mono}^2}{Dg}}} \tag{3.3.11}$$

where S_{GB} is the grain boundary recombination velocity and g is the grain diameter (horizontal or in plane size). As can be seen in (3.3.11), smaller grains or a faster grain boundary recombination rate would result in a smaller effective diffusion length. When grain boundary recombination is considered, the L in the expression (3.3.2) will be be replaced by L_{poly}.

Grain boundary recombination always increases the total recombination in a cell, as apparent from (3.3.11): $L_{poly} \leq L_{mono}$. However, its influence is only apparent when L_{mono} is high enough above a certain value. In particular this happens when $\frac{2S_{GB}L_{mono}^2}{Dg} \approx 1$, so when the denominator of (3.3.11) starts to be affected heavily by L_{mono}. Note that this bordering limit of L_{mono} depends

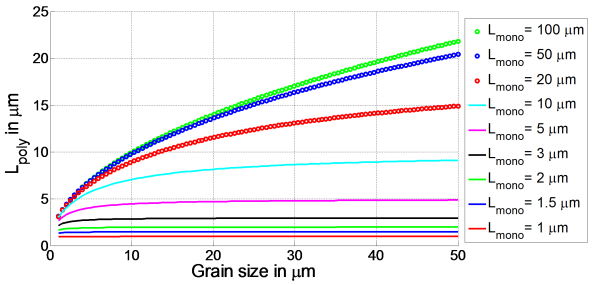

Figure 3.5: Effective diffusion length in polycrystalline silicon as a function of grain size g calculated by (3.3.11), with S_{GB}= 104 cm/s and D = 20 cm^2/s. L_{mono} was used as the parameter.

on the grain diameter and grain boundary recombination velocity values around which the calculations are done. This is illustrated in Figure 3.5 where the grain size is varied between 1 and 50 μm for different L_{mono} taking realistic S_{GB} and D values. For $L_{mono} < 10$ μm and relatively small grain diameter of several tens of μm, $L_{poly} \approx L_{mono}$. However, at $L_{mono} \geq 10$ μm, L_{poly} has not reached L_{mono} even when the grain diameter is 50 μm. More in depth discussion of the effects of grain boundary recombination is provided in chapter 7 .

3.4 Solar cell characterization methods

3.4.1 Capacitance-voltage measurements

Typically, a semiconductor solar cell structure would have its emitter layer strongly doped (either a pn$^+$ or p$^+$n junction) in order to have a large potential difference between each layer (built in voltage). In such cases the SCL region mainly extends to the least doped side and applying a voltage only changes the width of the SCL region there. For the case of homogeneous doping the capacitance of the SCL region C_j of n$^+$p or p$^+$n junction is expressed by:

$$C_j = \frac{\epsilon_0 \epsilon_s}{W} = \sqrt{\frac{q\epsilon_0 \epsilon_s N_l}{2(V_{bi} - V)}} \tag{3.4.1}$$

where ϵ_0 is the permittivity of vacuum, ϵ_s is the relative permittivity of the least doped side, W is the width of the depletion layer, V_{bi} is the built in potential, and N_l is the doping concentration in the least doped side of the junction. The capacitance contribution of the SCL region is typically called the junction capacitance. One can reformulate the expression for C_j to obtain the Mott-Schottky relation [4]:

$$\frac{1}{C_j^2} = \frac{2(V_{bi} - V)}{q\epsilon_0 \epsilon_s N_l} \tag{3.4.2}$$

from which one can obtain the doping. In the case of nonuniform doping (3.4.1) can be generalized into the form [7]:

$$\frac{d\left(1/C_j^2\right)}{dV} = -\frac{2}{q\epsilon_0\epsilon_s N_l} \tag{3.4.3}$$

One can essentially utilize expression (3.4.1) to obtain the position dependence of the doping density by measuring the capacitance at different bias voltage. Capacitance voltage (C-V) measurements are performed utilizing a four point probe setup. An impedance analyzer HP 4192A LF (5Hz-13MHz) was used to obtain the C-V spectra. The program MIA, written by J. Verschraegen, is used to control the impedance analyzer equipment [8].

3.4.2 Capacitance-frequency measurements

Defect levels can contribute to the junction capacitance of a solar cell due to their carrier trapping capability if they do not also act as efficient recombination centers. However by the same token, this essentially means one can deduce the defect distributions from the capacitance measurements [9]. Contribution of defect states to the capacitance is expressed by [9, 10]:

$$C = \left(\frac{q}{\tilde{u}_{ext}}\right)\left(\left[\int_{x_1}^{W_p} \tilde{u}_p(x) N_t\left(E_F(x)\right) dx\right] + \left[\int_{x_2}^{W_n} \tilde{u}_n(x) N_t\left(E_F(x)\right) dx\right]\right) \tag{3.4.4}$$

where E_F is the Fermi energy, $\tilde{u}_{ext}$ is the external applied AC voltage signal, $q\tilde{u}_{p,n}$ is the local shift of the quasi Fermi level of each charge carrier due to $\tilde{u}_{ext}$, N_t is the defect concentration. Each spatial integration term is the contribution of defects from the p and n side of the SCL layer, respectively. Note that the defects that effectively contribute to capacitance are those whose energy level crosses the Fermi energy. If a defect level at a certain position is far below the Fermi level, it is always occupied by electrons, and its occupation does not vary with small AC perturbations caused by the small AC voltage signal used to measure the capacitance: this defect at this position does not contribute to the capacitance. A similar conclusion is obtained for the case when the defect level is far above the Fermi level. Only defects whose level crosses the Fermi level at a certain position do change their occupation with AC voltage; they are probed with C-f measurement and analysis if the frequency of the AC voltage is low enough to allow the defect to adapt its occupation. If the C-f measurement is not done in equilibrium conditions, that is, when either a DC voltage or bias illumination is applied (or both), the situation becomes complicated because there are two different Fermi levels then, one for electrons and one for holes. This case is discussed by Decock et al. [10]. As we will carry out our C-f measurements in chapter 7 in dark and under zero DC bias voltage, a discussion of the simple equilibrium case is sufficient here.

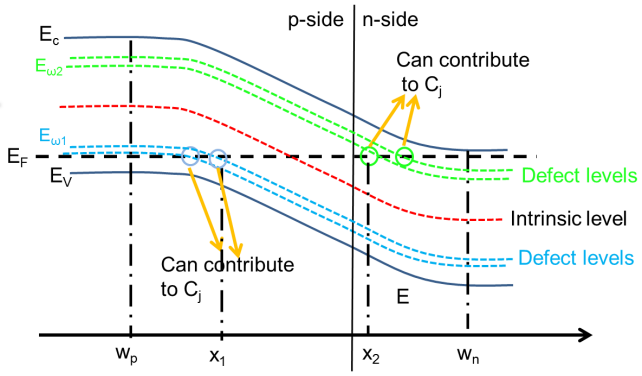

Figure 3.6: Band diagram of a pn$^+$ junction depicting defect levels that can contribute to C_j

In (3.4.4) the integrand's lower limits $x_{1,2}$ mark the position in the SCL region where the Fermi level intersects with energy $E_{\omega_{1,2}}$. $E_{\omega_{1,2}}$ is the maximum defect energy (from the closest band edge) that can contribute to the capacitance for the applied voltage signal's frequency as shown in Figure 3.6. Note that an applied AC voltage signal can only probe the capacitance contribution of defect states if the carrier trapping and escape processes at the defects are fast enough to follow the signal. If the voltage signal is oscillating at a frequency much faster than the characteristic frequency of a defect level, then defects with such energy level cannot contribute to the capacitance that the signal probes. Deeper defect levels would have smaller characteristic frequency f_o and thus require a slower voltage signal. The probed defect energy E_ω follows the expression:

$$E_\omega = kT \ln \frac{2\sigma_{n,p} N_{c,v}}{2\pi f_o} \tag{3.4.5}$$

where $N_{c,v}$ is the conduction/valence band density of states. If one wishes to probe the junction capacitance only, one thus should opt to measure the capacitance at a fairly high frequency to avoid contribution of deeper level defects.

Essentially, the apparent defect distribution in a solar cell N_t depends on the derivative of the measured capacitance with respect to the frequency (C-f). However, one would still need information on the spatial dependence of $\tilde{u}_{n,p}$ in the SCL. This spatial dependence depends on the doping characteristics of the semiconductor layers that form the junction. Assuming a simplified case of $\tilde{u}_p = \tilde{u}_{ext} =$ constant and no other parasitic components are affecting the C-f spectra, the apparent defect distribution N_t is:

$$N_t(E_\omega) = -\frac{V_{bi}}{qW} \frac{dC}{df} \frac{2\pi f}{kT} \tag{3.4.6}$$

One can have difficulty in knowing accurately the $\tilde{u}_{n,p}$ spatial profile, but knowledge of this is indicated from the doping profile of the samples. In the case of a parabolic spatial dependence of $\tilde{u}_p$, common in p^+n or n^+p junctions:

$$N_t(E_\omega) = -\frac{2V_{bi}^{3/2}}{\sqrt{q}W\sqrt{qV_{bi} - (E_g - E_F)}}\frac{dC}{df}\frac{2\pi f}{kT} \tag{3.4.7}$$

The C-f spectrum at a single temperature only gives an incomplete information of the energetical defect distribution. One would also have to obtain the C-f spectra at different temperatures (C-f-T) in order to identify the correct attempt to escape frequencies $\omega_{esc} = \sigma_{n,p}N_{c,v}$ of the defect states, which are needed obtain the defect state energy [9]. ω_{esc} is the rate at which trapped carriers escape the defect in question. Note also that to deduce the concentration of the defect properly, one would need to know V_{bi}, which can be deduced from the C-V measurements that give us the doping density distribution.

Incidentally, measuring the C-f spectra at different temperatures also allows one to probe defects at different energy ranges. At low temperature the thermal energy is low enough such that one can properly probe very shallow defects close to the band edges. At high temperature one measures mainly deeper level defects, as the contribution of shallow defects will be blurred by the high thermal energy. This method of deducing the defect distribution from the C-f-T spectra is widely known as admittance spectroscopy.

The C-f-T measurements were performed with samples placed in a vacuum cryogenic chamber in which liquid nitrogen is pumped to regulate the temperature. A vacuum pump was used to lower the pressure in the chamber reaching 0.1 mbar which is necessary in order to avoid water vapors that would crystallize and contaminate the cell when the chamber is cooled to cryogenic temperatures. The C-f spectrum was obtained with the impedance analyzer HP 4192A LF (5Hz-13MHz). The program MIA is used to control the impedance analyzer equipment. The C-f spectra is measured in the 100 Hz - 1 MHz range. At higher frequencies the impedance analyzer suffers from the parasitic inductance in the equipment, which renders the measured C-f spectra undependable. At lower frequencies there is simply too much noise in the spectrum.

An example measured C-f-T spectra is shown in Figure 3.7. This C-f-T spectra is taken from our measurements of an unhydrogenated poly-Si thin-film cell with p-type absorber layer. More detailed discussion on the measurement results will be given in chapter 7. One can deduce the correct ω_{esc} of the observed defects by first plotting $-\omega\frac{dC}{d\omega}$ versus $\log(f)$ at different temperatures as shown in Figure 3.8. The different peaks that one observes at a certain temperature correspond to contributions of different defect states. In our case, we see two distinct peaks.

By tracking the peak frequencies as temperature is changed, one can obtain information on the correct energy level and ω_{esc} of each observed defect. One

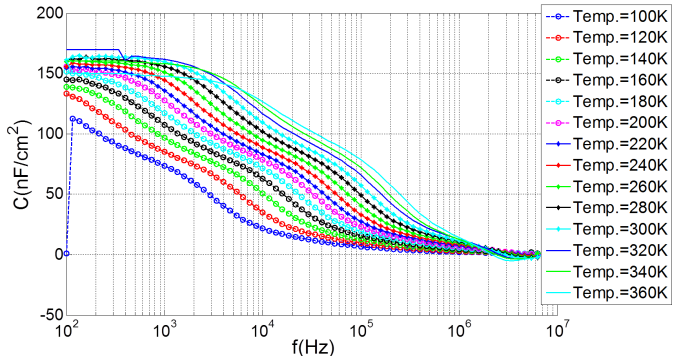

Figure 3.7: Example C-f-T spectra of an unhydrogenated p-type absorber poly-Si sample that is studied in this work.

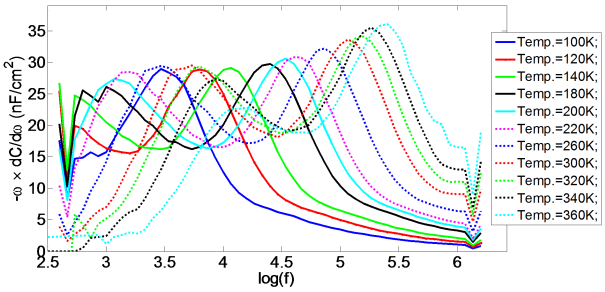

Figure 3.8: $-\omega\frac{dC}{d\omega}$ versus $\log(f)$ at different temperatures of the poly-Si sample of Figure 3.7

essentially rearranges equation (3.4.5) in the form:

$$\ln\frac{\omega}{2} = -\frac{E_\omega}{kT} + \ln\frac{2\omega_{esc}}{2\pi f} \tag{3.4.8}$$

where $\omega = 2\pi f_o$. f_o is the frequency pertaining to the peaks seen in the $-\omega\frac{dC}{d\omega}$ versus $log(f)$ plot. Utilizing (3.4.8) one can perform a fitting procedure commonly known as Arrhenius analysis to obtain the defect energy E_ω and ω_{esc}. The Arrhenius analysis of our data for the two observed peaks is shown in Figure 3.9. In our case here we find 2 distinct defects with different attempt to escape frequencies ω_{esc} (by an order of magnitude), but close characteristic energies.

The deduced defect distribution is calculated assuming a parabolic spatial dependence of $\tilde{u}_p$ (which is the case for our n$^+$p cells here) and shown in Figure 3.10. There we plot the whole spectra twice with two different values of ω_{esc} to demonstrate the effect of assigning an incorrect ω_{esc} value. When calculated assuming the correct ω_{esc}, defect distribution profiles deduced from measurements at differ-

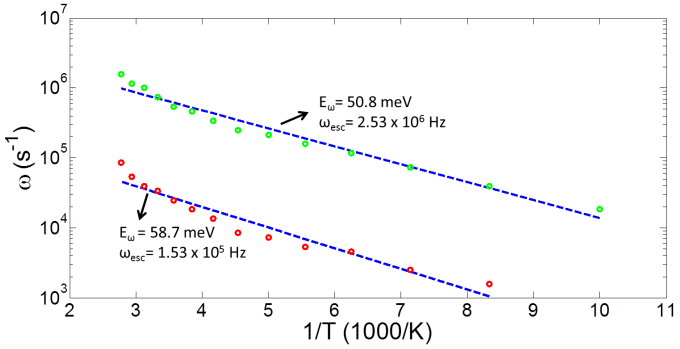

Figure 3.9: Arrhenius analysis of the C-f-T data in Figure 3.7. We utilized data in the temperature range T = 100-360 K in steps of 20 K (at temperature points where the peaks are visible).

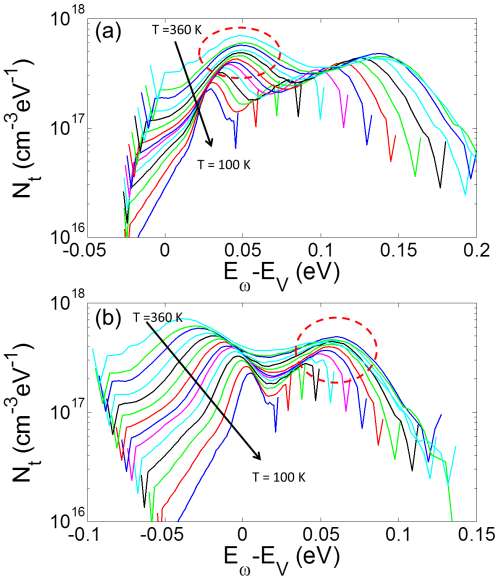

Figure 3.10: Deduced defect distribution plotted at (a) $\omega_{esc} = 2.53 \times 10^6$ Hz and (b) $\omega_{esc} = 1.53 \times 10^5$ Hz.

ent temperatures pertaining to the same defect will overlap. In our case, one can see that we obtain a fairly good overlap of the features deduced at different temperature for each defect. The deviations from a perfect overlap can be attributed to uncertainties such as temperature deviations during the measurements. As the features of the defect spectra originates from different defect types with largely different attempt to escape frequencies, one cannot obtain a good overlap for the

whole spectra with a single value of ω_{esc}.

3.5 Solar cell materials, structures and technologies

Over the years, various competing solar cell technologies based on different materials arise. Each of them has different limitations. Here we briefly present a few technologies and desribe the challenges each faces and we also discuss whether introducing light trapping structures is relevant:

1. (mono)crystalline cells: Typically made with Si, GaAs or other III-V materials. These cells utilizes expensive monocrystalline wafers and are thus rather thick, reaching around 200 μm in the case of typical commercial c-Si cells. Due to the high quality of the monocrystalline material they are based on, these cells can reach high efficiencies fairly close to the theoretical Shockley-Queisser limit for a single junction cell (25% for c-Si and 28% for GaAs) [11]. These cells have reached a fairly advanced state of their technology and can hardly be optimized further electrically. Simple light trapping features are already utilized in commercial cells, which include multilayer antireflection coatings and a surface texturization to provide light scattering. To acquire a large voltage, typical solar panels utilizing these materials have their cells connected in series externally.

   Due to their relatively high costs, people have looked into the possibility of not relying on expensive mono-crystalline wafers. There have been studies on utilizing thin monocrystalline Si films of a few to several tens of μm, either grown directly on another substrate or fabricated via novel epi-free processes for photovoltaic purposes [12, 13]. As c-Si requires the large thickness of several hundreds of μm to have a complete absorption, such thin c-Si films require more advanced light trapping schemes.

2. Multi-crystalline Si cells: As in the previous case, this solar cell technology is wafer based though not mono-crystalline. The crystalline size in these wafers is typically in the mm range, and these cells are also rather thick (≤ 200 μm) exhibiting efficiencies of 18-20% [11]. They are considered to be the work-horse of the commercial photovoltaics market due to their less expensive price as compared to their monocrystalline counterpart. Slight optical optimization can maybe improve the cells, but is usually not considered because of economics (it does not pay off). This type is not considered in this work.

3. Thin-film cells: In the efforts to decrease the costs of solar cells much research was done on alternative fabrication technology and materials. One of the popular directions is the development of solar cells that use less active

materials and thus cost less. As a result, a new class of solar cells with a thin thickness (< 10 μm) appears. A few of these cells could benefit from additional photonic sophistication, but some of them do not, as they are already strongly absorbing while supporting a large carrier diffusion length in the active material. Here we will briefly summarize the current dominant technologies of thin-film solar cells:

(a) Polycrystalline thin-film cells based on CdTe or on the Cu-In-Se materials family: Typical cells in this category are Cu(In,Ga)Se_2 or CIGS cells. The thickness of these cells is typically on the order of 5-10 μm for CdTe and around 2 μm for CIGS with grain size on the order of 1 μm. These cells are made via various thin-film deposition technologies involving evaporation, sputtering, electrochemical methods etc., which are capable of economically coating large areas on the order of 1 m^2. This solar cell technology alternative has also been commercialized, but with less market share than c-Si. Due to the strong absorption in these materials, these cells require only minimal optical sophistication (one antireflection layer, if any). These cells have reached fairly high efficiencies of 21 % for CIGS and 18 % for CdTe [11]. Further photonic sophistication on these cells are usually not considered because they already perform quite well, and it does not pay off. This type is not considered in this work.

(b) Dye-sensitized solar cells or Grätzel cells: These cells typically utilize extremely thin dye layers which act as an active layer that is coated on a random or rough nanostructured conducting surface, which provides for the charge separation and light trapping effect. Early forms of these cells are dye-coated 25 nm thick TiO_2 spheres swimming in an electrolyte encapsulated between glass plates with totals thickness ≈ 10 μm. Another example is ZnO nanowires coated with hybrid organic-inorganic dyes. Efficiencies reaching around 12% are reported for dye sensitized cells [14]. Not considered in this work.

(c) Organic polymer solar cells: These materials are often narrow-band absorbers. They are typically found in a bulk heterojunction structure with two different materials mixed in the active bulk, to address the fact that photon absorption leads to exciton instead of free carrier generation. The excitons typically have a very limited diffusion length and require a heterojunction in order to dissociate, hence the bulk heterojunction structure. Efficiencies of around 10 % have been reported for these single junction organic cells [15]. These cells could take profit from photonic sophistication due to their thinness. This type is not considered in this work.

(d) Amorphous-Si based solar cells: As the name implies, these cells are based on a-Si or alloys such as a-Si:Ge and a-Si:C, and can be combined with microcrystalline Si. The thickness of these cells are limited to 500 nm (and typically 200 nm) for several reasons related to the electrical characteristics: material stability and light induced defects which affect the carrier diffusion length. a-Si cells have been reported to reach an efficiency of 10% [11] and are often used in tandem cell or triple junction structures. These cells have been commercialized but have a much smaller market share than c-Si. With the thickness typically being limited to $<$500 nm, the absorption of light in a-Si is often incomplete. In commercialized a-Si cells, classical optical features have been utilized (thin-film AR, texturized transparent conducting oxides (TCO) as contacts and back reflectors). These cells can still be improved by more photonic sophistication.

(e) Polycrystalline Si (poly-Si) cells: These cells typically have thickness in the 1-10 μm range which is much thinner than their multicrystalline and monocrystalline counterparts. The thin thickness of these cells are mainly motivated by the relatively short carrier diffusion length in the poly-Si films. The grain size found in thin-film poly-Si films are typically in the range of $<$1 to 100 μm range. Due to their smaller grains, they are more prone to grain boundary recombination. In the fabrication of polycrystalline films, one typically first deposits a-Si which is followed by a crystallisation step (see chapter 7). Though there are problematic electrical characteristics, a thin poly-Si film is much cheaper to produce than its mono or multicrystalline counterpart. Currently these cells are not yet at the verge of commercialisation. The present best efficiency of these cells is reported to be around 10% [16]. Poly-Si is a rather poor absorber, and combined with the low layer thickness, incomplete absorption is a concern. They can benefit from additional photonic sophistication for improved light trapping.

In the framework of the IWT-SBO project SiLaSol, we studied and developed light trapping strategies aimed to boost the absorption of several thin-film solar cells by combining photonic structures. We look into the possibility of combining:

1. front and back grating nanostructures (chapter 4)

2. front grating nanostructures with rough back diffusers (chapter 5)

More details on these light trapping approaches are provided in the next chapters.

References

[1] F. E. Doany and D. Grischkowsky. *Measurement of ultrafast hotcarrier relaxation in silicon by thinfilmenhanced, timeresolved reflectivity*. Applied Physics Letters, 52(1):36–38, 1988.

[2] T. Sjodin, H. Petek, and H.-L. Dai. *Ultrafast Carrier Dynamics in Silicon: A Two-Color Transient Reflection Grating Study on a (111) Surface*. Physical Review Letters, 81:5664–5667, 1998.

[3] W. Shockley and H. J. Queisser. *Detailed Balance Limit of Efficiency of pn Junction Solar Cells*. Journal of Applied Physics, 32(3):510–519, 1961.

[4] S. Sze and K. K. Ng. *Physics of semiconductor devices*. Wiley & Sons, 3rd edition, 2007.

[5] R. Brendel and U. Rau. *Injection and collection diffusion lengths of polycrystalline thin-film solar cells*. Solid State Phenomena, 67-8:81–86, 1999.

[6] K. Taretto, U. Rau, and J. H. Werner. *Method to extract diffusion length from solar cell parameters—Application to polycrystalline silicon*. Journal of Applied Physics, 93(9):5447–5455, 2003.

[7] L. C. Kimerling. *Influence of deep traps on the measurement of freecarrier distributions in semiconductors by junction capacitance techniques*. Journal of Applied Physics, 45(4):1839–1845, 1974.

[8] J. Verschraegen. *Karakterisering en modellering met SCAPS van de CISCuT dunne-filmzonnecel*. PhD thesis, Ghent University, 2006.

[9] T. Walter, R. Herberholz, C. Mller, and H. W. Schock. *Determination of defect distributions from admittance measurements and application to Cu(In,Ga)Se2 based heterojunctions*. Journal of Applied Physics, 80(8):4411–4420, 1996.

[10] K. Decock, S. Khelifi, S. Buecheler, F. Pianezzi, A. N. Tiwari, and M. Burgelman. *Defect distributions in thin film solar cells deduced from admittance measurements under different bias voltages*. Journal of Applied Physics, 110(6):063722, 2011.

[11] M. A. Green, K. Emery, Y. Hishikawa, W. Warta, and E. D. Dunlop. *Solar cell efficiency tables (version 43)*. Progress in Photovoltaics: Research and Applications, 22(1):1–9, 2014.

[12] I. Gordon, S. Vallon, A. Mayolet, G. Beaucarne, and J. Poortmans. *Thin-film monocrystalline-silicon solar cells made by a seed layer approach on glass-ceramic substrates*. Solar Energy Materials and Solar Cells, 94(2):381 – 385, 2010.

[13] V. Depauw, Y. Qiu, K. Van Nieuwenhuysen, I. Gordon, and J. Poortmans. *Epitaxy-free monocrystalline silicon thin film: first steps beyond proof-of-concept solar cells*. Progress in Photovoltaics: Research and Applications, 19(7):844–850, 2011.

[14] B. E. Hardin, H. J. Snaith, and M. D. McGehee. *The renaissance of dye-sensitized solar cells*. Nature Photonics, 6(3):162–169, 2012.

[15] Y. Liu, C.-C. Chen, Z. Hong, J. Gao, Y. M. Yang, H. Zhou, L. Dou, G. Li, and Y. Yang. *Solution-processed small-molecule solar cells: breaking the 10% power conversion efficiency*. Scientific Reports, 3, 2013.

[16] J. Dore, R. Evans, U. Schubert, B. D. Eggleston, D. Ong, K. Kim, J. Huang, O. Kunz, M. Keevers, R. Egan, S. Varlamov, and M. A. Green. *Thin-film polycrystalline silicon solar cells formed by diode laser crystallisation*. Progress in Photovoltaics: Research and Applications, 21(6):1377–1383, 2013.

4

Dual-interface gratings

4.1 Introduction

In chapter 3 section 3.5, we described how several types of thin-film solar cells can benefit from additional light trapping sophistication due to incomplete absorption. Among these are thin-film cells based on organics, a-Si and c-Si cells. To help improve these cells one can utilize various photonic phenomena, which increase the transit time and the intensity of light within the active material, and thus enhance absorption. In this respect, photonic nanostructures offer many key opportunities as they provide advanced control over the flow of light. Much research over the years has gone into developing and incorporating photonic structures in solar cells in order to have a complete absorption with as less material as possible to decrease the costs [1–5].

Though there are many photonic phenomena that can be used, each of them is typically only effective in a limited wavelength range. Thus, to reach a broadband strong absorption enhancement, exciting as many as possible is paramount. Various nanostructured materials have since been proposed to achieve this, both periodic and aperiodic [6–10]. These nanostructures provide significant absorption enhancements through various mechanisms such as scattering, diffraction and coupling into waveguide modes or plasmonic modes [7–9, 11–20]. The idea of using plasmonic resonances to enhance thin-film solar cells has especially raised a large interest because of the strong scattering and near-field confinement [7, 8, 21–25]. Though plasmonic modes are typically confined close to the metal interface, the

absorption can be tuned to primarily occur in the active layer [4, 14, 16, 21].

One of the main obstacles in broadband absorption enhancement is that there is no simple nanostructure that can allow optimal excitation of mulitple and various photonic phenomena throughout the whole wavelength range of interest. In order to overcome this, much effort has been put in combining different nanostructures in one solar cell device. A significant research interest was raised for solar cell devices, which combine front and back gratings [12, 13, 20]. The two gratings can be engineered to complement each other by operating in non-overlapping wavelength ranges, resulting in an overall broad absorption enhancement. In some fabrication processes these dual-interface grating (DIG) systems may be introduced with no significant difficulty [20].

This chapter gives an in depth discussion on light trapping strategies with DIGs. We focus, in particular, on the use of triangular DIG structures of different materials. Numerical studies of the extensive mode-coupling possibilities of DIG structures are done. Expanding upon the previous works, we explored design principles of DIG structures which utilize more photonic phenomena to enhance absorption. To be more specific, we focus on utilizing multiple diffraction coupling orders to waveguide and plasmonic modes, dark and bright modes, and also antireflection through gradual effective index transition. We enhance the efficiency of multiple diffraction coupling processes by utilizing multiperiod DIG gratings, i.e. a different periodicity for the top and bottom grating. Multiperiodic DIG structures form supercells with rich Fourier spectra which we demonstrate to enhance various diffraction couplings to multiple waveguide and surface plasmon polariton (SPP) modes simultaneously, over a large wavelength range. We further present an analysis of the effects of symmetry-breaking via blazing, which provide access to dark modes, further broadening the enhancement range. We were the first to demonstrate how weak blazing may lead to unprecedented highly efficient excitation of modes that are inaccessible with symmetric structures without sacrificing the coupling efficiency to symmetric modes and absorption at other incidence angles. By combining all the possibilities shown here, the design strategy that we propose can lead to a stronger and a more broadband absorption enhancement than previously reported.

The discussion in this work focuses on structures with semiconductor gratings on top combined with metal gratings on the back. However, the proposed principles can be adapted to other material combinations. We focus mainly on 1D gratings in a 2D structure to keep both the analysis and calculations more easily tractable for better understanding of the phenomena. In reality, these structures can be extended to be polarization independent via the more conventional 2D gratings.

The results shown here are for a-Si material, except for Figure 4.13 where we explore the possibility in utilizing the DIG structure for c-Si based cells. In practice, a-Si based solar cells utilize hydrogenated a-Si (a-Si:H) which has a better

carrier diffusion length but different absorption characteristics and refractive index. Note however that the main purpose of this chapter is to introduce the DIG light trapping strategy that is not specific for a certain active material.

Section 4.2 introduces the employed grating systems and the initial design principles. Section 4.3 discusses the starting, symmetric single-periodic DIG structures, which can already provide significant enhancement. Section 4.4 extends the device to multiperiodic structures and explains the operating principles. Section 4.5 further tailors the performance by adding blazed, asymmetric features. The main results are summarized in section 4.6.

Most of the work in this chapter was presented in our paper in Ref. [26]. The work presented here was done in collaboration between the Metamaterials and Plasmonic Research Laboratory at the University of Texas at Austin, the Micro- and Nanophotonic Materials Group at the University of Mons, and the Solar Cells Group at Ghent University.

4.2 Design strategy

Figure 4.1a shows an example of dual interface triangular gratings in the case of a-Si thin-film solar cells. The indium tin oxide (ITO) top triangle grating structure is intended to give good antireflection properties at the front surface through the gradually varying effective index. This gradual approach with subwavelength

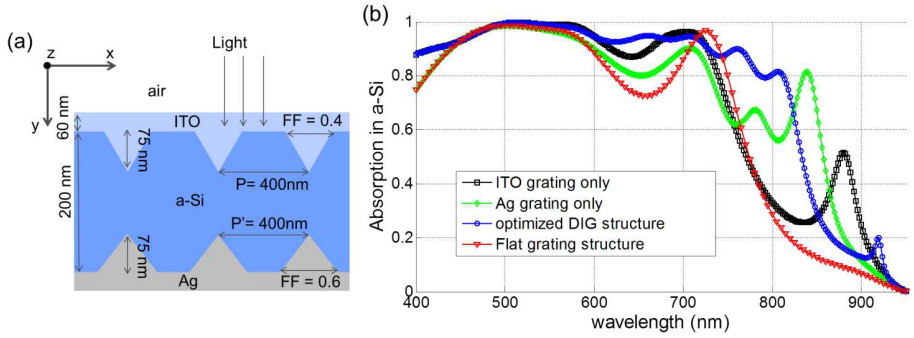

Figure 4.1: (a) Model of the simulated a-Si grating system. (b) Normal incidence absorption spectrum for flat structure (red triangles), ITO front grating only (black squares), Ag back grating only (green diamonds), and DIG structure (blue circles).

features is useful as an effective antireflection coating with broadband transmission [2, 27–29]. For the metal back grating we also use a triangular geometry that we previously demonstrated to have a flexible scattering capability and beneficial field distribution of SPP modes [14]. Basic design guidelines for the dimensions of the grating structures to control the waveguide and SPP mode resonances are

obtained by folded dispersion diagrams [14]. The fact that the triangular grating geometry also changes the effective layer thicknesses should be taken into account, as it affects the modal dispersion relations.

As we mainly aim to present the main principles, we focus on 1D grating structures: full wave 2D simulations and eigenmode analyses have been performed using finite element techniques with COMSOL multiphysics. One can very often derive 3D structures that respond to arbitrary light polarization in a similar way as the 2D case with TM polarization, if plasmonic effects are exploited correctly. For this reason, we mainly consider Transverse Magnetic (TM) polarization, in which the magnetic field has one component in the z direction (Figure 4.1a). Refractive index data is taken from databases for silver [30] and for a-Si [31]. To calculate the overall absorption efficiency, we integrate the divergence of the Poynting vector in the active layer and normalize it to the incoming power. We assume perfect internal quantum efficiency throughout the active layer, therefore absorption everywhere in the active layer is equally important.

4.3 Symmetric dual interface gratings

In this section, we examine symmetric DIGs with optimized triangle heights and grating fill factors (FF) to enhance absorption, see Figure 4.1a. The FF here is a ratio between the lateral size of the grating feature (the triangle) to the grating period. Figure 4.1b shows the absorption spectra in the a-Si active layer for increasingly complex geometries: flat structure, front and back grating structure only and for a DIG structure.

Enhancement with the front ITO grating only (Figure 4.1b, black square curve) occurs at shorter wavelengths ($<$ 720 nm) and via a resonance peak due to (dielectric) waveguide mode excitation around 880 nm. A profile plot of the absorption and power flow at 660 nm (Figure 4.2a) reveals that the main mechanism for the enhancement at shorter wavelengths is due to scattering by the ITO triangle features. The ITO triangles focus the incoming light, and subsequently spread it inside the active layer (Figure 4.2a). For the structure with Ag back contact only (Figure 4.1b, green diamond curve) the main enhancement occurs at longer wavelengths ($>$ 750 nm), due to the excitation of a leaky waveguide mode at 780 nm and a plasmonic mode at 838 nm. The wavelength region $<$ 750 nm is affected minimally by the metal grating structure. When we combine both grating structures, we obtain a complementary enhancement (Figure 4.1b, blue circle curve). The scattering power of the front ITO grating structure at shorter wavelengths is still present, as incoming light focusing and spreading into the a-Si layer occurs (Figure 4.2b). Additionally, see Figure 4.1b blue circle curve, a combination of a dielectric waveguide mode and a Fabry-Perot resonance arises at 660 nm, weakly excited together with a plasmonic near field enhancement near the metal tip (Fig-

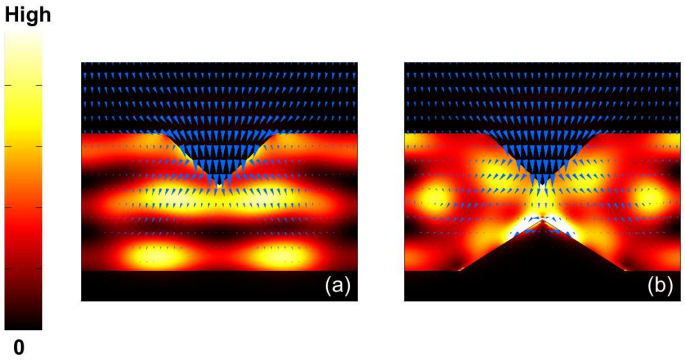

Figure 4.2: The Poynting vector (cones) and its divergence (absorption profile) at 660 nm wavelength in the case of (a) ITO grating system only, and (b) DIG system.

ure 4.2b), which together help boost the overall absorption. The magnetic field profile plots for the DIG case (Figure 4.3) reveal that the absorption peak at 760 nm is mainly a leaky waveguide mode (strong field inside the a-Si layer), whereas the peak at 810 nm corresponds to a plasmonic mode (strong field at the metal-silicon interface).

Wavelength shifts of the waveguide and SPP modes are observed when the grating structures are combined. This is partly due to changes in the effective thickness and effective index by introducing the metallic and ITO gratings. However, aside from these factors, different modes that overlap in a certain spatial and spectral region can interfere with each other and form hybrid modes. This interaction can lead to observed resonance wavelength shifts. The properties of these hybrid modes will also be a mix of the properties of the interacting bare resonances and depends on the wavelength detuning between each other.

In this chapter we are mainly concerned with having as much as possible photonic modes that can boost absorption in the wavelength region of interest. The exact characteristics of the photonic modes are of little concern as long as they boost absorption in the active material of the cell. Typically, a significant mixing of characteristics occurs when one of the interacting bare resonances has a broad linewidth. Thus, leaky guided modes with limited linewidth seldom affect each other strongly and one can still identify a unique dominant component of the resonance. For this reason, the nomenclature to describe the leaky guided modes here are kept as if we are dealing with bare resonances though they are indeed hybrid in nature. However, in chapter 6 of the book, we will discuss a useful class of hybrid modes arising from the mixing of an LSPR and other photonic resonances in more detail. There we investigate the extinction, photoluminescence, and field profile characteristics of such hybrid plasmonic modes and how we can tune them

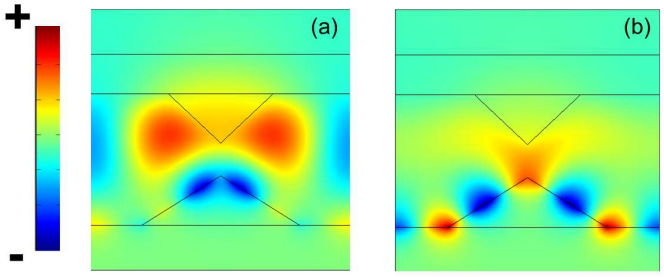

Figure 4.3: Magnetic field (H_z) profiles (snapshot in time) for the DIG structure at wavelength of (a) 760 nm and (b) 810 nm.

through geometry and through an active control of their surrounding material.

In the end, the combined grating structure leads to a better overall enhancement. We calculate an integrated absorption (TM polarization) of the AM1.5G spectrum in the 400-950 nm wavelength region of 83.10% for the DIG structure and 71.96% for the flat structure.

4.4 Dual periodic dual-interface gratings

For solar cell purposes it is desirable that the incoming broadband sunlight radiation couples to as many as possible (dielectric) waveguide and SPP modes in the solar cell. This coupling of incoming light to leaky guided modes via gratings depends on momentum conservation, eigenfield profiles of these modes, and the scattering properties of the gratings [32]. The propagation vector (k-vector) requirement is fulfilled by selecting the proper periodicity regardless of the grating geometry [32, 33]. However, the other two factors strongly influence the coupling efficiency as discussed before. In symmetric grating systems, there will be modes with dark and bright radiation coupling properties as discussed in chapter 2. Even for bright waveguide and SPP modes, coupling efficiency may be low due to a mismatch between scattered and modal field profiles. In general, there is a trend that lower diffraction orders have a better coupling efficiency than higher order ones [34]. Even though access to more modes is possible with larger periodicity, the scattering properties of a standard grating system do not commonly support efficient higher-order diffraction coupling.

This higher order diffraction to guided modes problem (with larger in plane momentum in the periodicity direction k_x) can be alleviated by having stronger small-periodicity components in the grating system. These additional components give more accommodating scattering properties to match the amplitude oscilla-

tions of higher order diffraction guided modes. Instead of just superimposing different periodicity components on one surface, we propose to spread the different Fourier components by having different periodicities on both interfaces, ensuring more flexibility in the design. This structure tackles the problem of providing efficient higher order diffraction coupling to multiple waveguide and SPP modes by effectively lowering the diffraction order while keeping the fundamental order accessible, as will be shown below.

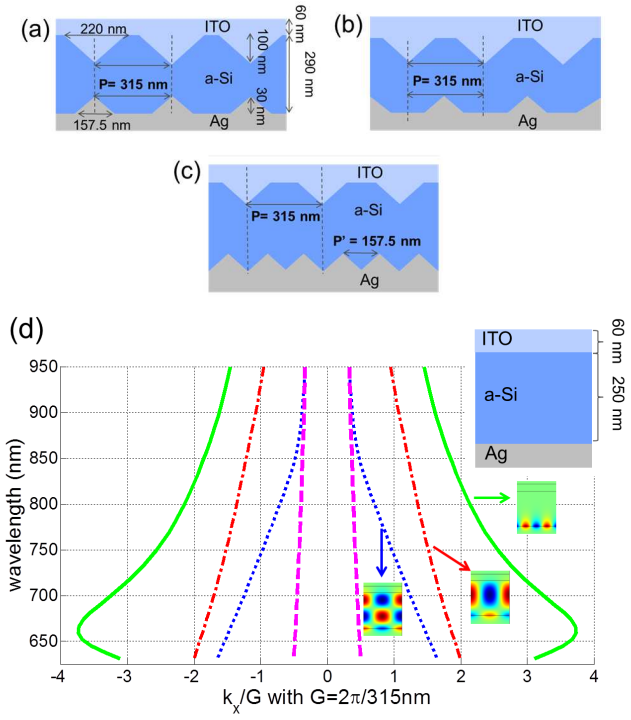

Figure 4.4: Compared grating structures with period $P = 315$ nm, (a) in phase gratings, (b) π phase shifted gratings, and (c) dual periodic DIG system with the same macro periodicity ($P = 315$ nm) and smaller sub-periodicity ($P = 157.5$ nm). (d) Dispersion diagram of waveguide and SPP modes in the indicated flat solar cell structure. Green line for SPP mode, red line first-order waveguide mode, blue line second-order waveguide mode, and the pink line indicates the light line in air.

Multiperiodic DIG structures in which the back metal grating has a smaller period than the top ITO grating are especially considered here (Figure 4.4c) for several reasons. First, the plasmonic back grating has a higher scattering cross-section as compared to the front ITO grating, and thus affects the scattering properties more. Second, plasmonic modes are localized to the surface of the metal and thus these modes are not sensitive to the top grating. Therefore, in order to improve

diffraction coupling to plasmonic modes, which have a larger momentum, it is necessary to have a smaller periodicity on the back surface. The larger periodicity at the top grating is more suited for dielectric modes, as they are more influenced by that top grating, and they have a smaller k_x. We focus on dual periodic DIG systems in which the back grating periodicity is half of the macro periodicity of the whole structure. With this configuration we aim to increase diffraction for second-order processes (according to the macro periodicity) while maintaining the efficiency for first order processes.

Solar cell structures with the same macro periodicity ($P = 315$ nm) are compared in Figure 4.4. Here, P is chosen in order to have as many first order diffraction coupling to dielectric waveguide modes as possible, while having higher order diffraction coupling to SPP modes in the 700-950 nm wavelength region. The accessible waveguide and SPP modes will still be largely determined by the macro periodicity. Via the dispersion relation of the planar structure (Figure 4.4d and inset) we can design the gratings to accommodate coupling to the chosen modes at the desired wavelengths. The k_x axis in Figure 4.4d is normalized with respect to $G = 2\pi/P$. The effective thickness of the a-Si layer in the cells in Figure 4.4a-c is similar to the planar reference thickness.

These structures (Figure 4.4a-c) support one SPP and two waveguide bright modes in the wavelength region above 625 nm (Figure 4.4d). The peculiar bending of the SPP dispersion is due to the refractive index of a-Si. The crossing points of the dispersion curves with the vertical lines (at integers) indicate the conditions for which the modes can be excited by normal incident light, when we introduce a grating structure with periodicity $P = 315$ nm. The integer value at these crossings indicates the diffraction order. For $P = 315$ nm, normal incident light can access the first-order waveguide mode around 930 nm, the second-order waveguide mode around 750 nm, and the SPP mode around 825 nm. Note that the diffraction coupling to the SPP is second order, but for the waveguide modes it is first-order.

The absorption spectra for normal incidence are shown in Figure 4.5a. The dual periodic DIG system (green line in Figure 4.5a) is able to excite more resonances in a more efficient manner as compared to the single period systems (blue dash-dotted and red dotted lines in Figure 4.5a). The nature of the excited modes can be identified from their magnetic field profiles for the dual periodicity system (Figure 4.5b). The resonance at the wavelength of 734 nm pertains to a second-order waveguide mode. At 800 nm and 876 nm, we see a mixed profile arising from the interferences of plasmonic and dielectric modes (they are relatively close and broadband in wavelength). Besides the waveguide and SPP modes, we also expect a Fabry-Perot resonance around this wavelength range, as can be seen from the flat structure absorption spectrum. Eigenmode calculations (not shown) for structures with gradually decreasing triangle height reveal that the peaks at 800 nm and 876 nm stem from a SPP mode and a Fabry-Perot mode. The profile at

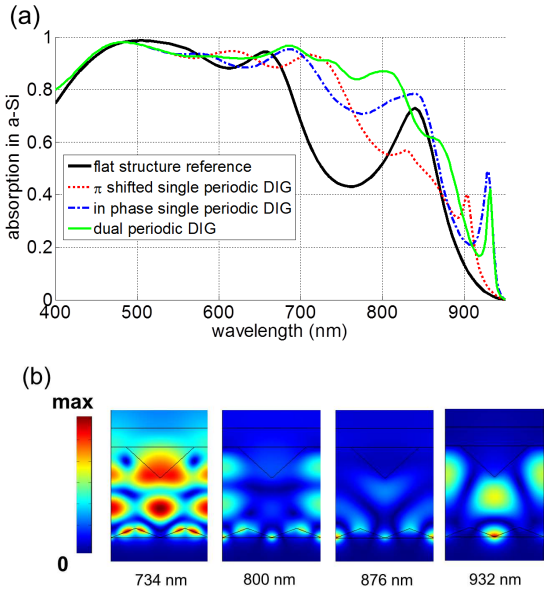

Figure 4.5: (a) Absorption spectra of DIG systems in Figure 4.4a-c. (b) $|H_z|$ field profiles at the resonances for the dual-periodic structure.

932 nm is distinctively a first-order waveguide mode. Thus after accounting for all the resonances, we see that not only have we boosted second-order diffraction coupling to the SPP mode, but we also maintained strong first-order diffraction coupling to both dielectric modes.

This dual interface multiperiodicity is especially promising when working with a larger macro period, as this leads to more higher order diffractions in the wavelength range of interest. To show this we compare single and dual periodic symmetric systems with a larger macro periodicity of 525 nm (Figure 4.6a). In Figure 4.6b we see that the single periodicity structures can still provide good coupling efficiency for some of the resonances. However, the dual periodicity gives an overall better coupling efficiency and access to more resonances. The field profiles for the resonances at longer wavelengths in Figure 4.7 indicate that most of the excited modes arise from higher order diffraction coupling. The multiple amplitude oscillations in the horizontal direction for the resonances at 792, 826 and 896 nm indicate that they are excited with higher order diffraction processes.

In summary, we have shown that dual periodic systems can provide better coupling efficiency to multiple waveguide and SPP modes, as compared to single periodic systems. By using double periodicity, coupling efficiency to higher order modes can be achieved without sacrificing coupling to lower-order modes, which can increase the overall absorption efficiency of the device.

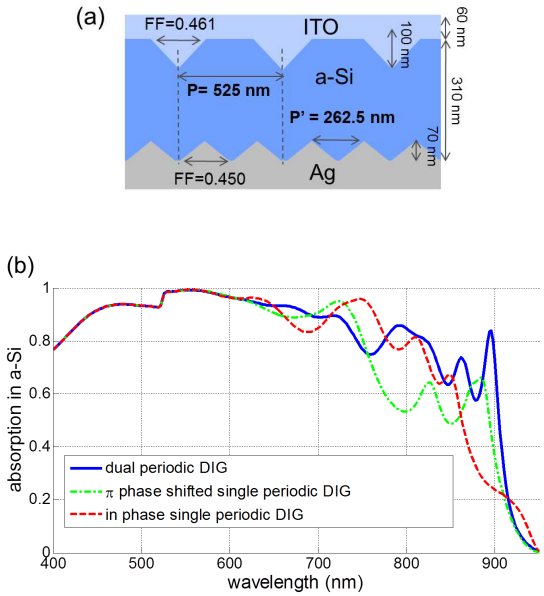

Figure 4.6: Comparing single and dual periodicity for larger periods. (a) Schematics of the symmetric dual periodic DIG system with macro periodicity $P = 525$ nm and smaller periodicity of $P = 262.5$ nm. (b) Absorption spectra comparison like that in Figure 4.5 for the dual periodic DIG system in (a) and symmetric single periodic DIG systems with 525 nm periodicity that has the same triangle geometries.

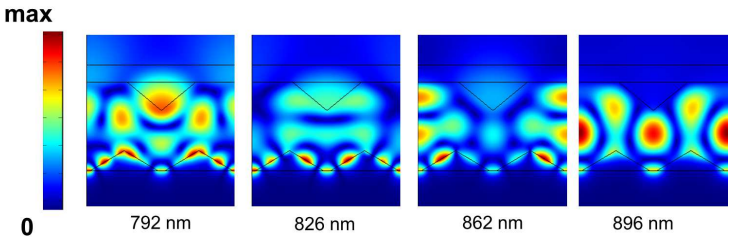

Figure 4.7: $|H_z|$ total field profiles at the resonances above 750 nm for the dual periodicity structure in Figure 4.6a.

To achieve solar cells with such multiperiod DIG structure, one can consider utilizing superstrate fabrication techniques. In superstrate cells, the solar cell structures are grown first on top of a transparent substrate [35]. We can first pattern this substrate before depositing the solar cell materials on it. After deposition, we will have the top side available for additional patterning before applying the contacts.

4.5 Blazed dual-interface grating systems

In symmetric grating systems, there are also dark antisymmetric waveguide and SPP modes, which cannot be accessed by normal incident plane waves. By breaking the symmetry, however, one can restrain guided modes from having perfectly antisymmetric field profiles and thus allow more modes for normal incident plane waves to couple to. Asymmetrical grating structures have been shown to potentially give more absorption due to this effect [19, 35]. This section demonstrates how weakly blazing dual triangle grating structures (introducing a weak asymmetry) results in an unprecedented strong coupling to previously inaccessible dark modes. By weakly blazing, we mean that the triangle features maintain a near isoceles shape.

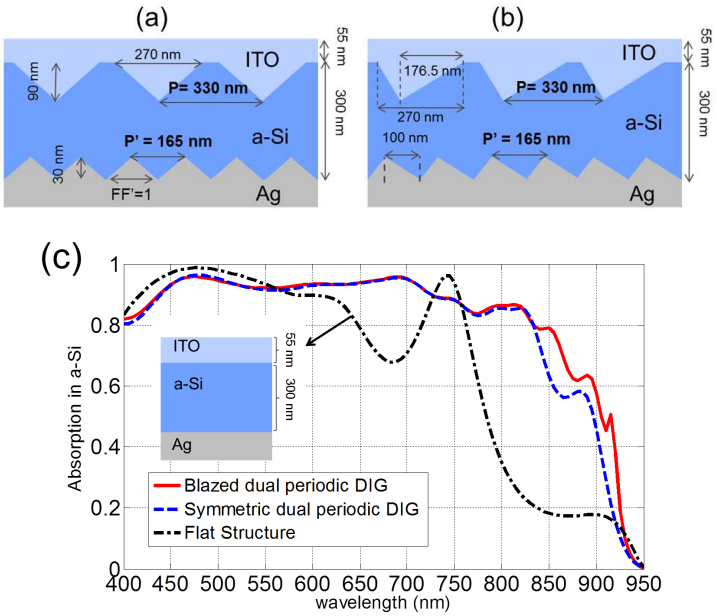

Figure 4.8: Structure schematic for (a) a symmetric DIG system and (b) when blazing is applied. (c) Absorption spectrum of the structures for normal incidence, compared with a planar reference.

We compare the absorption spectrum of a symmetric DIG system (Figure 4.8a) and its weakly blazed counterpart (Figure 4.8b) in Figure 4.8c. The blazing is applied to both the front and back grating. The absorption spectra show that weak blazing is sufficient to strongly excite previously dark modes, as new pronounced peaks appear. The weak blazing changes both the scattering properties of the grating structure and the eigenmode field profile of dark modes. Interestingly, we see

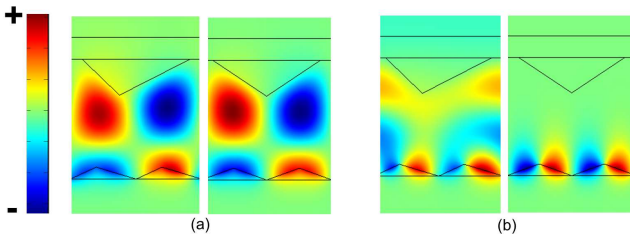

Figure 4.9: Dark modes H_z profile in the symmetric DIG system and their accessible form in the blazed DIG system. (a) First order waveguide mode in the two systems: blazed (left) and symmetric (right) at 915 nm wavelength. (b) SPP mode: blazed (left) and symmetric (right) at 850 nm.

that absorption at other wavelengths is preserved with weak blazing, particularly at the peaks already present for the symmetric structure. Dark modes are thus more sensitive to the blazing than bright modes. This implies that one can first optimize the symmetric grating to couple bright modes, e.g. with the period doubling enhancements of the previous section, and then introduce blazing for further optimization.

We look into the details behind the additional resonances in the blazed system by examining and comparing their eigenmode field profiles in the symmetric and blazed case (Figure 4.9). The two new peaks at 850 nm and 915 nm correspond to a SPP and a dielectric mode, respectively. We can see (Figure 4.9a) that there is only a weak distortion of the field profile due to the blazing for the waveguide mode, as compared to the SPP mode in Figure 4.9b. However, this minimum distortion in the eigenmode field profile (Figure 4.9a left compared to right) is already enough to give a strong excitation because the change in the scattering properties of the gratings complement as mentioned before. The heavier distortion of the SPP dark mode (Figure 4.9b left compared to right) is partially due to the fact that this mode is close to relatively broadband bright resonances, giving stronger interferences and a mixed modal profile. Although the SPP dark mode is uncoupled to other resonances in the symmetric grating system, other bright modes can interfere with this previously dark SPP mode in the blazed system, since now this mode is also accessible for normal incident light.

Blazing both front and bottom gratings is important in achieving the desired result. Figure 4.10 shows the effect of blazing only one side of the DIG structure on the absorption spectrum as compared to blazing both. We show here the total absorption spectrum (including metal absorption) to give a more direct idea of the coupling efficiency. The resonances that correspond to excitation of previously dark modes lead to above 90% total absorption, indicating that the coupling of incoming light to these modes is very strong when a weak blazing is applied. The

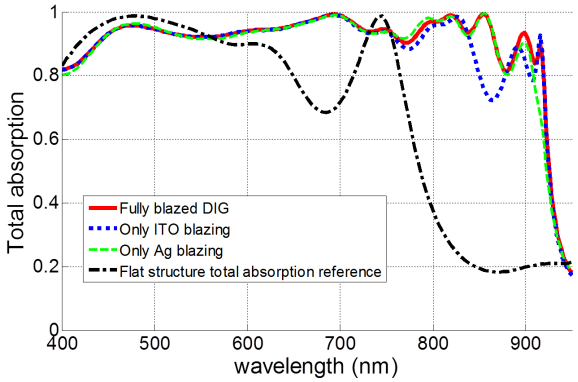

Figure 4.10: Total absorption spectra of a fully blazed DIG structure from Figure 4.8b (solid red line) and of structures that have blazing on the ITO front grating only (dotted blue line) and on the Ag back grating only (dashed green line). For comparison, we show also the total absorption spectrum of a reference flat structure as in Figure 4.8c (dash-dot black curve).)

dark waveguide mode resonance at 915 nm will not be excited if we only blaze the back grating, and the dark SPP mode resonance at 850 nm is not excited if we only blaze the ITO side. This again shows the power and flexibility of combining both front and back gratings. Tailoring of the scattering and eigenmode field profile to access dark modes can be accomplished with more degrees of freedom in a DIG structure.

To demonstrate that high coupling efficiency to multiple guided modes is possible in blazed dual periodic DIG systems, we show an optimized system in Figure 4.11 and compare with its non-blazed counterpart. In the blazed system (Figure 4.11b) we apply different blazing directions for the top and bottom gratings. In addition, we shift the front grating slightly with respect to the lower grating, also leading to a more optimized absorption. The red dashed circle line in Figure 4.11c shows nearly 100% total absorption at guided mode resonances at longer wavelengths (> 700 nm). Thus, the blazed dual-periodic DIG structure can indeed support a strong coupling efficiency with more modes, leading to an integrated absorption efficiency in the a-Si layer for normal incidence of 87.36% for TM polarization. The flat structure reference (ITO 60 nm/a-Si 290 nm/Ag) in Figure 4.11c gives a normal incidence integrated absorption efficiency of 73.97%. Though we focus on optimizing the conditions for TM polarized light, we can see in Figure 4.11c (magenta dots) that there is also improvement of TE polarized light absorption, although in some wavelength ranges the absorption decreases. The integrated absorption efficiency for normal incident TE polarized light is 81.53%. For extra reference, we plot the absorption in the Ag back contact of the blazed

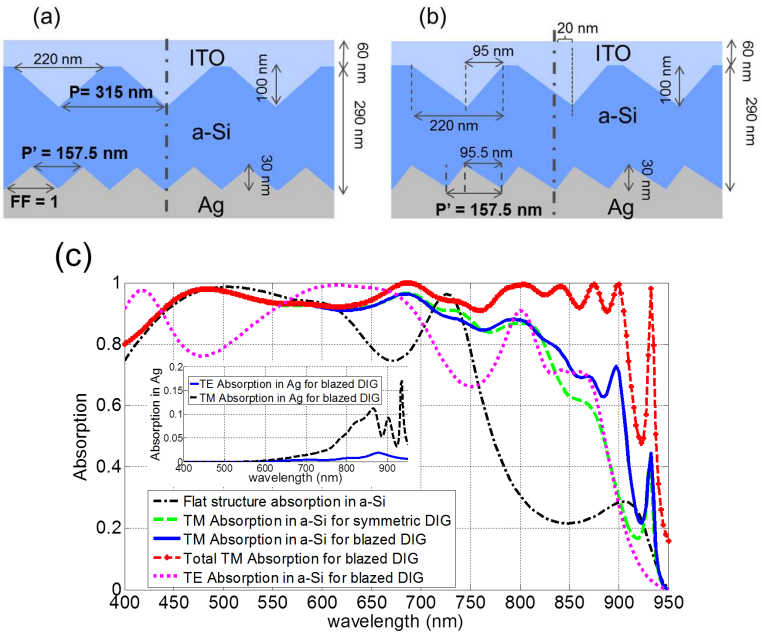

Figure 4.11: (a) Symmetric dual periodic DIG system. (b) Optimized blazed dual periodic DIG system providing high coupling efficiency to multiple guided modes. (c) Absorption spectra of the structures along with a planar reference (ITO 60 nm/a-Si 290 nm/Ag). Inset of (c) shows the absorption in the Ag back contact for (b).

DIG structure (Figure 4.11b) for both polarizations in the inset of Figure 4.11c. We see in the inset that there is a small absorption in the Ag back contact, and we note that a significant part of the absorption can happen in the ITO layer at wavelengths > 900 nm.

Figure 4.12 shows the integrated absorption efficiency (Abs_{int}) (normalized to incoming power at normal incidence) as a function of incidence angle for the optimized DIG structures and the planar reference of Figure 4.11c. We see that the absorption of the blazed structure in Figure 4.11b for both TE (black dashed) and TM (blue solid line) cases surpasses the flat reference absorption (green dash-dotted for TE and purple squares for TM) until 40° angle of incidence. Beyond 40°, the TM case absorption in the blazed structure is still above the flat reference case although the TE case absorption in the blazed structure is less than the flat layer TM case absorption. Comparing Abs_{int} for optimized symmetric (red dots) and blazed (blue solid) DIG structure, we see that the blazed structure improves the near normal incidence absorption performance without much affecting the absorption performance at larger angles. Also, because of the weak blazing, only a very weak dependence on the orientation of incidence angle ($+\theta$ or $-\theta$) for the blazed

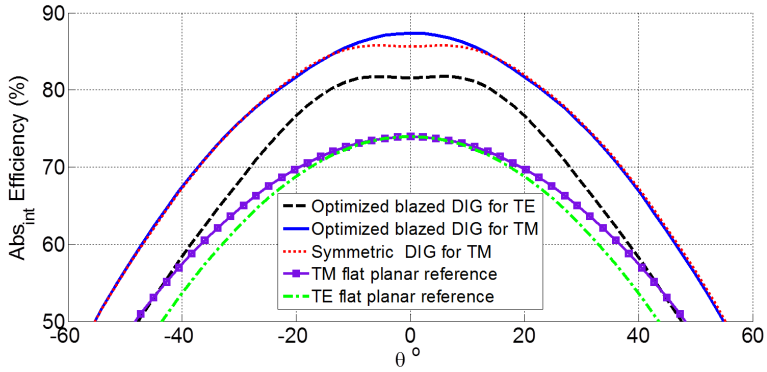

Figure 4.12: Integrated absorption efficiency versus incidence angle for the structures in Figure 4.11(a) and (b) and a flat planar reference (ITO 60 nm/a-Si 290 nm/Ag).

DIG structure is distinguished. Around normal incidence ($\pm 13.5^{\circ}$), the difference between the two orientations of θ is only in the range of 0.1% while at large angles it can reach up to 0.5%, which is still quite weak. Though the difference of Abs_{int} between the symmetric and blazed case here is only 1.7% for normal incidence, the results show that weak blazing can allow coupling to more modes at normal incidence without ruining the angular performance at larger angles.

A more distinct advantage of weakly blazed dual-periodic DIG structures over their symmetric counterparts is observed when the wavelength range window for absorption enhancement is larger. In such case there is room for more guided modes to come into play. One can see this for a thin c-Si film shown in Figure 4.13. Figure 4.13a shows a comparison between a symmetric and a blazed DIG structure applied to a 1 μm thick c-Si solar cell. Note that c-Si based cells would typically have a larger thickness in practice but the 1 μm thickness is chosen to demonstrate the DIG light trapping strategy performance. In this example the bottom grating periodicity is chosen to be larger than that of the top grating to focus on waveguide modes instead of SPP modes. The usage of SPP modes is less favorable due to the extremely weak absorption capability of c-Si at the longer wavelength range causing the absorption to occur mainly in the metal. As can be seen in Figure 4.13b the weakly blazed DIG structure outperforms its symmetric counterpart in a broader angle of incidence range than in the case of Figure 4.12. The weakly blazed structure has a better absorption over a broad angle of incidence range from -60° to 60°. The results of Figure 4.13b and Figure 4.12 show that breaking the structural symmetry may improve absorption in the whole angle of incidence range of interest.

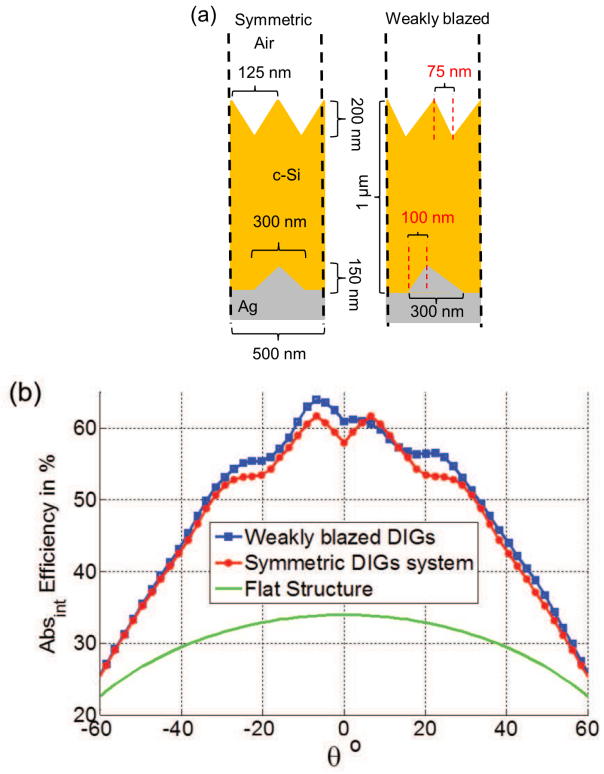

Figure 4.13: (a) Symmetric and weakly blazed DIG structure for a c-Si thin-film cell. (b) Integrated absorption efficiency comparison for TM polarized light of the structures in (a) along with their unpatterned counterpart.

4.6 Summary

This chapter discusses light trapping strategies utilizing DIG structures for absorption enhancement in thin-film solar cells. Multiperiodic DIG structures are demonstrated to enhance the coupling efficiency to more photonic phenomena as compared to single periodic structures. These structures can be tailored to give stronger coupling to higher order guided modes, without sacrificing the coupling efficiency to lower order modes. Applying weak blazing to triangle grating structures allows radiation coupling to previously dark modes with unprecedented high efficiency at normal incidence, without sacrificing the coupling at other wavelengths and at larger angles. Blazing of the front and back grating provides specific access to guided modes, e.g. blazing at the front dominantly influences the dielectric waveguide modes and not the SPP mode at the back contact. Combining blazing and dual periodicity in DIG structures leads to more accessible modes with strong coupling

efficiency and hence achieves a broader absorption enhancement. Weakly blazed DIG structures can outperform their symmetric counterparts throughout a broad angle of incidence range.

The light trapping strategy discussed here focuses mainly on the usage of leaky guided modes. This strategy would be more beneficial for solar cells with thickness significantly less than the optical path length gain provided by the leaky guided modes. Furthermore, the leaky guided mode resonances should ideally have significant linewidths, which is the case when the active material is a fairly strong absorber. It is thus most suited for thin-film solar cells with target thickness smaller or comparable to the wavelengths of interest. This is typically the case for organic and a-Si based solar cells whose thickness is limited due to carrier diffusion length limitations.

References

[1] D. N. Weiss, H. C. Yuan, B. G. Lee, H. M. Branz, S. T. Meyers, A. Grenville, and D. A. Keszler. *Nanoimprinting for diffractive light trapping in solar cells*. Journal of Vacuum Science & Technology B, 28(6):C6M98–C6M103, 2010.

[2] B. Paivanranta, P. K. Sahoo, E. Tocce, V. Auzelyte, Y. Ekinci, H. H. Solak, C.-C. Liu, K. O. Stuen, P. F. Nealey, and C. David. *Nanofabrication of Broad-Band Antireflective Surfaces Using Self-Assembly of Block Copolymers*. ACS Nano, 5(3):1860–1864, 2011.

[3] R. Tena-Zaera, M. A. Ryan, A. Katty, G. Hodes, S. Bastide, and C. Levy-Clement. *Fabrication and characterization of ZnO nanowires/CdSe/CuSCN eta-solar cell*. Comptes Rendus Cimie, 9(5-6):717–729, 2006.

[4] V. E. Ferry, L. A. Sweatlock, D. Pacifici, and H. A. Atwater. *Plasmonic Nanostructure Design for Efficient Light Coupling into Solar Cells*. Nano Letters, 8(12):4391–4397, 2008.

[5] F. J. Beck, S. Mokkapati, and K. R. Catchpole. *Plasmonic light-trapping for Si solar cells using self-assembled, Ag nanoparticles*. Progress in photovoltaics, 18(7):500–504, 2010.

[6] S. Fahr, T. Kirchartz, C. Rockstuhl, and F. Lederer. *Approaching the Lambertian limit in randomly textured thin-film solar cells*. Optics Express, 19(S4):A865–A874, 2011.

[7] O. Isabella, M. Zeman, J. Krč, and M. Topič. *Advanced light trapping techniques for thin-film silicon solar cells*. In 25th European Photovoltaic Solar Energy Conference, pages 3273–3279. WIP, 2010.

[8] S. Mokkapati, a. F. J. Beck, A. Polman, and K. R. Catchpole. *Designing periodic arrays of metal nanoparticles for light-trapping applications in solar cells*. Applied Physics Letters, 95:053115, 2009.

[9] W. E. I. Sha, W. C. H. Choy, and W. C. Chew. *A comprehensive study for the plasmonic thin-film solar cell with periodic structure*. Optics Express, 18(6):5993–6007, 2010.

[10] I. Gordon, L. Carnel, D. Van Gestel, G. Beaucarne, and J. Poortmans. *8on aluminum-induced crystallization and thermal CVD*. Progress in photovoltaics, 15(7):575–586, 2007.

[11] K. Q. Le, A. Abass, B. Maes, P. Bienstman, and A. Al. *Comparing plasmonic and dielectric gratings for absorption enhancement in thin-film organic solar cells*. Optics Express, 20(S1):A39–A50, 2012.

[12] H. Shen and B. Maes. *Combined plasmonic gratings in organic solar cells*. Optics Express, 19(S6):A1202–A1210, 2011.

[13] D. Madzharov, R. Dewan, and D. Knipp. *Influence of front and back grating on light trapping in microcrystalline thin-film silicon solar cells*. Optics Express, 19(S2):A95–A107, 2011.

[14] A. Abass, H. Shen, P. Bienstman, and B. Maes. *Angle insensitive enhancement of organic solar cells using metallic gratings*. Journal of Applied Physics, 109(2):023111–7, 2011.

[15] C. J. Min, J. Li, G. Veronis, J. Y. Lee, S. H. Fan, and P. Peumans. *Enhancement of optical absorption in thin-film organic solar cells through the excitation of plasmonic modes in metallic gratings*. Applied Physics Letters, 96(13), 2010.

[16] C. C. Chao, C. M. Wang, and J. Y. Chang. *Spatial distribution of absorption in plasmonic thin film solar cells*. Optics Express, 18(11):11763–11771, 2010.

[17] V. E. Ferry, M. A. Verschuuren, H. B. T. Li, E. Verhagen, R. J. Walters, R. E. I. Schropp, H. A. Atwater, and A. Polman. *Light trapping in ultrathin plasmonic solar cells*. Optics Express, 18(13):A237–A245, 2010.

[18] J. Gjessing, E. S. Marstein, and A. Sudb. *2D back-side diffraction grating for improved light trapping in thin silicon solar cells*. Optics Express, 18(6):5481–5495, 2010.

[19] Z. Yu, A. Raman, and S. Fan. *Fundamental limit of light trapping in grating structures*. Optics Express, 18(S3):A366–A380, 2010.

[20] V. E. Ferry, A. Polman, and H. A. Atwater. *Modeling Light Trapping in Nanostructured Solar Cells*. ACS Nano, 2011.

[21] H. A. Atwater and A. Polman. *Plasmonics for improved photovoltaic devices*. Nature Materials, 9(3):205–213, 2010.

[22] K. R. Catchpole and A. Polman. *Plasmonic solar cells*. Optics Express, 16(26):21793–21800, 2008.

[23] F. Hallermann, C. Rockstuhl, S. Fahr, G. Seifert, S. Wackerow, H. Graener, G. von Plessen, and F. Lederer. *On the use of localized plasmon polaritons*

in solar cells. Physica Status Solidi a-Applications and Materials Science, 205(12):2844–2861, 2008.

[24] C. Rockstuhl, S. Fahr, and F. Lederer. *Absorption enhancement in solar cells by localized plasmon polaritons*. Journal of Applied Physics, 104(12), 2008.

[25] H. H. Shen, P. Bienstman, and B. Maes. *Plasmonic absorption enhancement in organic solar cells with thin active layers*. Journal of Applied Physics, 106(7), 2009.

[26] A. Abass, K. Q. Le, A. Alù, M. Burgelman, and B. Maes. *Dual-interface gratings for broadband absorption enhancement in thin-film solar cells*. Physical Review B, 85:115449, 2012.

[27] E. B. Grann and M. G. Moharam. *Comparison between continuous and discrete subwavelength grating structures for antireflection surfaces*. J. Opt. Soc. Am. A, 13(5):988–992, 1996.

[28] E. B. Grann, M. G. Varga, and D. A. Pommet. *Optimal design for antireflective tapered two-dimensional subwavelength grating structures*. Journal of the optical society of America A, 12(2):333–339, 1995.

[29] M. K. Kim, D. K. Yi, and U. Paik. *Tunable, Flexible Antireflection Layer of ZnO Nanowires Embedded in PDMS*. Langmuir, 26(10):7552–7554, 2010.

[30] P. B. Johnson and R. W. Christy. *Optical Constants of the Noble Metals*. Physical Review B, 6(12):4370–4379, 1972.

[31] SOPRA-SA. *http://www.sopra-sa.com/*.

[32] A. Yariv and P. Yeh. *Photonics: Optical Electronics in Modern Communications*. Oxford University Press, Oxford, 6 edition, 2007.

[33] J. D. Joannopoulos, S. G. Johnson, J. N. Winn, and R. D. Mead. *Photonic Crystals: Molding the Flow of Light*. Princeton University Press, Princeton, 2nd edition, 2008.

[34] H. Zappe. *Fundamentals of Micro-Optics*. Cambridge University Press, 2010.

[35] X. Sheng, S. G. Johnson, J. Michel, and L. C. Kimerling. *Optimization-based design of surface textures for thin-film Si solar cells*. Optics Express, 19(S4):A841–A850, 2011.

5

One pass coherent calculations

5.1 Introduction

Current structures for solar cells or LEDs often incorporate optical elements in different size regimes, with a mixture of coherent and incoherent scattering components. These combined structures provide several computational challenges. On the one hand, the wavelength scale grating structures require one to take into account coherent effects. On the other hand, addressing structures in the ray optics regime such as rough diffusers with full wave simulation methods would typically require a huge computational domain. Furthermore, the total optical path length in such systems tends to be larger than the coherence length of light and thus fully coherent calculations cannot capture all of the real effects.

To address these complications we develop a simulation technique in this chapter which takes into account coherent effects where they matter the most while circumventing the need to fully implement the ray optics section of the structure. We avoid an extensive domain by working directly with the wavefront coming out of the ray optics section instead of its geometry. As any wavefront can be represented as a superposition of plane waves, we instead calculate the response of the wave section to different plane wave inputs. Phase relations are considered to be lost as soon as light enters or goes back to the ray optics section, hence the term one pass coherent (OPC) calculations. With our approach we can efficiently model 2D or 3D devices combining coherent and incoherent features, which is impossible with previously reported 1D methods [1–5]. A full wave simulation method that can

take into account partially coherent light by considering the Fourier components of the time signal has been described [6]. However, it still faces the same obstacles as other standard wave simulation techniques when used to simulate structures with ray optics segments such as a random diffuser.

Here, we additionally consider two topics that are studied using the OPC calculation method. First, we discuss the effect of limited coherence on solar cell absorption. With our calculation method we show that incoherence can lead to an increase of absorption on average in the presence of a diffracting element in the structure, if certain geometrical conditions are met. Second, we study the light trapping of structures with both rough diffusers and gratings, each at a different interface. More specifically, we examine combined structures with gratings at the front and rough diffusers at the back. Such structures are of great interest for solar cells with thicknesses exceeding a few wavelengths thick as will be discussed later. This is relevant and is illustrated for the case of thin-film poly-Si cells whose thickness is typically limited in the range of $1-10$ μm. The grating structures on the front provide flexibility in tailoring anti-reflection properties. Spinelli et al. have recently shown that nanopatterns on a Si substrate can suppress reflection to below 3% throughout the wavelength range of 450-900 nm [7]. The diffuser at the back will mainly serve to increase the optical path length.

In section 5.2 we describe the developed calculation method. In section 5.3 example calculations of the OPC method in which we simulate various diffusers and compare with measurement results. In section 5.4 we discuss the effect of coherence on solar cell absorption. In Section 5.5 we examine the combined back diffuser and front grating structures.

Most of the work in this chapter was presented in our paper in Ref. [8]. The work here is done in a collaboration between IMEC, the Micro- and Nanophotonic Materials Group at the University of Mons, the Light and Lighting Laboratory at the Catholic University College Ghent, and the Solar Cells Group at Ghent University.

5.2 Calculation method

As mentioned in the introduction, there is a dilemma in simulating structures with both ray and wave optics segments: Ray optics is not accurate enough, whereas full wave simulation of the whole structure is computationally costly. This problem is circumvented by directly considering the reflected wavefront coming out of the ray optics segment, instead of its geometry, which can be represented as a superposition of plane waves with a certain spatial frequency spectrum [9, 10]. Here, we mainly focus on structures with front gratings and rough diffusers at the back of the cell as shown in Figure 5.1a, though the method can be used for other combinations as well. We propose to model the ray optics segment in a structure

as a computational boundary which passes through incoming waves (towards -y) and relaunches plane waves with various directions (towards +y) into the structure (Figure 5.1b). The relaunched plane waves are determined in such a way that together they model the wavefront coming out of the ray optics segment of interest.

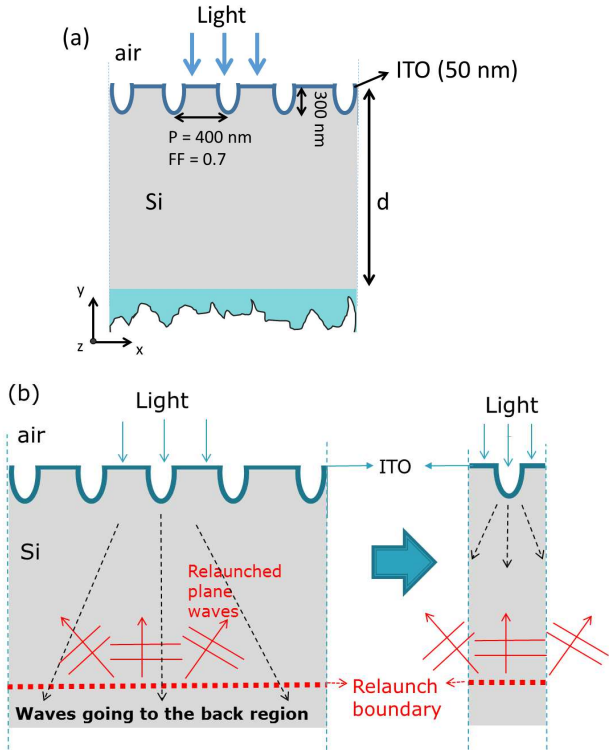

Figure 5.1: (a) The system under consideration. P is the grating period, FF is the grating fill factor and d is the thickness of the Si layer. The horizontal diameter of the grating feature is P×FF. The front part is coated with an indium tin oxide (ITO) layer of 50 nm thickness. (b) The proposed computational method which replaces the rough diffuser structure with a computational boundary and reduces the simulation domain to a single period of the grating.

The details of the computational steps are schematically shown in Figure 5.2. One first calculates the coherent field profile resulting from each relevant incident plane wave on the wave optics segment of interest in the structure. In our case here, the wave optics segment is the front grating (Figure 5.2a) and thus we calculate for one solar excitation direction from the front (air-side) as the first pass field profile (for each wavelength), and multiple (relaunched) directions from the back (Si-side). If we consider the incoming sunlight to be fully coherent or if the thickness of the cell structure is smaller than the coherence length, we would

have to calculate the coherent superposition of these calculated fields and know the phase relation between incoming and relaunched plane waves. However, if we can consider that coherence is broken after the bottom diffuser, the calculations of the total system response (absorption $A_{tot}(\lambda)$, reflectance $R_{tot}(\lambda)$ and transmittance $T_{tot}(\lambda)$) are simplified. Then we only need to consider interference effects for each launched plane wave separately and locally when it interacts with the front grating structure, and not between launched plane waves. By taking this assumption, the plane waves are treated as if they have their coherence length limited to the path length in one pass through the structure. Therefore, we refer to this method as one pass coherent (OPC) calculations.

The loss of coherence is applicable when the active material thickness itself is larger than the coherence length of light, or when the bottom diffusing structure is a bulk diffuser which makes light travel and scatter over a relatively long distance before coming back to the active material. In the case of sunlight, of which coherence length is around 1 μm [11], the loss of coherence assumption can be met relatively easily. One can therefore model any kind of bottom diffuser by calculating only one period of the front grating (Figure 5.1b). In essence, we trade complexity in real space for complexity in k-space. This method can treat any kind of structure at the bottom as long as the OPC assumption is valid and the reflected wavefront information is known.

Various one pass quantities necessary to calculate the total system response are obtained from the plane wave field profiles (Figure 5.2a). From the first pass field profile (incident sunlight) we determine the first pass absorption ($A_{first}(\lambda)$), reflectance ($R_{first}(\lambda)$), and transmittance ($T_{first}(\lambda)$), details below). Subsequently, from the field profiles of the relaunched plane waves the one pass relaunch absorption ($A_{k_{//}}(\lambda)$), escape transmittance ($R_{k_{//}}(\lambda)$) and relaunch reflectance ($T_{k_{//}}(k'_{//}, \lambda)$) are extracted for every possible transverse excitation propagation constant $k_{//} \leq k_{Si}$. Here $k_{Si} = kn_{Si}$ where k is the propagation constant in air and n_{Si} is the refractive index of silicon. The subscripts $k_{//}$ indicate the transverse direction (x- or z-axis in Figure 5.1a) of the plane wave excitation. The arguments $k'_{//}$ indicate the transverse plane wave component of the response in that particular direction. Note that $R_{first}(\lambda)$ and $R_{k_{//}}(\lambda)$ always indicate power escaping from the solar structure to air (towards +y). $T_{first}(k'_{//}, \lambda)$ and $T_{k_{//}}(k'_{//}, \lambda)$ always indicate power fractions going to the bottom of the cell (towards -y).

We provide now more details on how these quantities are determined. For clarity we describe the calculations only for 2D systems invariant along the z-axis and assume that the launched power for each plane wave is already normalized over one cell of the grating. The one pass absorption is calculated via the divergence of the Poynting vector over the absorbing volume (area in 2D):

$$A_q(\lambda) = \int (\nabla \cdot \mathbf{S}_q(\lambda)) dV \tag{5.2.1}$$

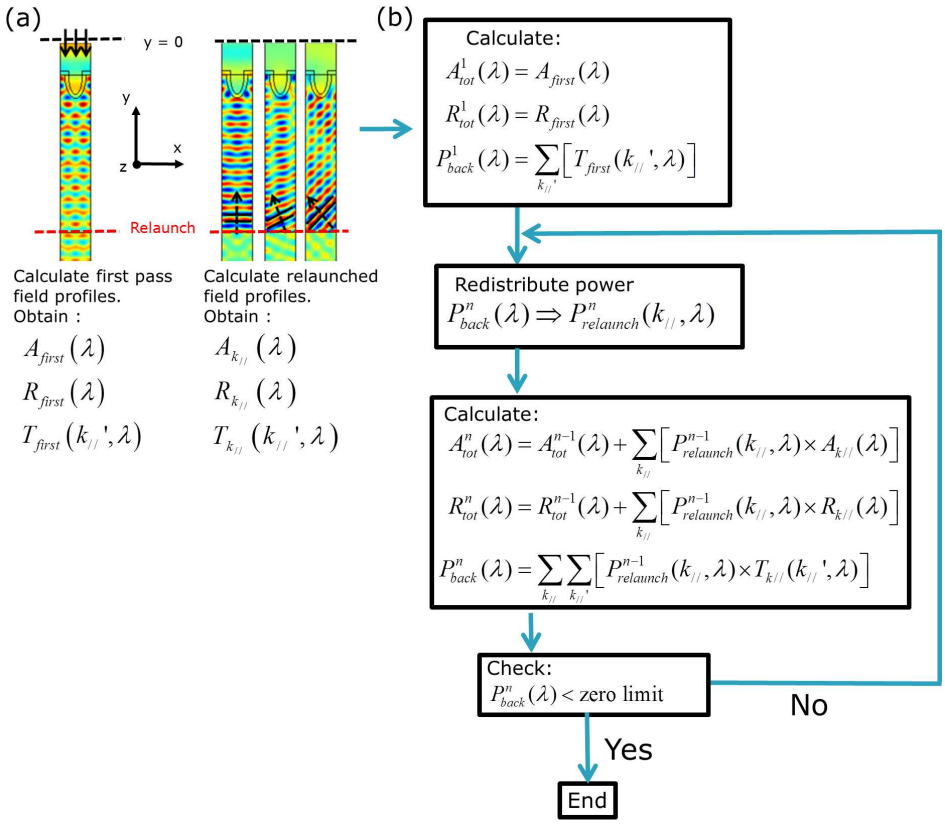

Figure 5.2: Computational scheme assuming a lossless back diffuser or reflector. (a) One pass field profile calculations. (b) OPC iteration.

where $\mathbf{S}_q(\lambda)$ is the Poynting vector defined as

$$\mathbf{S}_q(\lambda) = \frac{1}{2} Re\left[\mathbf{E}_q(\lambda) \times \mathbf{H}_q(\lambda)^*\right] \tag{5.2.2}$$

where $\mathbf{E}_q$ is the electric field and $\mathbf{H}_q$ is the magnetic field. The subscript q indicates whether it is the first pass case or a certain $k_{//}$ relaunch case. $R_{first}(\lambda)$ and $R_{k_{//}}(\lambda)$ to air are obtained via:

$$R_{first}(\lambda) = \int_P (\mathbf{S}^{scat}_{first}(\lambda) \cdot \mathbf{j}) dx|_{\text{y=0}} \tag{5.2.3}$$

$$R_{k_{//}}(\lambda) = \int_P (\mathbf{S}_{k_{//}}(\lambda) \cdot \mathbf{j}) dx|_{\text{y=0}} \tag{5.2.4}$$

calculated above the grating structure as shown in Figure 5.2a along one period P. $\mathbf{S}^{scat}_{first}$ refers to the scattered wave Poynting vector for the first launch case and **j** is the unit vector in the y direction. The scattered field can be obtained using the relation $\psi^{scat} = \psi - \psi^{incidence}$ where ψ is the total electric or magnetic field and $\psi^{incidence}$ is the incident plane wave from air propagating towards -y.

For our method it is necessary to decompose the scattered wave towards the bottom into a set of plane waves. One can use this information for example to consider specular reflection by relaunching plane waves with the same amplitude and $k_{//}$. We obtain these components via Fourier decomposition along the relaunch boundary:

$$\tilde{\psi}_{k'_{//}}(\lambda)|_{relaunch} = \frac{1}{P} \int_P \psi(x) e^{-ik'_{//}x} dx \tag{5.2.5}$$

where $\tilde{\psi}_{k'_{//}}$ is the amplitude of a Fourier component of the electric or magnetic field. With these Fourier components we calculate $T_{first}(k'_{//}, \lambda)$ and $T_{k_{//}}(k'_{//}, \lambda)$ which are the portions of the total power carried by each component to the bottom:

$$T_{first}(k'_{//}, \lambda) = \left[\int_P (-\mathbf{S}^{scat}_{first}(\lambda) \cdot \mathbf{j}) dx\right]_{relaunch} \tag{5.2.6}$$

$$T_{k_{//}}(k'_{//}, \lambda) = \left[\int_P (-\mathbf{S}^{scat}_{k_{//},k'_{//}}(\lambda) \cdot \mathbf{j}) dx\right]_{relaunch} \tag{5.2.7}$$

which are calculated along the relaunch boundary in one grating period with

$$\mathbf{S}^{scat}_{k_{//},k'_{//}}(\lambda) = \frac{1}{2} Re\left[\mathbf{E}^{scat}_{k_{//},k'_{//}}(\lambda) \times \mathbf{H}^{scat}_{k_{//},k'_{//}}(\lambda)^*\right] \tag{5.2.8}$$

where $\vec{\psi}^{scat}_{k_{//},k'_{//}}(\lambda)$ is the scattered $k'_{//}$ Fourier component for a $k_{//}$ plane wave excitation (here $\vec{\psi}$ represents **S**, **E** or **H**). Now we have enough information to start the subsequent OPC iteration procedure for the bottom structure (Figure 5.2b). Note that to model any kind of reflector at the bottom for a particular top grating

we only need to calculate the previous quantities once. With these values we proceed to take into account the reflector, which can have both diffuse and specular components. Here, it is assumed that the back reflector/diffuser is lossless and thus $T_{tot}(\lambda) = 0$. To obtain the total system response ($A_{tot}(\lambda)$ and $R_{tot}(\lambda)$), we start from the first response ($A_{first}(\lambda)$, $R_{first}(\lambda)$ and $T_{first}(k'_{//}, \lambda)$) and iteratively add the contributions of relaunched waves, until the power to be relaunched from the back side is close to zero (Figure 5.2b). Because there is no coherent interaction between different plane wave launches, the total response is calculated with:

$$A^n_{tot}(\lambda) = A^{n-1}_{tot}(\lambda) + \sum_{k_{//}} \left[P^{n-1}_{relaunch}(k_{//}, \lambda) A_{k_{//}}(\lambda)\right] \tag{5.2.9}$$

$$R^n_{tot}(\lambda) = R^{n-1}_{tot}(\lambda) + \sum_{k_{//}} \left[P^{n-1}_{relaunch}(k_{//}, \lambda) R_{k_{//}}(\lambda)\right] \tag{5.2.10}$$

where $P^n_{relaunch}(k_{//,}\lambda)$ is the relaunched power distribution (explained below). We can account for a lossy back reflector/diffuser without much added difficulty by relaunching the power that passes the relaunch boundary only partially. The values at the first iteration are determined from the first pass responses:

$$A^1_{tot}(\lambda) = A_{first}(\lambda) \tag{5.2.11}$$

$$R^1_{tot}(\lambda) = R_{first}(\lambda) \tag{5.2.12}$$

At every iteration the relaunched power distribution $P^{n-1}_{relaunch}(k_{//}, \lambda)$ (towards +y) consists of specular and diffuse components:

$$P^{n-1}_{relaunch}(k_{//}, \lambda) = \Phi^n_{Dif}(k_{//}, \lambda) + \Phi^n_{Spec}(k_{//}, \lambda) \tag{5.2.13}$$

where $\Phi^{n-1}_{Dif}(k_{//}, \lambda)$ and $\Phi^n_{Spec}(k_{//}, \lambda)$ are the spatial power density spectra of the diffused and specular component, respectively. $\Phi^n_{Spec}(k_{//}, \lambda)$ is updated at every iteration in order to account for the specular reflection properly with the relation:

$$\Phi^n_{Spec}(k_{//}, \lambda) = (1 - \alpha)\Theta^n(k_{//}, \lambda) \tag{5.2.14}$$

α is the portion of incoming power that will be diffused, which in general can depend on λ and $k_{//}$. $\Theta^n(k_{//}, \lambda)$ is the power contribution of plane waves with a certain $k_{//}$ value that are going to the bottom of the cell. $\Theta^n(k_{//}, \lambda)$ is calculated using:

$$\Theta^1(k_{//}\lambda) = T_{first}(k_{//}, \lambda) \tag{5.2.15}$$

in the first iteration and for the rest:

$$\Theta^n(k_{//}, \lambda) = \sum_{k'_{//}} \left[P^{n-1}_{relaunch}(k'_{//}\lambda) T_{k'_{//}}(k_{//}, \lambda)\right] \tag{5.2.16}$$

Note that $T_{first}(k_{//}, \lambda)$ and $T_{k'_{//}}(k_{//}, \lambda)$ give the complete information of how power is distributed to plane wave components propagating in the Si (towards -y). Thus, we can infer the values of $A_{tot}(\lambda)$ and $R_{tot}(\lambda)$ for any Si thickness of choice after simulating for a particular thickness, provided that the relaunch boundary is far enough from the top grating to avoid any possible near field effect. From that information we can calculate $P^n_{Dif}(\lambda)$

$$P^n_{Dif}(\lambda) = \sum_{k_{//}} \alpha \Theta^n(k_{//}, \lambda) \tag{5.2.17}$$

where $P^n_{Dif}(\lambda)$ is the total diffused power to be relaunched at iteration n which is then used to calculate $\Phi^n_{Dif}(k_{//}, \lambda)$ using:

$$\Phi^n_{Dif}(k_{//}, \lambda) = P^n_{Dif}(\lambda) F_{Dif}(k_{//}) \cos(\theta) \tag{5.2.18}$$

$F_{Dif}(k_{//})$ is the cross spectral density distribution of the wavefront coming out from the diffuser of our choice. One can infer $F_{Dif}(k_{//})$ from the far field radiant intensity distribution $J(\theta)$ coming out of the diffuser through the relation:

$$J(\theta) = C \times F_{Dif}(k_{//}) \cos^2(\theta) \tag{5.2.19}$$

where C is a proportionality constant and θ is the angle with respect to the normal direction of the diffuser surface (thus $k_{//} = k \sin(\theta)$). For a Lambertian source $F_{Dif}(k_{//}) = \frac{C_0}{\sqrt{k^2 - k^2_{//}}}$ where C_0 is a proportionality constant [9, 10]. Examples of various $F_{Dif}(k_{//})$ of diffusers along with their corresponding far field radiant intensity are shown in Figure 5.3. These different diffusers can be modelled with the results of just a single plane wave calculation $k_{//}$ sweep.

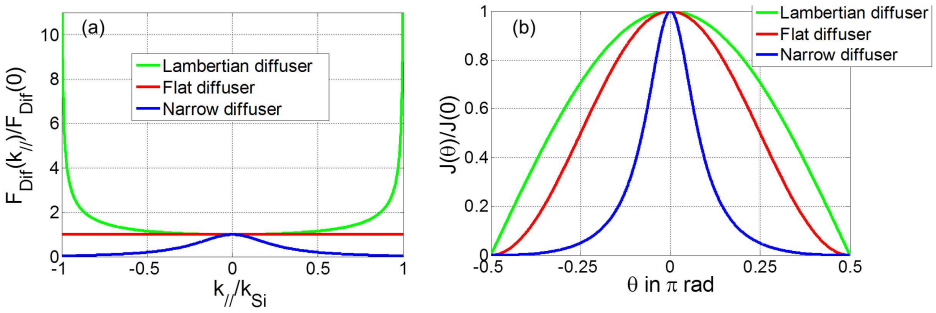

Figure 5.3: (a) The spatial power density spectrum of the wavefront coming out of various diffusers. (b) The corresponding radiant intensity profiles. θ is the angle relative to the normal of the diffuser surface. The narrow diffuser radiant intensity has a lorentzian shape with a linewidth of $\pi/6$ rad.

If one wishes to simulate for a realistic diffuser structure, one can infer the proper $F_{Dif}(k_{//})$ from radiant intensity measurements. Here, the back reflector is

assumed to not couple light to any evanescent component. The iterative procedure is stopped when the total power to be relaunched $P^n_{back}(\lambda)$ (towards +y) calculated with:

$$P^n_{back}(\lambda) = \sum_{k'_{//}} \Theta^n(k'_{//}, \lambda) \tag{5.2.20}$$

for $n > 1$ reaches zero.

5.3 Examples of OPC calculations for structures with various diffusers

As a first example, we show OPC calculations for a solar cell with a flat front surface with anti-reflection coating (50 nm ITO) together with a back reflector with various specular and 3D Lambertian diffuse components (Figure 5.4). Here, the single pass responses of the front surface were obtained via analytical calculations. The specular reflection component of the back diffuser in the OPC case is assumed to be uniform for all wavelengths and angles of incidence, but a more detailed characteristic can easily be implemented. For all wavelengths we simulate the excitation of plane waves with a homogeneous grid $\Delta k_{//} = 0.025 \times k_{Si}$. We then further interpolate the values of $A_{k_{//}}(\lambda)$, $R_{k_{//}}(\lambda)$, and $T_{k_{//}}(k'_{//}, \lambda)$ to a finer mesh with $\Delta k_{//} = 0.001 \times k_{Si}$. We utilize relaunched $k_{//}$ cases in the range of $-0.999 \times k_{Si} \leq k_{//} \leq 0.999 \times k_{Si}$. Due to symmetry of the front structures, we only need to simulate for positive or negative values of $k_{//}$. Here, the light is incoming at normal incidence, though any arbitrary of incidence angle is easily handled.

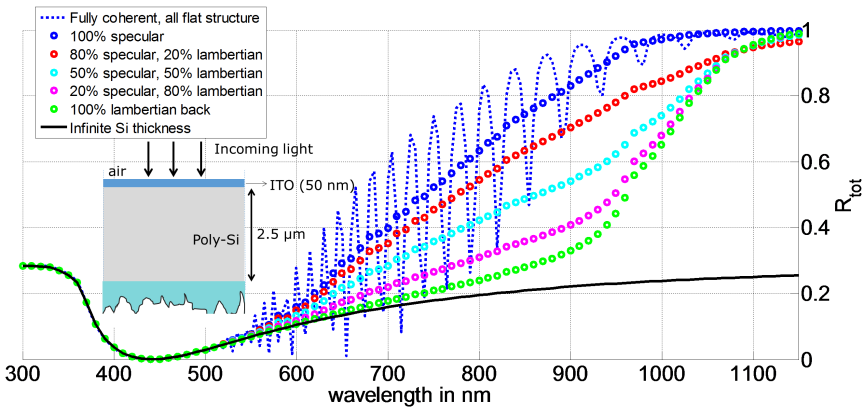

Figure 5.4: Reflectance spectra for flat top structures at normal incidence for different back reflectors. The inset shows the structure.

The blue dotted line in Figure 5.4 shows the coherent calculation result for the reflectance, assuming a perfect flat mirror at the back of the cell that is modelled with a perfect electric conductor boundary. The resonances are Fabry-Perot modes. The blue circles show the reflectance curve from OPC calculations for an all-flat structure (so with perfect specular reflection). We see that the OPC reflectance follows the average of the coherent case, as may be expected. The green circle plot shows the reflectance when we assume a 100% Lambertian diffuser at the bottom. There is a great decrease in reflectance due to the increased optical path length. The red, cyan and purple circle plots show the in-between cases where there is partial specular reflection by the back diffuser, 80%, 50% and 20% respectively. In the presence of 20% specular reflection, its performance is still comparable to that of a Lambertian diffuser, an important point for choosing a functional back reflector. The OPC method can complement reflectance and transmittance mea-

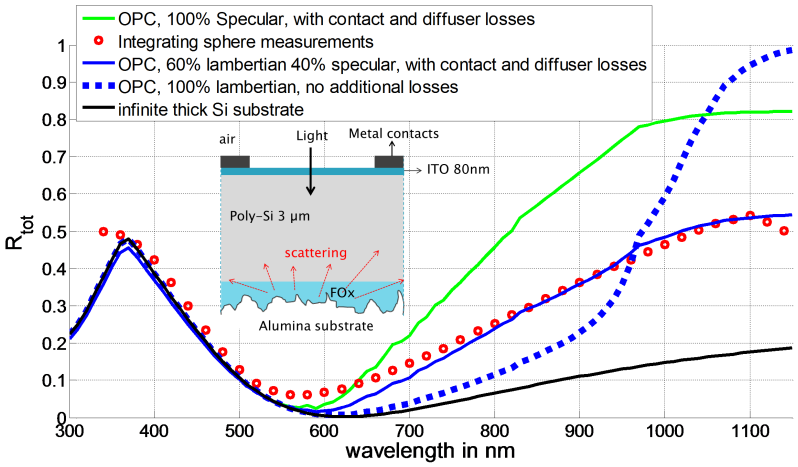

Figure 5.5: Measured reflectance spectrum of 3 μm Poly-Si solar cell sample compared to OPC simulation models. The black solid line shows the reflectance spectrum in the case of infinite Si thickness. For both the cases of solid green and blue line plots, additional 5% loss for all wavelengths at the front and back side of the cell is considered. The inset shows the structure.

surements to help understand the roughness of a layer in a certain structure. To demonstrate this we plot reflectance measurement results of a 3 μm poly-Si solar cell sample with a back alumina (Al_2O_3) bulk diffuser coated with flowable oxide (FOX in this case SiO_2) and compare it with several OPC simulation models of the same cell (Figure 5.5). The red circle plot shows the reflectance of the sample obtained from integrating sphere measurements of the sample. The blue solid line gives the OPC calculated fit of the measured spectrum, which assume addi-

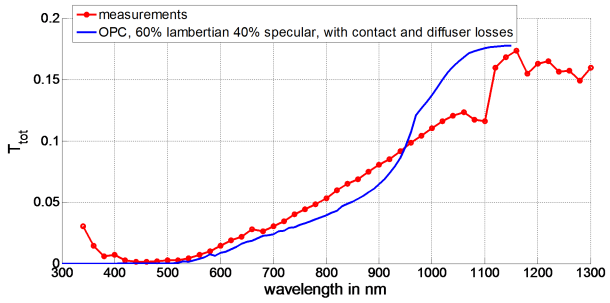

Figure 5.6: Measured transmittance spectrum of 3 μm Poly-Si solar cell sample compared to the OPC model with fitting parameters as in Figure 5.5.

tional front- and backside losses. The green line plot shows the OPC calculated reflectance assuming a specular back reflector with the same additional losses as for the blue solid line case. For both the cases of solid green and blue line plots, additional 5% loss for all wavelengths at the front and back side of the cell is considered. The blue dotted line gives the reflectance spectrum assuming a perfect Lambertian back diffuser with no additional losses.

Utilizing the OPC method we can study how well the diffusing component at the back of the sample helps with the light trapping. The back diffuser specular reflection component, front contact and diffuser transmission loss at every pass are considered to be the same for all wavelengths. With some rough fitting to account for the back diffuser specular reflection component and transmittance loss, and the top metal contact shadowing and absorption loss, we deduced that the back diffuser component of the cell is effectively 60% Lambertian and 40% specular. As can be seen in Figure 5.5) (comparing red circle plot and solid blue line plot), a fairly good agreement with the measurement is obtained with such specular/diffuse proportion. This good fit with measurements is obtained when the front and bottom of the cell is assumed to have additionally 5% loss at every light pass, which roughly accounts for the metal contact shadowing and diffuser transmittance loss.

A more accurate description of the back alumina diffuser can be obtained with Bidirectional Scatter Distribution Function (BSDF) measurements assuming there is no other layer in the structure that would also diffuse light. Our fitting parameters also reasonably reproduce the transmittance spectrum (Figure 5.6). With the OPC we can compare how well the alumina diffuser improves absorption as compared to a flat back reflector (green solid line of Figure 5.5) and a perfect lossless diffuser (blue dotted line of Figure 5.5). We envision that this method can help identify which component in a multilayered structure should be optimized in order to achieve the desired performance.

In what follows the full wave simulations to obtain the single pass responses

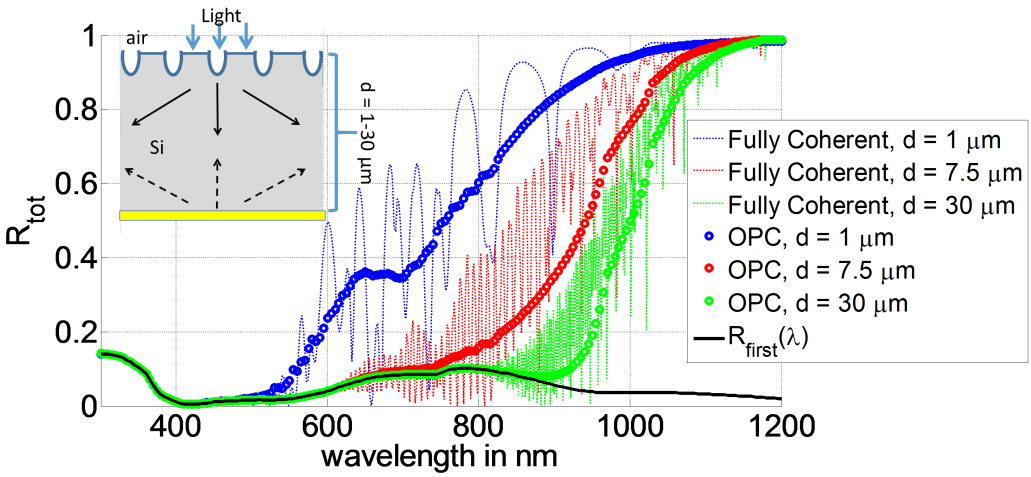

Figure 5.7: Reflectance curves for the fully coherent and one pass coherent cases for top grating-flat bottom solar cell structures with different Si thicknesses d. The top grating structure is the same as shown in Figure 5.1a with $P = 400$ nm. The black line plot gives the first pass reflectance (or reflectance when the Si thickness is infinite)

in the case of a patterned front surface were done using the finite element method (COMSOL), however any other tool can be employed. We mostly only consider 2D systems and plane waves with Transverse Magnetic (TM) polarization (no out-of-plane electric field) for simplicity and clarity as the phenomena described below are not polarization specific. The diffraction efficiency of TE waves can be different than that of TM waves but the same phenomena discussed below occur for TE waves also.

5.4 Implications of limited coherence on absorption

Before proceeding to discuss the light trapping effects of combined front grating-back diffuser structures (Section 5.5), we first discuss the effects of limited temporal coherence of light on solar cell absorption that is inherent in our calculations. It has been shown that light coherence can influence absorption in a 1D multilayer solar cell structure [4, 5]. Here, we show that having limited light coherence can improve absorption on average for a 2D solar cell structure over a fairly broad wavelength range when certain geometrical conditions are met.

In Figure 5.7 we compare the reflectance under fully coherent and OPC conditions for solar cell structures with a patterned front surface and a 100% specular bottom reflector. The geometric parameters of the grating are $P = 400$ nm, $FF = 0.7$, grating depth of 300 nm and ITO thickness of 50 nm. One can see that

the OPC reflectance can be lower than the average reflectance of fully coherent light, indicating that loss of coherence can increase absorption. This difference is seen to be significant only at intermediate thicknesses. For Si thickness d = 1 μm the OPC reflectance follows closely the average of coherent reflectance, as the OPC plot lies in between the peaks and the dips of the coherent resonances. In contrast, the difference between the OPC result and the coherent average is very apparent when d = 7.5 μm. This deviation again decreases for the thicker structures, e.g. when d = 30 μm. We note that this absorption dependence on coherence does not exist in flat cell structures, no matter how thick the cells are. Diffraction must be present in order to have this effect. In flat cells there will only be Fabry-Perot resonances and the reflectance under OPC conditions follows faithfully the coherent average.

The dependence of light absorption on coherence stems from the constructive phase relation necessary for waveguide modes. This phase condition restricts diffraction to high $|k_{//}|$ in the total internal reflection (TIR) regime to be efficient only in waveguide mode resonant conditions but inefficient otherwise. If phase relation is lost during propagation in the active material, as in our OPC case at the relaunch boundary, no such phase restriction exists. In effect, a discrete set of leaky waveguide states are exchanged with a broadband continuum of allowable states. Though one loses the strong absorption provided by leaky guided modes at resonant wavelengths, a more broadband absorption enhancement becomes possible and can on average improve the absorption performance. However, if the material absorption is too weak or if the optical path length is only slightly increased by diffraction, the absorption enhancement due to the limited coherence is not significant.

Single pass absorption of diffracted waves should not be too strong or too weak in order to see this coherence effect on absorption. In the extreme case when all the light at a certain wavelength is absorbed in a single pass, the total reflectance will converge to the first pass reflectance (the reflectance for infinite Si thickness) for both the OPC and coherent case. The particular wavelength edge, where interplay between front and back interface becomes important, depends on the Si thickness (around wavelength of 550 nm for d = 1 μm, 900 nm for d = 30 μm). Thus, absorption enhancement due to loss of coherence is typically apparent at intermediate wavelengths (around 800-1000 nm for Si), when light travels multiple passes in the active layer and certain geometrical conditions are fulfilled. A similar positive effect of limited coherence on solar cell absorption was also recently reported by Herman et al. from a quantum optical view point [12].

The thickness dependence of the limited coherence effect on absorption is traced back to the optical path length gain by scattering light to higher $|k_{//}|$ which is proportional to the thickness d. In the structure with top grating P = 400 nm at small thickness (d = 1 μm), there is not much gain in optical path length by diffrac-

tion and thus the effect is not significant. For d = 30 μm a significant portion of the diffracted waves would already be absorbed in a single pass and thus there is weaker OPC reflectance deviation from the fully coherent average. For in-between thicknesses such as d = 7.5 μm, light at longer wavelengths is not over-absorbed in just a single pass and there is significant increase of optical path length upon diffraction. Thus, this intermediate thickness range provides the prime condition for coherence to significantly influence on absorption as seen in our calculation results in Figure 5.7.

To quantify the coherence effect, we calculate a figure of merit in the wavelength region of 750-1200 nm

$$\gamma = (WIR_{FC} - WIR_{OPC})_{750-1200nm} \tag{5.4.1}$$

where *WIR* is the weighted integrated reflection of the AM1.5G solar spectrum which is defined as

$$WIR = \frac{\int R_{tot}(\lambda) \times P_{AM1.5G}(\lambda) d\lambda}{\int P_{AM1.5G}(\lambda) d\lambda} \tag{5.4.2}$$

$P_{AM1.5G}(\lambda)$ is the power spectrum of the AM1.5G solar radiation. The subscripts FC and OPC refer to the fully coherent and OPC condition, respectively. A higher *WIR* indicates less absorption. We choose this wavelength regime for Si cells, as the effect of limited coherence (and all light-trapping features) should be apparent there.

We plot γ as a function of Si thickness in Figure 5.8, and see that there is an optimal thickness, as the previous analysis predicts. A larger, positive γ means more absorption in the OPC case compared to the fully coherent case. The solar

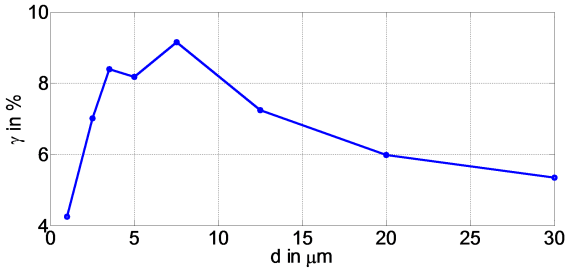

Figure 5.8: Plot of γ versus Si thickness d for the structure of Figure 5.7.

cell structure with d = 7.5 μm has around 9% less reflectance when incoming light has limited coherence. When the Si thickness is further increased, the difference in *WIR* approaches the initial value for the very thin thickness d = 1 μm. We also note that the fully coherent *WIR* is larger than the OPC *WIR* even at d = 1 μm,

where the OPC reflectance is close to the fully coherent average. This is due to the AM1.5G power spectrum and the nature of the Fabry-Perot resonances, which have a free spectral range (FSR) proportional to the square of the wavelength and inversely proportional to the thickness. The FSR will increase more rapidly at thin thicknesses as the wavelength increases, providing for less reflectance dips in the wavelength region of interest (Figure 5.7, coherent case for d = 1 μm).

As the effect of coherence depends on the absorption of diffracted waves, the periodicity of the grating also plays a major role as it dictates the diffraction angles. We compare in Figure 5.9 the reflectance of structures with a flat bottom and a grating top for P = 1000 nm and P = 400 nm with d = 2.5 μm and 7.5 μm. Comparing Figure 5.9a with b we see that the OPC case reflectance deviates more from the fully coherent average reflectance for lower periodicities. The fact that the γ values for P = 1000 nm are significantly lower than for P = 400 nm further demonstrates that the effect of limited coherence is weaker at larger grating periodicities. This is because the larger period mainly couples to less oblique angles. In the two thicknesses considered in Figure 5.9, the single pass absorption of the diffracted waves for P = 1000 nm is weaker than for P = 400 nm. Due to this, one can expect that optimum coherence effect on absorption will occur at larger thickness values where the single pass absorption of diffracted waves becomes strong enough.

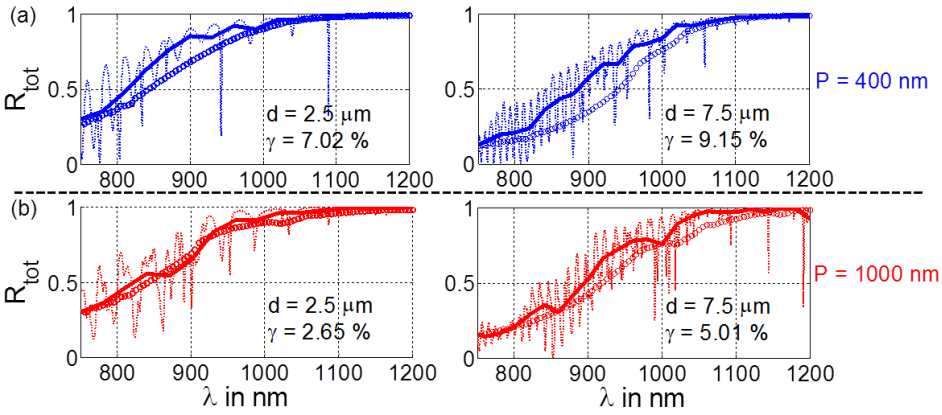

Figure 5.9: Comparing the fully coherent and OPC case for (a) P = 400 nm with d =2.5 μm and d = 7.5 μm, and for (b) P = 1000 nm with d = 2.5 μm and d = 7.5 μm. For all structures, the bottom reflector is 100% specular, FF = 0.7 and grating depth of 300 nm. The dotted line plots are the reflectance for the fully coherent case. The solid line plots are the average reflectance of the fully coherent case, with wavelength averaging window 20 nm. The circle plots are the reflectance for the OPC case.

5.5 Combined back diffuser and front grating

The combined front and back grating structure studied in the previous chapter focuses heavily on utilizing leaky guided modes to enhance solar cell absorption. In weakly absorbing materials such as crystalline Si relying on coupling to leaky guided modes for absorption enhancement is challenging. In such materials, the linewidth of leaky guided mode resonances tends to be extremely narrow (just a few nms) due to the weak absorption losses. One would then need to excite even more leaky guided modes to significantly enhance absorption and would thus require a grating structure with a very rich Fourier spectrum, which unavoidably leads to very complex geometries.

If the active material thickness of a solar cell is large enough, one would not need to rely on leaky guided modes to obtain a strong absorption enhancement. Provided that the active material supports a large carrier diffusion length, having a thicker active film is a viable and preferable option. This is even more true for c-Si and poly-Si based solar cells which not only can support carrier diffusion lengths of tens of μms and above, but are also now relatively cheap to produce [13]. Poly-Si and c-Si solar cells can have relatively large thicknesses of several μms and above (up to hundreds of μm for c-Si) due to their large diffusion length. With such thicknesses, light scattering that does not lead to guided mode coupling can still give strong absorption enhancement, as a slight deflection of several degrees may already result in a large optical path length increase. As a result, a random rough diffusing component in the solar cell structure may already provide strong absorption enhancement. Still, one is not required to solely rely on one light trapping element to enhance absorption as demonstrated in the previous chapter.

Here we propose the usage of both front gratings and back diffusers in a solar cell structure. The front gratings are intended to provide antireflection effects while the back diffuser is intended to give an increase of optical path length via additional scattering. Note that the effect of phase correlation loss is also present in the systems with back diffusers considered here. As a proof of principle, we mainly consider 2D systems and 2D Lambertian distributions, invariant along the z-axis.

We note that the improvement one obtains from a full 3D Lambertian system is significantly larger than for 2D systems as demonstrated in Figure 5.10 for the case of a flat front structure. This is so because a full 3D Lambertian wavefront inherently contains more high $k_{//}$ components. This however does not affect the main points we wish to show here.

In Figure 5.11 we show the total reflectance plot of the structure in Figure 5.1a for different back reflectors calculated under fully coherent and OPC conditions for Si thickness d = 2.5 μm. The black dotted line gives the fully coherent calculation for an all flat structure. By introducing the grating pattern on the front of the cell

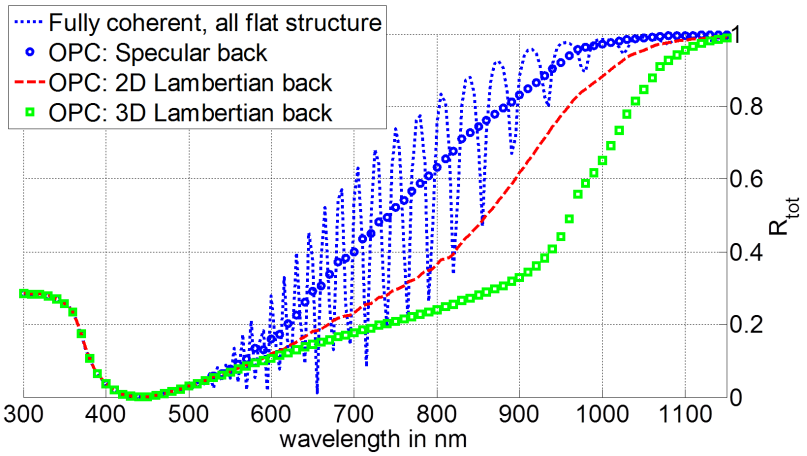

Figure 5.10: Comparison of light trapping by 2D and 3D Lambertian diffusers.

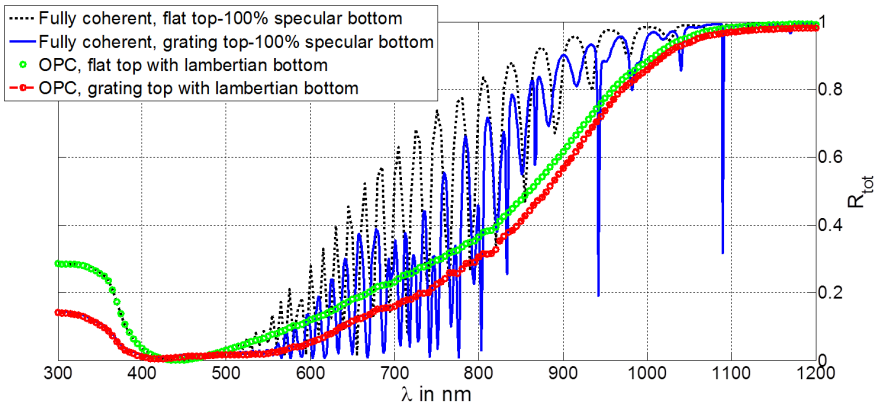

Figure 5.11: Total reflectance plot of the structure showed in Figure 5.1a for Si thickness d = 2.5 μm and compared with reflectance of the unpatterned top structure

(solid blue line), we see a significant reduction in the total reflectance already. The front grating pattern mainly gives antireflection effects and additionally induces light scattering and allows coupling to guided modes. The total reflectance of the structure when there is additionally a Lambertian diffuser at the back side of the cell can be seen from the red circle plot. When comparing the solid blue line plot and the red circle plot, we see that the Lambertian diffuser works together with the top grating to enhance absorption. The role of the top grating in the combined system can be clearly understood by comparing the red circle plot with the total reflectance for a structure with only the back Lambertian diffuser (green

circle plot). There we see that the back Lambertian diffuser only cell (without front grating) has a worse performance at lower wavelengths though one observes a similar performance at longer wavelengths.

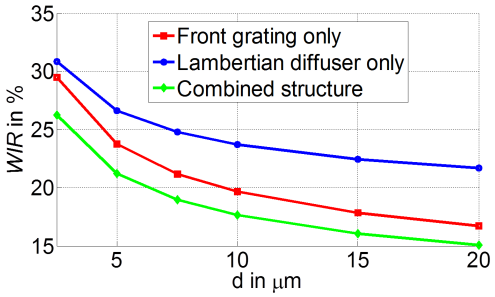

Figure 5.12: Plot of WIR versus d assuming the front pattern of the cell is the same as in Figure 5.1a. Lower WIR is better.

The thickness of the cell is an important factor that affects how well the front grating and back diffuser work together. A plot of the weighted integrated reflectance (WIR) versus the Si thickness (d) is shown in Figure 5.12. With the grating structure we focus on here, the combined structure performs better (gives less reflectance) for the whole thickness range considered. For combined and single component structures, the total reflectance is less if the thickness is larger. Note however, the WIR of the grating only structure approaches that of the combined structure as thickness increases, which is due to the single pass absorption becoming stronger. Thus, one can expect that beyond a certain thickness, a front grating pattern will already give sufficient light trapping. Interestingly, this already occurs at a fairly low thickness for thin-film Si cells. In our 2D system here, when the Si thickness is beyond 10 μm, the difference between the combined and the grating only structure is less than 2%.

The effect of thickness on the reflectance spectra is shown in Figure Figure 5.13. The combined and grating only structure reflectance overlaps in the lower wavelength region due to high single pass absorption. As the Si thickness increases, this region where the overlap occurs widens due to more wavelengths experiencing large single pass absorption. Another important factor that affects how well the combined structure performs is the escape transmittance ($R_{k_{//}}$) of waves coming out of the Si. To be more specific $R_{k_{//}}$ is the power portion of light incoming from the bottom of the cell (launched from the relaunch boundary) that is escaping to air. The presence of the grating disrupts the total internal reflection (TIR) of the Si-air interface. Due to the grating, diffused light incoming to the front of the cell that would normally be total internally reflected can escape to air. This is illustrated in Figure 5.14 which shows $R_{k_{//}}$ with and without the

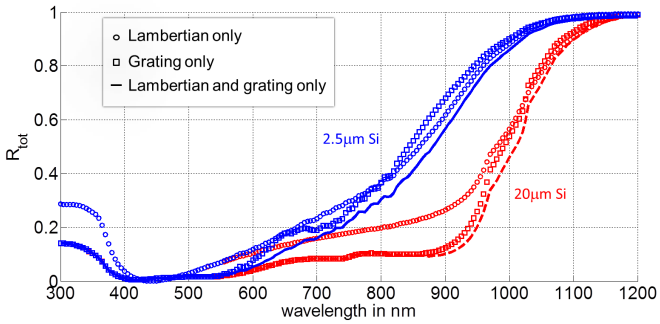

Figure 5.13: Plot of total reflectance for the combined and single component structures for thicknesses d = 2.5 μm (blue) and d = 20 μm (red).

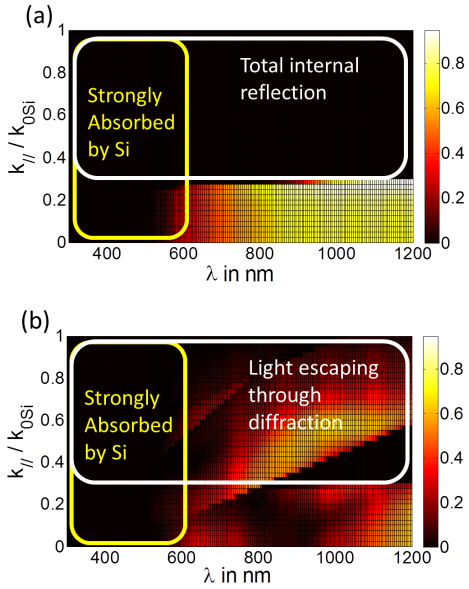

Figure 5.14: Escape transmittance ($R_{k_{//}}$) of relaunched plane waves for (a) flat top structure (d = 2.5 μm) and (b) grating top (P = 400 nm, d = 2.5 μm). In all cases the ITO thickness is 50 nm.

presence of the grating structure. The disruption of TIR is the reason why adding a Lambertian diffuser at the back in the presence of a front grating leads to less reflectance reduction than if the front is unpatterned, though the combined structure can still have less reflectance. Ideally, the front grating structure should not have

a high $R_{k_{//}}$ in the $k_{//}$ (angle) region where the diffuser wavefront Fourier components are strong. This escape transmittance depends heavily on the geometry of the grating structure and should be considered in the optimization process of the top grating while maintaining a low first-pass reflectance.

5.6 Summary

A calculation method to efficiently address structures that have wave and ray optics segments is discussed. The One-Pass Coherent (OPC) calculations take wave effects into account where they matter the most, while evading a large computational domain to model rough structures. A general rough diffuser is handled directly via the reflected wavefront instead of its geometry. A single plane wave calculation sweep provides all the information to calculate any kind of bottom diffuser.

We demonstrate that limited light coherence can lead to stronger absorption over a fairly broad wavelength range for an important range of Si thicknesses. A loss of phase relation between waves incoming and waves reflected from the back in effect exchanges a discrete set of leaky wave-guide states in the active material film with a broadband continuum of allowable states. Though one loses the strong absorption provided by leaky guided modes at resonant wavelengths, a more broadband absorption enhancement becomes possible and can on average improve the absorption performance. Therefore, the back reflector in advanced thin-film devices needs careful consideration.

We further utilize the calculation method to study solar cell structures that combine a grating at the front and a rough diffuser at the back, which has been realized in state-of-the-art thin-film Si devices [14]. This is an extension of the double component study of the previous chapter towards rough surfaces and partially coherent elements. Results show that the combined structures provide significantly more light trapping capabilities than single element devices in an important poly-Si thickness range.

References

[1] J. S. C. Prentice. *Coherent, partially coherent and incoherent light absorption in thin-film multilayer structures*. Journal of Physics D-Applied Physics, 33(24):3139–3145, 2000.

[2] C. C. Katsidis and D. I. Siapkas. *General Transfer-Matrix Method for Optical Multilayer Systems with Coherent, Partially Coherent, and Incoherent Interference*. Applied Optics, 41(19):3978–3987, 2002.

[3] E. Centurioni. *Generalized matrix method for calculation of internal light energy flux in mixed coherent and incoherent multilayers*. Applied Optics, 44(35):7532–7539, 2005.

[4] M. C. Troparevsky, A. S. Sabau, A. R. Lupini, and Z. Zhang. *Transfer-matrix formalism for the calculation of optical response in multilayer systems: from coherent to incoherent interference*. Optics Express, 18(24):24715–24721, 2010.

[5] R. Santbergen, A. H. M. Smets, and M. Zeman. *Optical model for multilayer structures with coherent, partly coherent and incoherent layers*. Optics Express, 21(S2):A262–A267, 2013.

[6] W. Lee, S.-Y. Lee, J. Kim, S. C. Kim, and B. Lee. *A numerical analysis of the effect of partially-coherent light in photovoltaic devices considering coherence length*. Optics Express, 20(S6):A941–A953, 2012.

[7] P. Spinelli, M. A. Verschuuren, and A. Polman. *Broadband omnidirectional antireflection coating based on subwavelength surface Mie resonators*. Nature Communications, 3:692, 2012.

[8] A. Abass, C. Trompoukis, S. Leyre, M. Burgelman, and B. Maes. *Modeling combined coherent and incoherent scattering structures for light trapping in solar cells*. Journal of Applied Physics, 114(3), 2013.

[9] A. Starikov and A. T. Friberg. *One-dimensional Lambertian sources and the associated coherent-mode representation*. Applied Optics, 23(23):4261–4268, 1984.

[10] W. H. Carter and E. Wolf. *Coherence properties of lambertian and non-lambertian sources*. Journal of the Optical Society of America, 65(9):1067–1071, 1975.

[11] A. Donges. *The coherence length of black-body radiation*. European Journal of Physics, 19(3):245, 1998.

[12] A. Herman, M. Sarrazin, and O. Deparis. *The fundamental problem of treating light incoherence in photovoltaics and its practical consequences*. New Journal of Physics, 16(1):013022, 2014.

[13] A. Goodrich, P. Hacke, Q. Wang, B. Sopori, R. Margolis, T. L. James, and M. Woodhouse. *A wafer-based monocrystalline silicon photovoltaics road map: Utilizing known technology improvement opportunities for further reductions in manufacturing costs*. Solar Energy Materials and Solar Cells, 114(0):110 – 135, 2013.

[14] C. Trompoukis, A. Herman, O. El Daif, V. Depauw, D. Van Gestel, K. Van Nieuwenhuysen, I. Gordon, O. Deparis, and J. Poortmans. *Enhanced absorption in thin crystalline silicon films for solar cells by nanoimprint lithography*. In R. Wehrspohn and A. Gombert, editors, Photonics for Solar Energy Systems IV, volume 8438 of *Proceedings of SPIE*. SPIE, 2012.

6

Hybrid plasmonic-photonic modes

6.1 Introduction

Electromagnetic modes that occupy the same spatial and spectral region can have a coupling interaction with each other to form a hybrid mode with mixed characteristics [1–4]. Such mode hybridization attracts a broad scientific interest due to the possibility of mixing desirable characteristics from different photonic resonances. In particular, a lot of attention is directed to hybrid plasmonic-photonic modes. While plasmonic resonances are of great interest for diverse applications due to their strong near field enhancement and scattering properties, these modes tend to be lossy, and there are limited possibilities to tune their field profile. Hybrid plasmonic-photonic modes, on the other hand, can be tailored far more flexibly as one can mix in the properties of other resonances. One can, for example, engineer a mode that provides a fairly strong near field enhancement while having a low loss and thus narrow linewidth as demonstrated in this chapter. For emission or other light-matter interaction enhancement purposes, such qualities in an optical mode are highly desirable. On top of this, hydrid plasmonic-photonic modes can be tailored to have a strongly directional emission enhancement as they can be engineered to couple with just one or a few discrete radiation plane waves.

In recent years periodic arrays of metallic nanoparticles have attracted much attention for their ability to support hybrid plasmonic-photonic modes. In particular 2D arrays can support hybrid surface modes arising from the radiative coupling between Localized Surface Plasmon Resonances (LSPRs) and waves diffracted

in the plane of the array [Rayleigh Anomalies (RAs)] [4–14]. The SLR dispersion and linewidth is flexibly tunable via the particle geometry and lattice constant [4, 14]. Similar hybrid surface modes have also been observed in metallic gratings [15–18], subwavelength hole arrays [19–22], nanoslit arrays [23, 24], stacked plasmonic nanowire arrays [25] and particle arrays coupled to waveguide modes [26, 27]. When periodic arrays of metallic nanoparticles are placed near a waveguide structure, the LSPR of each metallic nanoparticle may also couple with waveguide modes. The resulting hybrid mode is known as the waveguide plasmon polariton (WPP) [26, 27]. Similar to the SLRs, the WPPs properties are tunable by the geometry. Recent works have demonstrated the advantages of hybrid plasmonic-photonic modes in enhancing the spontaneous emission of luminescent molecules or quantum dots within the vicinity of the array [27–29], in lasing [30], and in refractive index sensing [31].

Despite the many studies concerning SLRs and WPPs, their general properties in terms of the coupling conditions between the participating modes are limitedly explored. The work of Barnes and co-workers gave a good insight on the coupling between distinct surface plasmon polaritons in metallic sinusoidal gratings [16]. However, the analysis there is not easily extended to more complex plasmonic structures and SLRs. Another important study was presented recently by Teperik and Degiron [14], who explained how the SLR energy and linewidth (at normal incidence only) can be tuned by tailoring the polarizability tensor describing the nanoparticles. While such an approach is appealing from a theoretical standpoint, experimental implementation is difficult as it requires *a priori* knowledge of how the particle dimensions (the experimentalist's turning knob) relate to the polarizability tensor.

The next three sections of this chapter elucidate how a hybrid mode's characteristics depend on the spectral properties of the interacting resonances, which are in turn determined by geometry. This part of the work is a result of a joint collaboration between the Surface Photonics Group in the FOM Institute AMOLF, the Micro- and Nanophotonic Materials Group at the University of Mons and the Solar Cells Group at Ghent University.

We firstly focus on SLRs in nanorod arrays where RAs associated with two diffraction orders [(+1,0) and (-1,0)] interact with a single first order LSPR. Experimental extinction spectra of arrays with gold nanorods of different dimensions are measured by our collaborators in the Surface Photonics group in AMOLF. The nanorod dimensions determine the energy and linewith of the LSPR, and thus the detuning with respect to the RAs in arrays with fixed periodicity. We focus on the case of light polarized along the width of the nanorod where the LSPR red-shifts and broadens for increasing nanorod width due to the depolarization field along this dimension [32]. Our work analyzes how this changes the coupling of the LSPR to the RAs. Transmission and eigenmode calculations using finite element

based methods were done to elucidate the physics of the SLRs. The eigenmode numerical simulations illustrate how the SLR field profile varies for different LSPR-RA energy detunings, including changes in periodicity and in-plane momentum. These eigenmode profiles can be described by a straightforward plane wave model, highlighting on the subtle interferences at play.

In addition, we discuss the usage of liquid crystals (LCs) to actively tune hybrid plasmonic-photonic modes. This part of the work is a joint collaboration between the Surface Photonics Group in the FOM Institute AMOLF, Philips Research Laboratories, the Micro- and Nanophotonic Materials Group at the University of Mons, and Ghent University which includes the Liquid Crystal and Photonics Group, the Physics and Chemistry of Nanostructures Group, and the Solar Cells Group. The tuning of extinction and photoluminescence (PLE) enhancement properties of a hybrid plasmonic-photonic mode is experimentally and theoretically demonstrated. In accomplishing this, an Al nanodisk array is fabricated by Philips Research Laboratories on top of an emitting layer consisting of colloidal semiconductor quantum dots (QDs), and then coated with LCs. The utilized CdSe/CdS/ZnS core-shell QDs were synthesized by the Physics and Chemistry of Nanostructures Group at Ghent University. After synthesis, the QDs were deposited on a glass substrate by spin coating. The LC deposition was done by the Liquid Crystals and Photonics Group at Ghent University. Here, the active tuning was done via a temperature change. Both extinction and photoluminescence were measured by the Surface Photonics Group in AMOLF at temperatures well below and above the LC critical temperature (T_c), where the effective refractive index of the LC changes from birefringent to isotropic. We performed finite element method (FEM) simulations to examine the modal field profile, and elucidate the physics behind the tuning mechanism.

The work shown in this chapter paves the way for better light-matter interaction enhancement utilizing such hybrid plasmonic-photonic modes. The concepts described here can also be useful in the context of spectral management for solar energy conversion. More specifically, the emission enhancement provided by hybrid plasmonic-photonic modes may also be used to enhance photon up and down conversion processes useful for solar cells. Enhancing these processes would enable one to more effectively utilize the incoming solar spectrum, even the spectral range that is not normally contributing to current generation for a certain solar cell. In the framework of such solar cell applications, the current work is still preliminary. Though we did not work on utilizing these modes for specific up/down conversion materials, the concepts shown here will be applicable for it.

Section 6.2 discusses the experimental observation of SLRs in five gold nanorod arrays with varying rod width. Section 6.3 presents the transmission and eigenmode simulations to understand these experimental results. Section 6.4 shows a plane wave model that can be used to intuitively understand the eigenfield profile

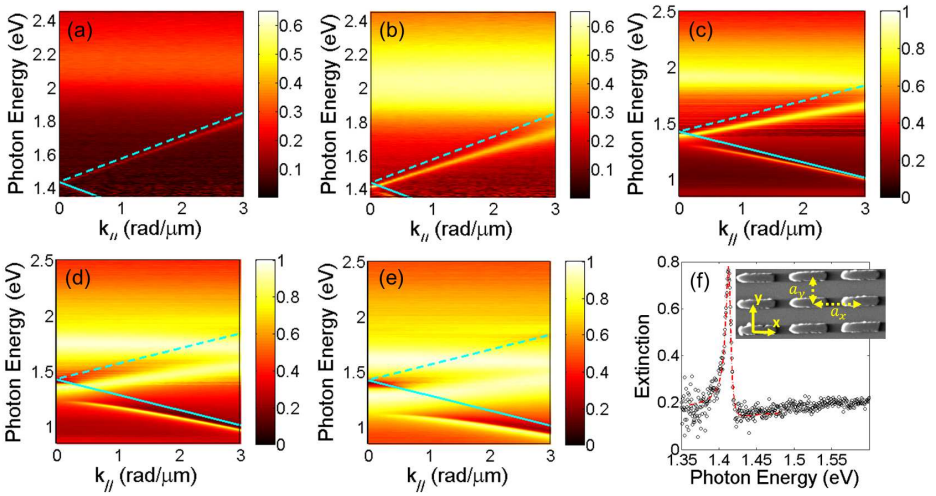

Figure 6.1: Experimentally measured extinction for (a) w = 70 nm, (b) w = 110 nm, (c) w = 160 nm, (d) w = 200 nm, and (e) w = 230 nm. (f) Experimental extinction at $k_{//} = 0$ for w = 110 nm array, fitted with a Fano resonance (red dashed lines) for the upper SLR. The inset in (f) shows the SEM picture of the nanorod array with w = 110 nm.

and radiation paths of the SLR modes. Section 6.5 discusses active liquid crystal tuning of a hybrid plasmonic-photonic mode and photoluminescence enhancement via temperature change.

Most of Section 6.2-6.4 in this chapter was presented in our paper in Ref. [33].

6.2 Experimental tuning of surface lattice resonances

The Surface Photonics Group in AMOLF fabricated five gold nanorod arrays with varying nanorod width (*w*) of 70, 110, 160, 200 and 230 nm (in the y direction) but equal nanorod length of 450 nm (in the x direction) on a silica substrate using electron beam lithography. The arrays have dimensions of 1.5×1.5 mm^2 and lattice constants $a_x = 600$ nm and $a_y = 300$ nm. The nanorods have an approximately rectangular shape in the plane of the array, and a height of 40 ± 2 nm. The rod width was tuned by varying the exposure dose of the electron beam. The tolerances of the in-plane dimensions are on the order of ± 10 nm. The arrays were embedded in a uniform surrounding medium by placing a silica superstrate preceded by $n = 1.45$ index matching fluid to ensure good optical contact.

Figure 6.1a-e shows the extinction of y polarized light measured by the Surface Photonics Group, defined as $1 - T_0$ with T_0 the zeroth-order transmittance, for the five arrays described above. The extinction is displayed in color as a function of the incident photon energy and component of the wave vector parallel to the

surface in the x direction, which is given by $k_{//} = \frac{E}{\hbar c}\sin\theta$, with θ the angle of incidence from the normal. The samples were rotated around the y-axis, while the y-polarized collimated beam from a halogen lamp impinged onto the sample, probing the short axis of the nanorods.

The broad extinction peak with a flat dispersion seen on the high energy side of the extinction spectra for all five arrays corresponds to the excitation of LSPRs in the individual nanorods. The cyan solid and dashed lines indicate the $(-1, 0)$ and $(+1, 0)$ RAs, respectively. The RAs are solutions to the equation $E_{\pm} = \frac{\hbar c}{n}|k_{//} + mG_x|$, where $m = \pm 1$ is the order of diffraction, and $G_x = 2\pi/a_x$ is the x-component of the reciprocal lattice vector. The coupling of the LSPR to the two RAs yields the upper and lower SLRs. The SLRs are dispersive bands in extinction with variable linewidth, following the dispersion of the RAs on the low energy side. Note that the LSPR should also feel the hybridization effect and have its properties altered by the RA resonances. However, due to the narrow linewidth of the RA resonances, this effect will only be prominent when the RA is close to the LSPR.

At $k_{//} = 0$, the upper SLR is bright (normal incident plane wave can excite it), while the lower SLR is dark (i.e., it is not excited by normal incident plane wave). The difference in energy of the bright and dark SLR at $k_{//}$ is connected to the different eigenfield profile distribution which determines the energy of each mode. We note that this is not a complete bandgap, since it exists only for light polarized parallel to the short axis of the nanorods (y direction) and for an in-plane wave vector component parallel to the long axis of the nanorods. For light polarized parallel to the long axis of the nanorods, the dipolar LSPR lies at lower energies than the ($\pm$1, 0) RA diffraction orders at normal incidence and largely detuned from the RAs, which results in a weak diffractive coupling [10]. On the other hand, for an in-plane wave vector component parallel to the short axis of the nanorods, the $(\pm 1, 0)$ Rayleigh anomalies are degenerate, leading to degenerate $(\pm 1, 0)$ SLRs and therefore to the absence of a gap [34].

The extinction measurements in Figure 6.1a-e show a clear correlation between the SLR characteristics and the spectral properties of the LSPR and RA resonances. As the LSPR broadens and approaches the RAs in energy upon increase of *w*, the SLRs shift towards lower energies, their linewidths broaden, and the gap between the upper and lower SLR widens. The SLR dispersion also deviates more strongly from the associated RA for increasing *w*. This indicates that the coupling strength between LSPRs and RAs increases. The broadening of the SLR linewidth, which implies increased losses, can be understood on the basis of the increased influence from the lossy LSPR. The effect of LSPR-RA energy detuning can also be observed in the SLR dispersion of each array. As $k_{//}$ increases the detuning between the upper SLR and LSPR diminishes. Consequently, the SLR linewidth broadens and its peak energy deviates more pronouncedly from the

(+1,0) RA. In contrast, the lower SLR becomes narrower and approaches the (-1,0) RA as it becomes more detuned from the LSPR.

The SLRs can exhibit relatively narrow linewidths for plasmonic type resonances. To obtain the linewidths of these SLRs, we fit the extinction measurements with a Fano model of the form: $F = A_0 + A\frac{(q\alpha/2+E-E_0)^2}{(E-E_0)^2+(\alpha/2)^2}$. A_0, A, q, α, and E_0 are the fitting parameters, which we determine by a least squares method. Figure 6.1f shows the Fano fit of the upper SLR at $k_{//}$ = 0 for *w* = 110 nm, from which we obtain the linewidth (α) to be 8.29 meV $\pm$ 0.56 meV and resonant frequency (E_0) to be 1.413 eV $\pm$ 0.269 meV. The Fano shape of SLRs can be expected as they arise from the coupling between a broad LSPR and narrow RA resonances [3, 4]. These resonances, commonly arising from a broad resonance interacting with narrow resonances, have been found in various other plasmonic systems [1–3].

6.3 Transmission and eigenmode simulations of SLRs

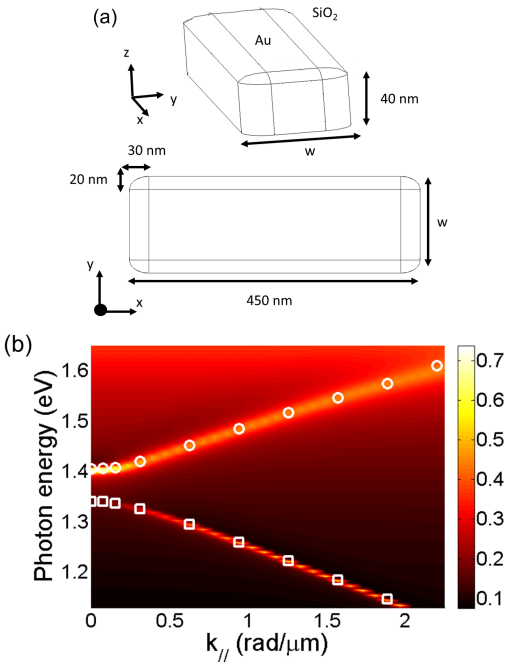

Figure 6.2: (a) Diagram of the simulated nanorods. (b) Simulated extinction (color plot) dispersion for w = 110 nm. White markers indicate the eigenfrequencies of the SLR modes obtained through eigenfrequency calculations. Circle and square markers indicate data points for upper and lower SLR respectively.

The SLR characteristics in driven and undriven conditions were examined by finite element method simulations (COMSOL). The tranmission of plane waves impinging on the nanorod arrays from various angles was calculated to obtain the extinction spectra. The extinction was calculated as $1-T_0$, with T_0 the zeroth order transmission obtained by Fourier decomposition. Figure 6.2a shows a sketch of the nanorods in the simulated arrays. Figure 6.2b shows the simulated extinction of the *w* = 110 nm array.

Our simulations reproduce the SLR characteristics observed in the measurements, and similar agreement was obtained for other arrays. The SLR peak energies obtained from the transmission simulations serve as an initial guess and check for the eigenenergies in the un-driven case obtained from eigenmode calculations.

To show the near-field enhancement capability of a hybrid plasmonic-photonic mode, we show cross-section plots of $\frac{|E|}{|E|_{\text{incoming}}}$ at the bright SLR resonance condition for *w* = 110 nm at $k_{//} = 0$. As can be seen in Figure 6.3(a) and (b), a strong near field $|E|$ enhancement of up to 7 times in the xz plane and 18 times in the xy plane respectively is achieved. Note that in our simulation such a strong

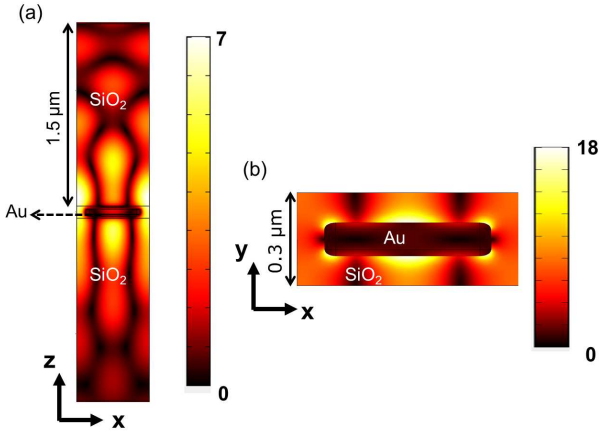

Figure 6.3: (a) xz cross-section and (b) xy cross-section plots through the center of the nanorod of the simulated electric field enhancement profile $\frac{|E|}{|E|_{incoming}}$*. The plots are taken for* w *= 110 nm at* $k_{//} = 0$ *and incoming photon energy of 1.401 eV which is the bright mode extinction peak.*

near field enhancement is obtained while having a narrow resonance linewidth of 8.5 meV (which is in agreement with the measured linewidth). This demonstrates that hybrid plasmonic-photonic modes may offer a strong near field enhancement without the large loss common for pure plasmonic resonances.

With the eigenmode simulations we focused on finding Bloch modes that propagate in the plane of the array along the x-direction which would corresponds to

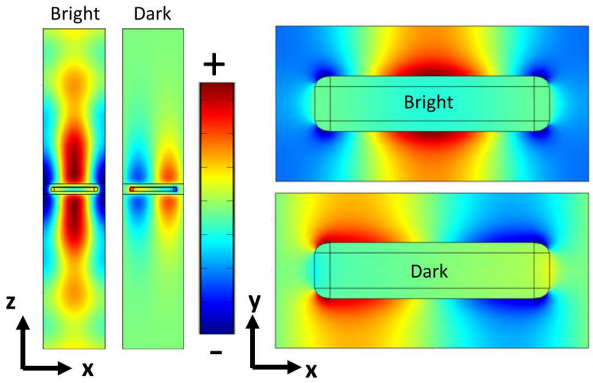

Figure 6.4: Eigenmode E_y plot cross-sections of bright and dark modes at the xz and xy plane at the center of the nanorods for w = 110 nm at $k_{//} = 0$.

the SLRs. The SLR eigenenergies calculated at a few values of $k_{//}$ are plotted as white circles and squares in Figure 6.2b. The good agreement of the SLR dispersion obtained with eigenmode and transmission simulations confirms that the obtained Bloch modes are indeed SLRs and thus validate our eigenmode calculations.

The radiative properties of the SLRs can be understood by inspecting their eigenfield profile. Figure 6.4 shows the y-component of the upper and lower SLRs eigenfield at $k_{//} = 0$ for *w* = 110 nm array. In both planes (xz and xy) intersecting the unit cell at its center, it is shown that the eigenfield E_y has even parity for the upper SLR and odd parity for the lower SLR (with respect to the yz plane through the particle center). The odd parity of the lower SLR renders the mode dark at normal incidence, i.e. it cannot be excited by a normal incident plane wave. This is due to the fact that the array cannot scatter the normal incident plane wave to produce an antisymmetric field profile required for coupling to an antisymmetric mode. On the other hand, the upper SLR clearly has a field profile that is not strictly confined to the nanorod, as it has a radiative component unlike the lower SLR. The symmetries of the upper and lower SLR eigenfields are the same for arrays with different *w* (other dimensions fixed), but with different eigenenergies. In Figure 6.5 we show how, as *w* increases and the LSPR-RA energy detuning decreases, the SLRs are shifted to lower energies and the gap widens, in agreement with our measurements ($k_{//} = 0$ in Figure 6.1a-e).

The influence of the nanorod width *w* on the eigenfield profile of the upper and lower SLRs are shown in Figure 6.6a and Figure 6.6b respectively. The near field confinement of both SLRs is enhanced as *w* increases. This effect is more clearly visible for the lower SLR, as this mode lacks a radiative component. In

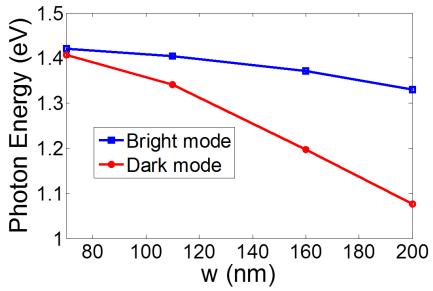

Figure 6.5: SLR energy dependence on nanorod width at $k_{//}$ = 0 obtained from eigenmode calculations.

contrast, the upper SLR retains a radiative component for all *w*. Concentrating on the spatial region away from the nanorods in Figure 6.6a, we observe that the magnitude of the eigenfield increases as *w* increases. Since the fields in this region are mostly radiative in character, it follows that the radiative portion of the total loss also increases with increasing *w* for the upper SLR. This effect, in combination with the increased near field confinement, which naturally leads to larger Ohmic losses, can thus be expected to increase the linewidth of the upper SLR at $k_{//} = 0$ in the driven system. The latter observation is very clear from the experiments (Figure 6.1a-e).

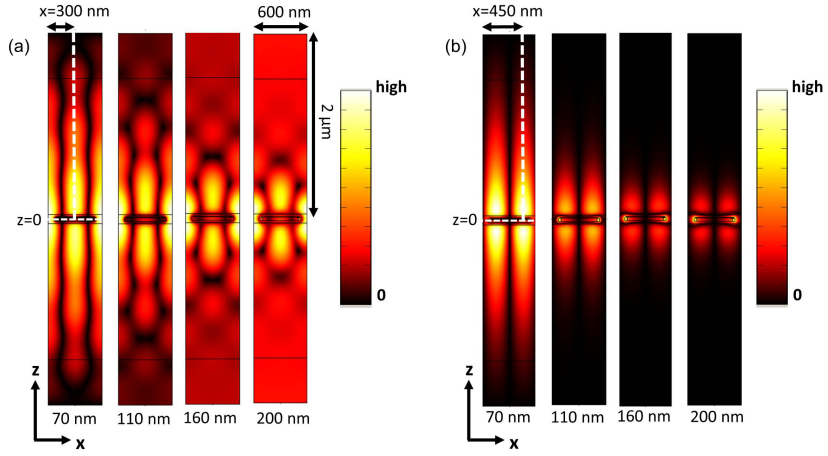

Figure 6.6: xz cross-section plot through the center of the nanorod of the eigenmode $|E|$ profile of (a) bright and (b) dark modes for different w at $k_{//} = 0$. Each $|E|$ plot has a different normalization individually. The dimension listed is the nanorod width (w).

To further elucidate the trends in Figure 6.6, we show cross-sections of the nor-

malized eigenfield magnitude in Figure 6.7. The cross-sections are taken along the dashed line in Figure 6.6, and normalized to the first maximum encountered in the dielectric medium. The upper SLR eigenfields in Figure 6.7a display oscillations due to interference between the near-field and far-field (radiative) components of the eigenmode. In the far field regime away from the nanorods, the magnitude reaches a "plateau". This asymptotic behaviour can be seen in Figure 6.7a for the nanorod array of w = 160 nm starting at a distance of 1.5 μm and is more apparent for arrays of wider nanorods.

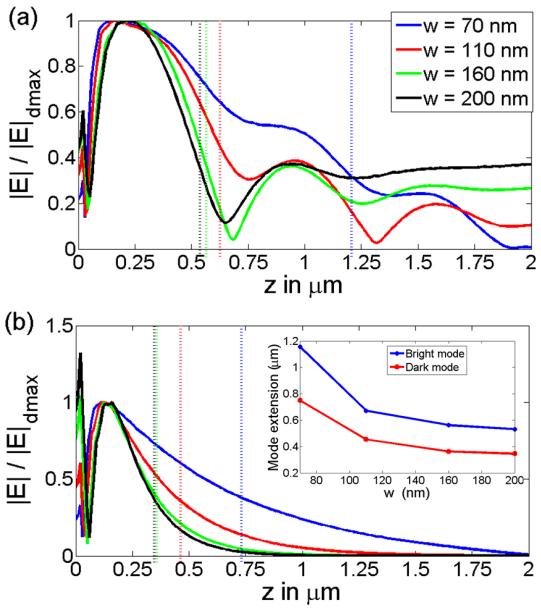

Figure 6.7: Normalized cross-section of (a) bright mode and (b) dark mode field profile at $k_{//} = 0$. The vertical dotted lines indicate the field extension for each array according to the definition described in the text. The inset of (b) shows the plot of the dark and bright mode field extension.

The radiative component of the upper SLR dominates in the region where this plateau sets in. The plateau indicates coupling of the upper SLR to a single radiative plane wave channel as will be demonstrated more clearly later in the discussion of radiative losses and in the plane wave model section. The onset of the plateau is more visible for wider nanorods, as it occurs at shorter distances away from the nanorods due to the near-field portion of the mode being more tightly confined.

The physics is simpler for the lower SLR eigenfield, which decreases monotonously in the dielectric medium as shown in Figure 6.7b. The inset in Figure 6.7b shows a plot of the spatial extent of the upper and lower SLRs eigenmodes as a function of w. The mode extension is taken to be the distance where the eigenfield mag-

nitude drops to $1/e$ for the first time after the normalization point. There, it can be observed that both SLR eigenmodes become increasingly confined for wider nanorods, again consistent with increasing losses and experimentally observed increasing linewidths for the bright mode at $k_{//} = 0$ in Figure 6.1.

The upper and lower SLRs radiative and field confinement properties evolve differently as $k_{//}$ changes. Figure 6.8a shows a plot of the total electric eigenfield magnitude (color plot) and Poynting vector (arrows) for *w* = 110 nm at different $k_{//}$ for the upper SLR.

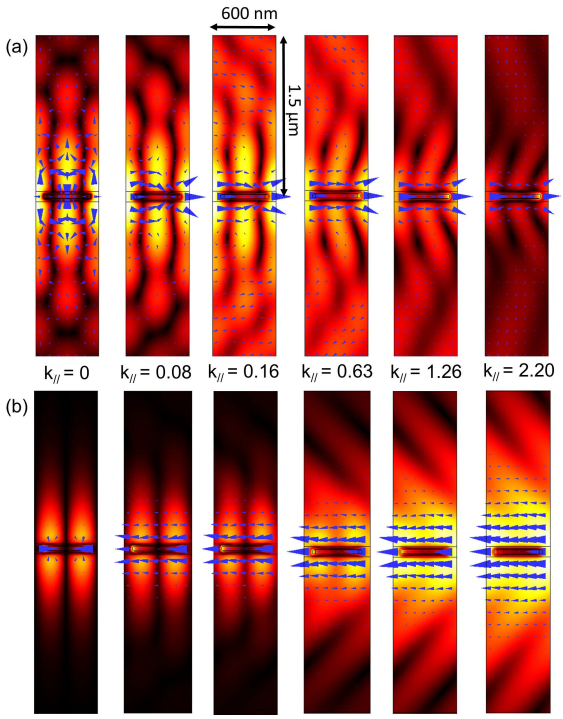

Figure 6.8: (a) Upper SLR and (b) lower SLR modal field profile evolution as $k_{//}$ is increased for w = 110 nm (xz cross-section through the center of the nanorod). The shown $k_{//}$ values are in units of rad/μm and directed to the right. The blue arrows indicate the Poynting vector.

There, we can identify different regimes for the upper SLR depending on the value of $k_{//}$. In the low momentum regime ($k_{//} \leq 0.16$ rad/μm), the eigenfield magnitude far away from the nanorods ($> 1\mu$m) increases relative to the magnitude in the near field as $k_{//}$ increases. As in the case of the nanorod widening, this apparent increase of far field magnitude suggests an increase in radiative losses at intermediate $k_{//}$ which will be discussed later. For higher momenta ($k_{//} \geq 0.16$

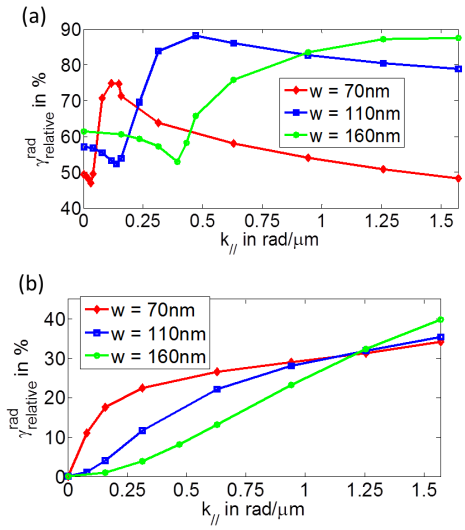

Figure 6.9: Relative radiative loss portion of the (a) upper SLR and (b) lower SLR for different nanorod widths.

rad/μm), the eigenfield magnitude away from the nanorods ($> 1\mu$m) decreases relative to the magnitude in the near field. This trend at high $k_{//}$ is due to the increase of near field confinement as the SLR approaches the LSPR and obtains a more localized nature.

As before, the eigenfield profile evolution of the lower SLR is more monotonous (Figure 6.8b). As $k_{//}$ increases the radiative component of the lower SLR increases and the mode becomes less confined. The former is due to the fact that there is no symmetry missmatch between the modal field profile with the possible radiative plane wave routes. The latter effect is because the lower SLR detunes from the LSPR and approaches the (-1,0) RA as $k_{//}$ increases. The near- and far-field properties of the SLR modes are discussed in detail in the next section using a simple plane wave expansion model.

We observe that the Poynting vector becomes increasingly parallel to the plane of the array in the near field region as $k_{//}$ increases for both upper and lower SLRs (Figure 6.8). However, the Poynting vector of the lower SLR is anti-parallel to the direction of $k_{//}$. Therefore, it can be recognized that the upper and lower SLRs correspond to surface waves with counter-propagating group velocities (Poynting vectors have opposite directions) but parallel phase velocities (the wave vectors $k_{//}$ are parallel in Figure 6.8).

In order to investigate the different regimes observed in the eigenfield profile of Figure 6.8 in more detail, the relative radiative portion of the loss is numerically

calculated as

$$\gamma_{relative}^{rad} = \frac{\gamma_{rad}}{\gamma_{rad} + \gamma_{Ohmic}} \tag{6.3.1}$$

where $\gamma_{relative}^{rad}$ is the relative radiative loss portion, γ_{rad} is the radiative loss which is calculated by integrating the power leaving the nanorod arrays and γ_{Ohmic} is the Ohmic loss in the metal nanorods. In Figure 6.9a, we plot $\gamma_{relative}^{rad}$ of the upper SLR as a function of $k_{//}$ for three arrays with different nanorod widths. For every array $\gamma_{relative}^{rad}$ first decreases until a certain $k_{//}$ before suddenly increasing again to reach a maximum. The $k_{//}$ point where the sudden transition occurs is the point where an additional radiative loss channel starts to become available. This additional radiative loss channel is the outcoupling to the (-1,0) diffraction order plane waves that only becomes nonevanescent when the condition $|k_{//} - G_x| \leq nk_0$ is satisfied. This condition is satisfied at higher $k_{//}$ starting at the crossing point between the upper SLR with the RA (-1,0). The cusp $k_{//}$ point depends on the nanorod width, as changing the width shifts the upper SLR dispersion. After the minimum $\gamma_{relative}^{rad}$ increases rapidly with $k_{//}$ and reaches a maximum before slowly decreasing again. The radiative loss portion decreases again at high $k_{//}$ due to Ohmic loss becoming dominant as the upper SLR approaches the LSPR.

The radiative loss portion of the lower SLR is plotted as a function of $k_{//}$ in Figure 6.9b. $\gamma_{relative}^{rad}$ for the lower SLR is zero at $k_{//} = 0$ and it increases as $k_{//}$ increases. The slower increase of $\gamma_{relative}^{rad}$ at low $k_{//}$ for arrays with wider nanorods is due to the fact that there is a smaller detuning between the lower SLR and the LSPR which makes the SLR dispersion in the low $k_{//}$ regime flatter and its Ohmic loss more dominant.

6.4 Plane wave model for SLR profiles

This section demonstrates how a simple plane wave model, developed in collaboration with the Micro- and Nanophotonic Materials Group at the University of Mons, provides an intuitive basis for the near- and far-field properties of the calculated eigenmodes. Combined with the FEM simulations, a global picture of the field profile engineering possibilities is obtained.

The model gives a simple expression for the field in the uniform space above (or below) the nanorods. By exploiting the Bloch character of the eigenmode, we obtain

$$\psi(x,z) = \sum_m a_m e^{izk_z} e^{ix\left(k_{//}+mG_x\right)} \tag{6.4.1}$$

where the z-dependence stems from the uniform space in the z-direction [35]. Each integer order m corresponds to a particular propagation constant component along x ($k_x = k_{//} + mG_x$) and along z ($k_z = \sqrt{n^2k_0^2 - k_x^2}$). We neglect the vectorial character, the material loss component and the y-dependence. In addition,

we already obtain a characteristic picture of the modes by only considering three orders: $m = 0, +1, -1$. The eigenmode shapes are mainly determined by the particular orders that are present, by their symmetry, and by their radiative (k_z real, 'above the lightline', $|k_x| < nk_0$) or evanescent character (k_z imaginary, 'below the lightline', $|k_x| > nk_0$).

An estimate of the Fourier amplitudes a_0, a_{+1} and a_{-1} corresponding to each mode can be obtained from considering their basic characteristics. This is not an exact determination by calculation, as this would entail another simulation, as done in the previous section. However, it provides for insight into the underlying Bloch structure of what was rigorously calculated. Note that the dispersion (the values of k_0 and $k_{//}$) is considered as a given, determined by the eigenmode simulations (Figure 6.2b).

The simplest case is for the lower SLR, when $k_{//} = 0$. The anti-symmetry requires that $a_0 = 0$ and $a_{+1} = -a_{-1}$, so we are limited to only one option $(a_0, a_{+1}, a_{-1}) = (0, 1, -1)$. The resulting mode shape ($|\psi|$ in Figure 6.10a) is similar to the simulated one (Figure 6.6b, for *w* = 110 nm). At $k_{//} = 0$, the orders

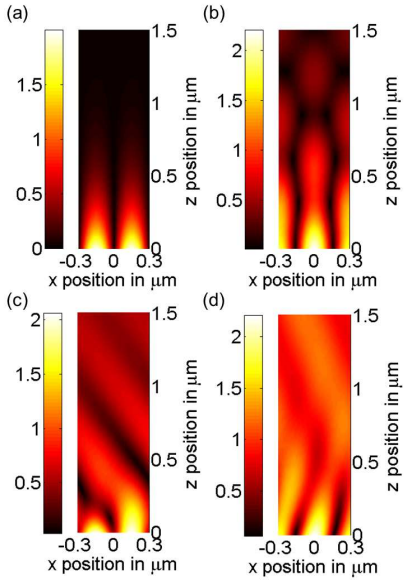

Figure 6.10: Plane wave model amplitude $|\psi|$ for: (a) Lower SLR ($k_{//} = 0$, $k_0 = 6.79$ rad/μm), (b) upper SLR ($k_{//} = 0$, $k_0 = 7.12$ rad/μm), (c) lower SLR ($k_{//} = 1.26$ rad/μm, $k_0 = 6.22$ rad/μm), (d) upper SLR ($k_{//} = 1.26$ rad/μm, $k_0 = 7.65$ rad/μm).

$+1$ and -1 are both evanescent along z. Additionally, as symmetry also requires the zeroth order to be absent, there is thus no coupling to radiation which makes the mode 'dark' and its far-field becomes zero for large z. For the upper SLR at

$k_{//} = 0$, the even symmetry requires $a_{+1} = a_{-1}$. The value of a_0 quantifies the radiative component, as again it is the only plane wave component above the lightline, but it also determines the strength of the central lobe compared to the side-lobes. We plot $|\psi|$ for a choice $(a_0, a_{+1}, a_{-1}) = (0.2, 1, 1)$ in Figure 6.10b, which we compare to the simulated profile (Figure 6.6a, for *w* = 110 nm). The near field shape with the larger central lobe is created by the non-zero a_0. In addition, this radiative order 0 provides for the 'bright' character of the mode, with non-zero magnitude in the far-field.

The situation becomes more complex for $k_{//} \neq 0$. For the lower SLR, for moderate $k_{//} > 0$, the modes $+1$ and -1 remain evanescent, as the dispersion curves downward. Therefore, as the mode becomes bright a non-zero a_0 is required. We choose $(a_0, a_{+1}, a_{-1}) = (0.5, 1, -1)$ in Figure 6.10c, to compare with Figure 6.8b, for $k_{//} = 1.26$ rad/μm with $k_0 = 6.22$ rad/μm. The interference between the three orders clearly recreates the characteristic simulated near field profile, with lobes going to the left (towards negative x) as z increases. In addition, a non-zero (but constant) amplitude is observed in the far-field, corresponding to radiation by order 0 in the $+x$-direction, which we also observe in the simulations (not visible on Figure 6.8b).

For the upper SLR there is a qualitative change of both the near- and far-field pattern as $k_{//}$ increases, as seen in the simulations (Figure 6.8a). In the plane wave picture this can be interpreted via a shift of the three orders with $k_{//} > 0$. We plot the *same* amplitudes $(a_0, a_{+1}, a_{-1}) = (0.2, 1, 1)$, but now for $k_{//} = 1.26$ rad/μm with $k_0 = 7.65$ rad/μm in Figure 6.10d, to compare with Figure 6.8a. The near field shows a bending of the lobes towards $+x$, in the opposite direction as the lower SLR. The far-field is again non-zero, but it has a non-constant profile, depending on x and z, unlike the constant value in the case of $k_{//} = 0$. This is a consequence of order -1 moving into the lightcone, leading to two radiative plane waves (order 0 and -1) interfering in the far-field with a non-evanescent lobe towards $-x$.

The plane wave model provides for a consistent picture of the simulated Bloch modes, and can be instrumental to interpret the near- and far-fields of SLRs. The knowledge of the field amplitude is crucial, for example for the interaction with localized emitters or absorbers.

6.5 Active liquid crystal tuning of hybrid plasmonic-photonic modes

In this section we discuss a demonstration of active liquid crystal (LC) tuning of hybrid plasmonic-photonic modes. More specifically, we demonstrate tuning of emission directionality and resonance wavelength of a hybrid plasmonic-photonic

mode arising from the coupling between an LSPR and a waveguide mode. This demonstration is done in a system of aluminum nanodisk arrays fabricated on top of an emitting layer consisting of colloidal semiconductor quantum dots (QDs), and then coated with LCs, which provide the active tuning. The tuning was achieved by changing the temperature of the sample, and relies on the fact that the orientation of the LCs becomes randomized and the medium becomes isotropic above a critical temperature T_c. Both variable angle extinction and photoluminescence were measured at temperatures well below and above T_c, where the effective refractive index changes from birefringent to isotropic. Numerical simulations utilizing the finite element method are used to elucidate the physics behind the tuning mechanism.

Though active tuning of plasmonic emission enhancement has been demonstrated, previous approaches mostly use localized surface plasmon resonances (LSPRs) or propagating surface plasmon polaritons. These approaches, which utilize pure plasmonic resonances, provide limited control over the directionality and spectral bandwidth of the emitted light. Hybrid plasmonic-photonic modes in periodic arrays of metallic nanoantennas however, can give a strong and actively tunable spectrally narrow emission enhancement without such limitations. These modes are in many ways superior for enhancing the emission of near field coupled sources [27–30, 36, 37]. Hybrid plasmonic-photonic modes can be flexibly designed via the geometry and dimensions of the structures [6, 33]. One can obtain a better field overlap with the region of interest and also better spectral overlap with the emission wavelength range. Actively tunable photon sources enhanced by such modes offer many possibilities for efficient applications in solid state lighting, lasers, and on-chip photon sources.

Figure 6.11 shows a sketch of the sample. CdSe/CdS/ZnS core-shell QDs with an average diameter of 6.5 nm were synthesized by the Physics and Chemistry and Nanostructures Group at Ghent University through the successive ion layer adsorption and reaction (SILAR) method [38]. These QDs are emitting around a central wavelength of 585 nm. The QDs were dispersed in toluene and spin-coated on a glass substrate, resulting in a 120 nm thick QD layer as determined by atomic force microscopy (AFM). A 15 nm thick protective silicon nitride layer was deposited on top of the QDs by plasma-enhanced chemical vapor deposition (PECVD) at relatively low temperature (120°C) to avoid degradation of the QDs. The deposited silicon nitride also planarizes the surface for consequent fabrication of the Al nanodisk array. Al nanodisk arrays were fabricated by Philips Research Laboratories with substrate conformal imprint lithography [39]. The nanodisks have a height of 150 ± 20 nm, a diameter of 120 ± 20 nm, and are arranged in a square lattice with nominal periodicity of 390 ± 10 nm. The Liquid Crystal and Photonics Group at Ghent University deposited LC molecules on top of the array. To control the orientation of the LC molecules a thin layer of nylon alignment

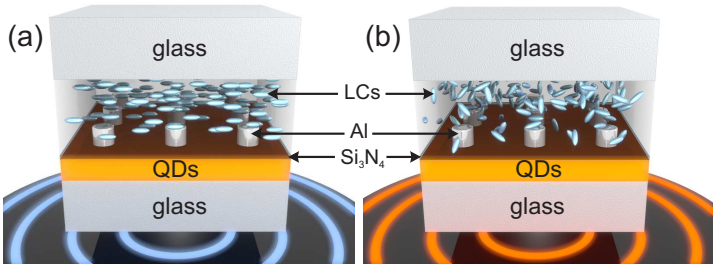

Figure 6.11: Schematic representation of the sample. (a) At room-temperature ($\sim 23^{\circ}C$) the liquid crystals are ordered, making the medium overlying the plasmonic nanostructures birefringent. (b) At higher temperatures ($> 58^{\circ}C$) the liquid crystals are disordered, yielding an isotropic refractive index in the same region.

material was placed over the array. The alignment layer was mechanically rubbed to force the LCs to orient in a planar direction along one of the lattice vectors of the square array. UV curable glue containing spacer balls with a diameter of 6 μm (not shown in Figure 6.11) is subsequently placed at the edge of the substrate away from the arrays and used to attach a glass plate to the sample. Finally, the space between the array and the top glass plate is filled with LC E7 (made by Merck) which has a critical temperature of 58°C [40].

We first discuss the extinction spectrum of the sample which gives a picture on the nature of the emergent hybrid plasmonic-photonic mode. The Surface Photonics Group in AMOLF measured the extinction spectrum of the sample at room temperature and above the LC critical temperature. A collimated beam (angular spread $< 0.1^{\circ}$) from a halogen lamp illuminates the sample with a linear polarization along the extraordinary index direction of the LC which is aligned with one of the lattice vectors of the square array. A fiber-coupled spectrometer measures the zeroth order transmittance T_0 in the far-field, for which the extinction follows as $1 - T_0$.

The extinction spectra at normal incidence for temperatures way below and above T_c is shown in Figure 6.12a. There we see two resonances pertaining to hybrid modes resulting from the interaction between the LSPR of each nanodisk with a waveguide mode resonance in the QD layer as will be clearly shown later. Upon increasing the temperature of the sample, the resonances in the extinction spectrum shift. The shift of the resonances is due to a transition of the liquid crystals from an ordered (Figure 6.11a) to a disordered (Figure 6.11b) state. This transition causes the LC medium to lose the birefringence character it has at room temperature in exchange for an isotropic refractive index. The observed shifts of the resonances were experimentally verified to be reversible upon successive heating and cooling of the sample.

To further show that the observed resonant wavelength shift is due to the LC

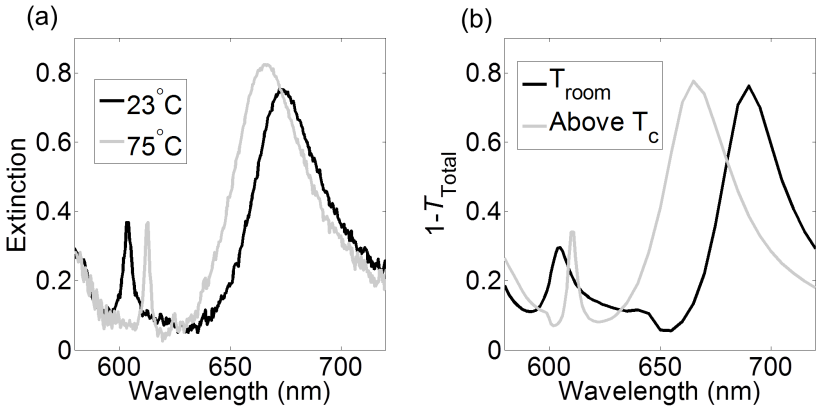

Figure 6.12: (a) Measured extinction spectra at normal incidence for temperatures below ($23^\circ C$) and above the LC critical temperature ($75^\circ C$). (b) Simulated $1 - T_{Total}$ spectra for perfect anisotropic and isotropic LC conditions which reflect the conditions below and above T_c respectively.

transition, we plot the extinction spectra at different temperatures in Figure 6.13. There we clearly see that a significant shift of both resonances occurs at 60°C which is just above the expected LC critical temperature of 58°C and not before. Thus, these measurements strongly indicate that the observed resonance shifts are tied to the LC phase transition. Another main point of interest in Figure 6.12a is the fact that the two extinction peaks spectrally shift in opposite directions. This shows that the LC phase transition affects the optical modes differently, indicating that in the birefringent state (at room temperature) they are each sensitive to different refractive indices as will be shown later.

To explain the observed temperature-dependent response, finite element simulations (COMSOL) of plane waves incident on the structure at normal incidence were performed. In the simulations the plane waves impinge from the LC layer which is considered to have infinite thickness above the array. At room-temperature T_{room}, we assume that the LC layer is perfectly ordered and aligned. Consequently, the LCs constitute a homogeneous anisotropic material with a weakly dispersive ordinary ($n_o \approx 1.52$) and extraordinary ($n_e \approx 1.73$) refractive index. Above T_c the LC layer is assumed to be completely isotropic with refractive index n_c which approximately follows the weighted average of the ordinary and extraordinary refractive indices $n_c \approx \frac{(2n_o+n_e)}{3}$. The frequency dependent LC refractive index data is taken from literature [40, 41]. The frequency-dependent refractive index of the glass, QD layer, and Al nanodisks were obtained by ellipsometry. On average throughout the measured wavelength range, the real part of the QD layer refractive index is around 1.79.

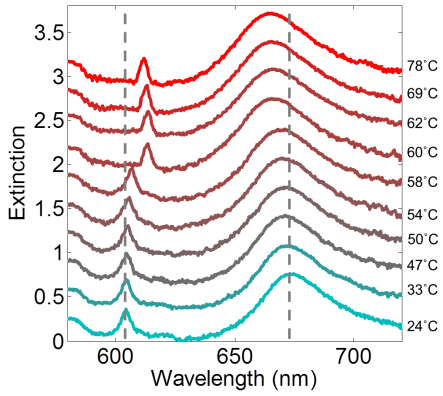

Figure 6.13: Normal incident extinction spectra at different temperatures measured by the Surface Photonics Group in AMOLF. The extinction spectrum at each temperature is displaced by 0.32 in the Y axis relative to its neighboring spectra.

Figure 6.12b shows the $1 - T_{\text{Total}}$ spectra where T_{Total} is the total transmittance obtained from the simulations. The simulated spectrum clearly reproduces the main experimental observations, displaying resonance wavelengths and shift directions in good agreement with experiments. The dimensions of the structure in the simulations were slightly different from the nominal values of the fabrication. Namely, for the simulations the lattice constant is 378 nm, and the particle height and diameter both are 100 nm. These deviations are attributed to uncertainties in the fabrication, which could have rendered structures with dimensions differing from the nominal ones. In addition, small discrepancies between the simulated and experimental refractive indices could also exert an influence on our results. Different values of the Al refractive index could be expected depending on the fabrication conditions.

To clarify the nature of the shorter wavelength resonance, which is our main interest, dispersion calculations were done without the presence of the nanodisk array in anisotropic and isotropic LC conditions (discussed later in relation to Figure 6.18). These calculations indicate that the array periodicity allows normal incident waves to couple to a fundamental Transverse Magnetic (TM) slab waveguide mode in the QD layer at wavelengths close to the measured resonance at 605 nm shown in Figure 6.12a. To further ascertain whether the shorter wavelength resonance has a waveguide mode nature, we perform normal incidence transmission simulations for a similar system but with a thicker QD film. Figure 6.14a shows the simulated 1-T_{Total} spectra for two different QD layer thicknesses (w_{QD}) at room temperatures. To show which resonant peak in the new thicker QD system pertains to the peak of interest, we plot the field enhancement profiles of the mode

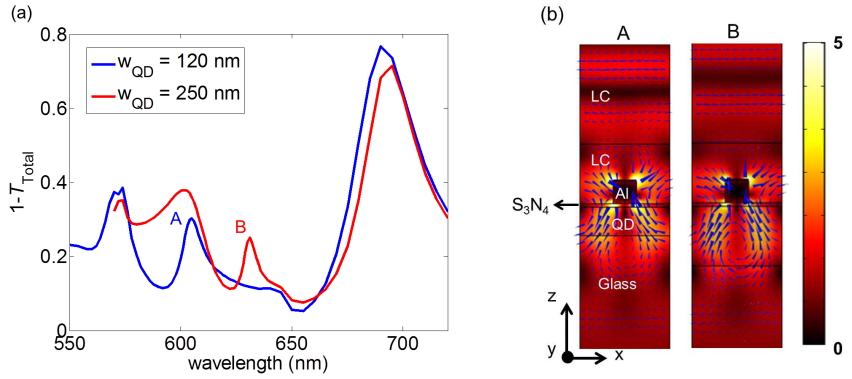

Figure 6.14: (a) Simulated extinction for QD layer thickness (w_{QD}) of 120 nm and 250 nm at room temperature T_{room} with LC optical axis oriented along x-direction. (b) Plot of field enhancement $|\boldsymbol{E}|/|\boldsymbol{E}_{input}|$ at the hybridized quasi-guided mode peaks for both w_{QD} (peak A and B in (a)). The blue cones show the electric field at a certain moment in time.

for both thicknesses in Figure 6.14b (peak A and B in (a)). There we can see that the two peaks have similar profiles and characteristics indicating that they stem from the same resonance phenomenon. More importantly we see that the peak redshifts when w_{QD} is increased. Such a shift can be expected from a waveguide mode resonance when the guiding core is made thicker. The redshift, dominant polarization, and near field enhancement of the mode strongly support the conclusion that these peaks arise from a coupling between a fundamental TM waveguide mode of the multilayer structure with the localized surface plasmon resonance of individual aluminum nanodisks. This coupling gives rise to the hybrid light-matter quasi-particles known as a waveguide-plasmon polaritons (WPP) as discussed in Refs. [26, 27]. Note that, by making the QD layer thicker, we are not changing the diffraction conditions set by the grating periodicity in the LC and glass substrate. This eliminates the possibility that the peak is a surface lattice resonance (SLR).

To examine the nature of the resonances in more detail, we plot cross-sections of the electric field enhancement $|\mathbf{E}|/|\mathbf{E}_{input}|$ through the middle of the nanodisk above T_c for the broad resonance at 665 nm and for the narrow resonance at 610 nm (Figure 6.12b), respectively in Figure 6.15a and 6.15b. In Figure 6.15a we observe that the electric field enhancements are most localized near the metallic nanostructure, resembling the characteristics of bare LSPRs. In contrast as seen in Figure 6.15b, the shorter wavelength resonance shows a more delocalized electric field enhancement distribution. This is characteristic of a waveguide mode close to cut-off (as it may be expected due to the small waveguide thickness and the asymmetry of the refractive index of the upper and lower media). Note, however, that the field enhancements are still relatively strong near the vicinity of the metallic nanodisks, indicating once more that waveguide-LSPR coupling is present.

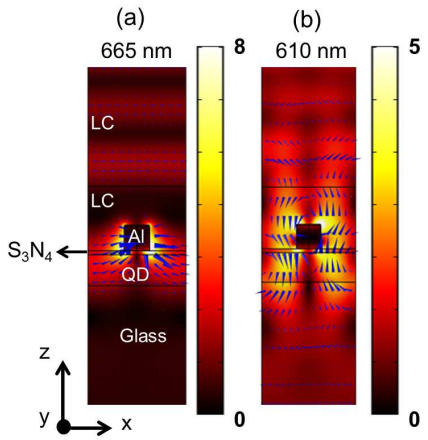

Figure 6.15: Total field enhancement for isotropic LC (above T_c) at wavelength (a) 665 nm (hybridized LSPR) and (b) 610 nm (hybridized quasi-guided mode). The incoming field is polarized along x. For all graphs, the blue arrows show the E field at a certain phase.

At zero waveguide-LSPR wavelength detuning, the arising hybrid states would consist of a linear superposition of the bare states with equal weights. In contrast, at large detuning the hybrid states resemble the bare states. Thus, although the LSPR and waveguide mode in our experiments are coupled, there is a large wavelength detuning between the resonances as compared to their linewidth. This makes the hybrid states resemble one or the other of the bare states. In particular, the broad resonance at long wavelengths is reminiscent of the LSPR, while the sharper resonance at short wavelengths is reminescent of a quasi-guided (leaky) mode. The mode is quasi-guided because it is radiative via coupling to the antennas. In view of these effects, the broad resonance is refered to as the hybridized LSPR and the narrow resonance as the hybridized quasi-guided mode, reserving the term waveguide-plasmon-polariton for the case where these hybrid states are tuned-in resonance [26, 27].

An interesting observation in Figure 6.15 concerns the dominant field components of each mode. The hybridized LSPR has a dominant in-plane electric field component with the same direction as the input plane wave polarization (x direction) which is along the extraordinary index direction of the LC (blue arrows Figure 6.15a). In contrast to that, the hybridized quasi-guided mode has a dominant z electric field component (out-of-plane blue arrows in Figure 6.15b), because the slab waveguide mode has TM polarization. Thus, this mode mainly samples the ordinary refractive index of the LC layer at T_{room}. Note that the relation between the LC refractive indices is $n_o < n_c < n_e$. Upon increase of temperature to above T_c, the quasi-guided mode thus experiences an increase of effective index,

as the LC layer index increases from n_o to n_c causing a red shift. In contrast, the hybridized LSPR mainly samples n_e in the LC layer at T_{room}, and therefore blue shifts when the temperature increases above T_c.

Having discussed the resonant wavelength tuning and modal field characteristics of the hybrid mode, we proceed to present the photoluminescence characteristics of our sample. The Surface Photonics Group in AMOLF measured the photoluminescence enhancement (PLE) of the sample at room temperature and above the LC critical temperature to demonstrate the active emission tuning. The QDs were pumped with a 450 nm laser beam at a fixed angle of incidence (5°) from the normal, and 0° azimutal angle. The emitted light at different directions was collected by the same fiber-coupled spectrometer used in extinction measurements. The PLE is defined as I_{in}/I_{out}, with I_{in} being the emission from the QDs in the presence of the nanodisk array, and I_{out} without the array. Figure 6.16a shows the PLE spectra in the direction normal to the sample. The wavelength range is limited by the emission bandwidth of the QDs, which only probes the hybridized quasi-guided mode. Up to 6 times directional light emission enhancement by the hybridized quasi-guided mode is observed in the PLE measurements at above T_c. As in extinction, the PLE feature due to this mode red shifts and its linewidth becomes narrower when the temperature is increased. Furthermore, the PLE is greater at higher temperatures. By fitting the PLE peak above T_c with the Fano-shape function (red dotted curve Figure 6.16a) we found a linewidth of 5.5 nm, which is very narrow for plasmonic systems. The Fano shape was used for the fitting as that is the expected spectral shape of modes arising from the coupling between a narrow (waveguide) resonance with a broad (LSPR) resonance [1–4]. This narrow PLE linewidth demonstrates the strength of hybrid plasmonic-photonic modes for emission enhancement purposes by providing a strong near field enhancement while having a low loss.

In order to understand the measured PLE characteristics we simulate the spectral dependence of the field enhancements in the QD layer. We define the electric field intensity enhancement in the QD layer by the nanodisk array with respect to the bare layer (without the array) as $I_E = \frac{[\int |E|^2_{\text{with array}} dV]_{QD}}{[\int |E|^2_{\text{without array}} dV]_{QD}}$, where the integral volume V extends throughout the QD layer volume within one period. While in the simulations I_E is a measure of the excitation strength of an optical mode, by reciprocity it also represents a decay strength of the same mode to outgoing plane waves in the same direction. Thus, I_E correlates with the PLE in experiments. Figure 6.16b shows I_E for a plane wave at normal incidence.

The calculated peak in I_E due to the hybridized quasi-guided mode reproduces the temperature dependence observed in our PLE experiments. This peak experiences a red shift and linewidth narrowing, and furthermore the enhancement also increases. We confirmed that this is related to the field confinement of the mode by performing eigenmode calculations to obtain its eigenfield profile at room temper-

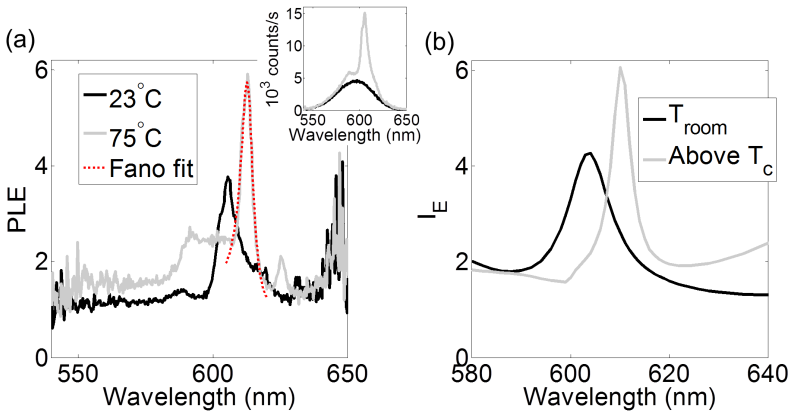

Figure 6.16: (a) Measured photoluminescence enhancement in the direction normal to the sample for temperatures below ($23^\circ C$) and above the LC critical temperature ($75^\circ C$). The red dotted curve is the Fano-shape fitting of the PLE peak in above T_c. The inset in (a) shows the photon count per second in the presence of the array (grey line) and without the array (black line) at $23^\circ C$. (b) Calculated integrated intensity enhancement in the QD layer I_E for perfect anisotropic and isotropic LC conditions obtained from simulations.

ature (T_{room}) and above LC critical temperature (T_c) conditions. In Figure 6.17b for the isotropic LC state above T_c, the hybrid quasi-guided mode is less confined to the aluminum nanodisks as compared to the anisotropic LC state at T_{room} (Figure 6.17a). Thus, above T_c, one expects the mode to have lower Ohmic losses. The weaker confinement results in less optical losses by the metallic structure, and is due to a lower index contrast between the QD layer and the isotropic LC layer above T_c. The damping constant of the mode (imaginary part of the eigenfrequency) obtained from these eigenmode calculations is 6.38×10^{12} Hz at T_{room} and 2.78×10^{12} Hz at above T_c, about a factor of two smaller. The eigenmode calculations are thus directly in accordance with the measured linewidth narrowing.

Finally we describe the directional dependence of both the extinction and PLE spectrum. Figure 6.18(a,b) shows the measured extinction at 23°C and 75°C respectively, while Figure 6.18(c,d) displays the PLE, for the same two temperatures. In all plots the bands of enhanced extinction/PLE correspond to the excitation of hybridized quasi-guided modes. The variable angle data shows a similar shift of this resonance in both extinction and PLE when temperature is increased to above T_c, as it occurs at normal incidence (Figure 6.12a and 6.16a). Thus, the entire band structure (in the measured range) is shifted. Consequently, the directionality of the emission enhancement provided by the hybridized quasi-guided mode can also be actively tuned by the LC.

Comparing Figure 6.18a with 6.18c, and 6.18b with 6.18d, one sees that the

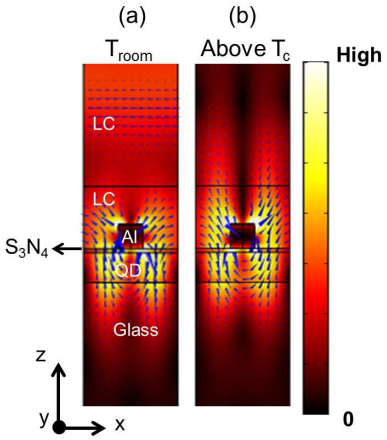

Figure 6.17: Eigenfield profiles of the hybridized quasi-guided mode at temperature of (a) T_{room} with LC optical axis oriented along x-direction and (b) above T_c. The color plot gives the $|\boldsymbol{E}|$ field profile with the same scale for both (a) and (b). The blue cones show the electric field at a certain moment in time.

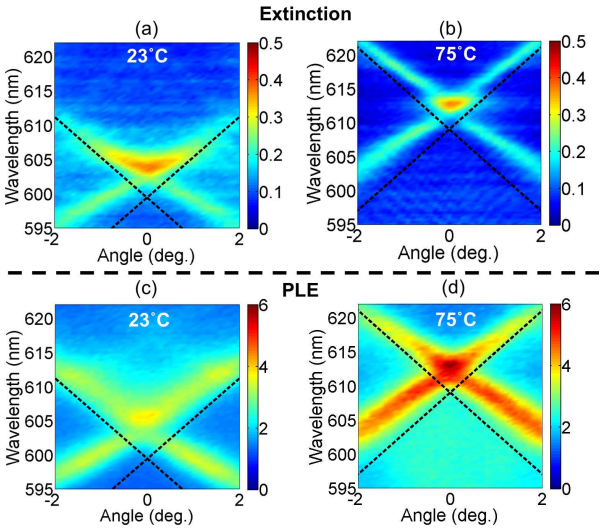

Figure 6.18: Measured extinction dispersion spectra at (a) $23^\circ C$ and (b) $75^\circ C$ (above T_c). Measured PLE dispersion spectra at (c) $23^\circ C$ and (d) $75^\circ C$ (above T_c). The black dashed lines in all the plots show the dispersion of the fundamental order TM waveguide mode without the presence of the Al nanodisk array at each temperature folded by the period of 378 nm.

dispersion of the hybridized quasi-guided mode in PLE closely resembles that in extinction. Furthermore, in all dispersion diagrams the hybrid quasi-guided mode closely follows the dispersion of the fundamental TM waveguide mode (folded into the first Brillouin zone) for the structure without the nanodisk array, indicated by the dashed lines. The proximity in wavelength of the hybrid quasi-guided mode to the bare waveguide mode suggests once more that the hybrid mode resembles the bare mode, and that the coupling to the LSPR has a small influence due to the large detuning between the modes. This is however not a detriment for our purpose of actively tuning the hybrid mode with the LC layer. In fact, the large out of plane fields of the bare TM polarized guided mode (and also of the coupled mode resembling the bare one) make it more sensitive to refractive index changes in the LC layer. Clearly, this allows for a greater degree of tunability given the fixed contrast between the ordinary and extraordinary refractive indices in the experiments.

6.6 Summary

This chapter discusses how the spectral properties of the interacting bare resonances influence the characteristics of a hybrid plasmonic-photonic mode. We demonstrate tailoring of SLR dispersion, linewidth, and associated stop-gap by controlling the energy detuning between the interacting bare resonances, which in this case are the LSPR and RAs. Here, we change the energy detuning by controling the LSPR spectral characteristics via a single geometrical parameter of the nanorods: their width. To ellucidate the physics behind the measurement results, numerical simulations were done for driven and undriven systems, with the latter revealing the SLR eigenmode properties for the first time. Both the radiative loss and the near field confinement (and thus Ohmic loss) of the SLRs are enhanced as the LSPR energy approaches the RA energy. The radiative component of the upper SLR, which is closer in energy to the LSPR, displays two regimes depending on in-plane momentum. In the low-momentum regime before crossing with the (-1,0) RA resonance, the upper SLR has only one radiation loss route. In the higher momentum regime, there are two radiation loss channels for the upper SLR due to the (-1,0) diffraction order entering the regime above the light line. This second radiation channel induces a cusp in the radiative loss portion and an optimum point at a nonzero $k_{//}$. In contrast, the lower SLR is simpler with always only one radiative channel, as it becomes less confined and more radiative as $k_{//}$ increases. Additionally, these properties are qualitatively interpreted with a plane wave model, explaining the evolution of the SLRs via the amplitude and radiative character of their Fourier components. With the plane wave model picture, the upper SLR field profile evolution can be qualitatively explained via a change in the radiative character of a Fourier component and thus corroborates the FEM analysis regarding the radiative loss routes.

We further proceed to demonstrate active LC tuning of the emission enhancement resonant wavelength and directionality provided by a hybrid plasmonic-photonic mode. This was demonstrated in a system of an aluminum nanodisk array that is placed on top of an emitting colloidal quantum dot layer and coated with LC. The hybrid mode in this system emerges from the coupling between localized surface plasmons of the aluminum nanodisk and waveguide modes in a quantum dot emitter layer. The LC layer refractive index depends on its molecular orientation, which is controlled here via temperature. Above a critical temperature, the LCs transition from an optically birefingent to an isotropic state. In turn, this modifies the resonance conditions for the hybrid mode and thus provides a tuning mechanism for the dispersion, linewidth, and excitation strength of the hybrid mode. Through numerical simulations, we show that the tuning mechanism depends on the field profile, more specifically on the orientation of the dominant mode polarization in the LC layer with respect to the LC axis. Up to 6 times directional light emission enhancement is demonstrated with a narrow linewidth of 5.5 nm. It is possible to further boost the tuning range and the enhancement factor by optimizing the optical mode field overlap with the LC and emitter layer.

In general, our results provide insight into how the hybrid plasmonic photonic mode depends on the interplay between the interacting bare resonances. The implications of various conditions on the near- and far-field characteristics of the hybrid mode are discussed. We envisage the work done here to be used as a stepping stone for utilizing hybrid plasmonic/photonic modes in diverse applications.

References

[1] B. Luk'yanchuk, N. I. Zheludev, S. A. Maier, N. J. Halas, P. Nordlander, H. Giessen, and C. T. Chong. *The Fano resonance in plasmonic nanostructures and metamaterials*. Nature Materials, 9(9):707–715, 2010.

[2] A. Lovera, B. Gallinet, P. Nordlander, and O. J. Martin. *Mechanisms of Fano Resonances in Coupled Plasmonic Systems*. ACS Nano, 7(5):4527–4536, 2013.

[3] Y. Francescato, V. Giannini, and S. A. Maier. *Plasmonic Systems Unveiled by Fano Resonances*. ACS Nano, 6(2):1830–1838, 2012.

[4] S. R. K. Rodriguez, A. Abass, B. Maes, O. T. A. Janssen, G. Vecchi, and J. Gómez Rivas. *Coupling Bright and Dark Plasmonic Lattice Resonances*. Physical Review X, 1:021019, 2011.

[5] S. Zou and G. C. Schatz. *Narrow plasmonic/photonic extinction and scattering line shapes for one and two dimensional silver nanoparticle arrays*. Journal of Chemical Physics, 121(24):12606–12612, 2004.

[6] E. M. Hicks, S. Zou, G. C. Schatz, K. G. Spears, R. P. Van Duyne, L. Gunnarsson, T. Rindzevicius, B. Kasemo, and M. Käll. *Controlling Plasmon Line Shapes through Diffractive Coupling in Linear Arrays of Cylindrical Nanoparticles Fabricated by Electron Beam Lithography*. Nano Letters, 5(6):1065–1070, 2005.

[7] F. J. García de Abajo and J. J. Sáenz. *Electromagnetic Surface Modes in Structured Perfect-Conductor Surfaces*. Physical Review Letters, 95:233901, 2005.

[8] F. J. García de Abajo. *Colloquium: Light scattering by particle and hole arrays*. Rev. Mod. Phys., 79(4):1267–1290, 2007.

[9] Y. Chu, E. Schonbrun, T. Yang, and K. B. Crozier. *Experimental observation of narrow surface plasmon resonances in gold nanoparticle arrays*. Applied Physics Letters, 93(18):181108, 2008.

[10] B. Auguié and W. L. Barnes. *Collective Resonances in Gold Nanoparticle Arrays*. Physical Review Letters, 101(14):143902, 2008.

[11] V. G. Kravets, F. Schedin, and A. N. Grigorenko. *Extremely Narrow Plasmon Resonances Based on Diffraction Coupling of Localized Plasmons in Arrays of Metallic Nanoparticles*. Physical Review Letters, 101(8):087403, 2008.

[12] G. Vecchi, V. Giannini, and J. Gómez Rivas. *Surface modes in plasmonic crystals induced by diffractive coupling of nanoantennas*. Physical Review B, 80(20):201401, 2009.

[13] W. Zhou and T. W. Odom. *Tunable subradiant lattice plasmons by out-of-plane dipolar interactions*. Nature Materials, 6:423–427, 2011.

[14] T. V. Teperik and A. Degiron. *Design strategies to tailor the narrow plasmon-photonic resonances in arrays of metallic nanoparticles*. Physical Review B, 86:245425, 2012.

[15] H. Lochbihler. *Surface polaritons on gold-wire gratings*. Physical Review B, 50:4795–4801, 1994.

[16] W. L. Barnes, T. W. Preist, S. C. Kitson, and J. R. Sambles. *Physical origin of photonic energy gaps in the propagation of surface plasmons on gratings*. Physical Review B, 54:6227–6244, 1996.

[17] S. C. Kitson, W. L. Barnes, and J. R. Sambles. *Full Photonic Band Gap for Surface Modes in the Visible*. Physical Review Letters, 77:2670–2673, 1996.

[18] A. Ghoshal, I. Divliansky, and P. G. Kik. *Experimental observation of mode-selective anticrossing in surface-plasmon-coupled metal nanoparticle arrays*. Applied Physics Letters, 94(17):171108, 2009.

[19] L. Martín-Moreno, F. J. García-Vidal, H. J. Lezec, K. M. Pellerin, T. Thio, J. B. Pendry, and T. W. Ebbesen. *Theory of Extraordinary Optical Transmission through Subwavelength Hole Arrays*. Physical Review Letters, 86:1114–1117, 2001.

[20] A. Krishnan, T. Thio, T. Kim, H. Lezec, T. Ebbesen, P. Wolff, J. Pendry, L. Martin-Moreno, and F. Garcia-Vidal. *Evanescently coupled resonance in surface plasmon enhanced transmission.* Optics Communications, 200(16):1 – 7, 2001.

[21] C. Sauvan, C. Billaudeau, S. Collin, N. Bardou, F. Pardo, J.-L. Pelouard, and P. Lalanne. *Surface plasmon coupling on metallic film perforated by two-dimensional rectangular hole array*. Applied Physics Letters, 92(1):011125, 2008.

[22] C. Billaudeau, S. Collin, C. Sauvan, N. Bardou, F. Pardo, and J.-L. Pelouard. *Angle-resolved transmission measurements through anisotropic two-dimensional plasmonic crystals*. Optics Leters, 33(2):165–167, 2008.

[23] C. Ropers, D. J. Park, G. Stibenz, G. Steinmeyer, J. Kim, D. S. Kim, and C. Lienau. *Femtosecond Light Transmission and Subradiant Damping in Plasmonic Crystals*. Physical Review Letters, 94(11):113901, 2005.

[24] K. G. Lee and Q.-H. Park. *Coupling of Surface Plasmon Polaritons and Light in Metallic Nanoslits*. Physical Review Letters, 95:103902, 2005.

[25] R. Taubert, D. Dregely, T. Stroucken, A. Christ, and H. Giessen. *Octave-wide photonic band gap in three-dimensional plasmonic Bragg structures and limitations of radiative coupling*. Nature Communications, 3, 2012.

[26] A. Christ, S. G. Tikhodeev, N. A. Gippius, J. Kuhl, and H. Giessen. *Waveguide-Plasmon Polaritons: Strong Coupling of Photonic and Electronic Resonances in a Metallic Photonic Crystal Slab*. Physical Review Letters, 91:183901, 2003.

[27] S. R. K. Rodriguez, S. Murai, M. A. Verschuuren, and J. G. Rivas. *Light-Emitting Waveguide-Plasmon Polaritons*. Physical Review Letters, 109:166803, 2012.

[28] G. Vecchi, V. Giannini, and J. Gómez Rivas. *Shaping the Fluorescent Emission by Lattice Resonances in Plasmonic Crystals of Nanoantennas*. Physical Review Letters, 102(14):146807, 2009.

[29] G. Lozano, D. J. Louwers, S. R.K. Rodriguez, S. Murai, O. T. Jansen, M. A. Verschuuren, and J. Gómez Rivas. *Plasmonics for solid-state lighting: enhanced excitation and directional emission of highly efficient light sources*. Light Science and Applications, 2:e66, 2013.

[30] W. Zhou, M. Dridi, J. Y. Suh, C. H. Kim, D. T. Co, M. R. Wasielewski, G. C. Schatz, and T. W. Odom. *Lasing action in strongly coupled plasmonic nanocavity arrays*. Nature Nanotechnology, 8:506–511, 2013.

[31] P. Offermans, M. C. Schaafsma, S. R. K. Rodriguez, Y. Zhang, M. Crego-Calama, S. H. Brongersma, and J. Gómez Rivas. *Universal Scaling of the Figure of Merit of Plasmonic Sensors*. ACS Nano, 5(6):5151–5157, 2011.

[32] S. A. Maier. *Plasmonics: Fundamentals and Applications*. Springer, New York, USA, 2007.

[33] A. Abass, S. R.-K. Rodriguez, J. Gómez Rivas, and B. Maes. *Tailoring Dispersion and Eigenfield Profiles of Plasmonic Surface Lattice Resonances*. ACS Photonics, 1(1):61–68, 2014.

[34] V. Giannini, G. Vecchi, and J. Gómez Rivas. *Lighting Up Multipolar Surface Plasmon Polaritons by Collective Resonances in Arrays of Nanoantennas*. Physical Review Letters, 105(20):266801, 2010.

[35] R. Engelen, D. Mori, T. Baba, and L. Kuipers. *Subwavelength structure of the evanescent field of an optical Bloch wave*. Physical Review Letters, 102(2), 2009.

[36] G. Pellegrini, G. Mattei, and P. Mazzoldi. *Nanoantenna Arrays for Large-Area Emission Enhancement*. Journal of Physical Chemistry C, 115(50):24662–24665, 2011.

[37] S. R. K. Rodriguez, G. Lozano, M. A. Verschuuren, R. Gómez, K. Lambert, B. D. Geyter, A. Hassinen, D. V. Thourhout, Z. Hens, and J. G. Rivas. *Quantum rod emission coupled to plasmonic lattice resonances: A collective directional source of polarized light*. Applied Physics Letters, 100(11):111103, 2012.

[38] J. J. Li, Y. A. Wang, W. Guo, J. C. Keay, T. D. Mishima, M. B. Johnson, and X. Peng. *Large-Scale Synthesis of Nearly Monodisperse CdSe/CdS Core/Shell Nanocrystals Using Air-Stable Reagents via Successive Ion Layer Adsorption and Reaction*. Journal of American Chemical Society, 125(41):12567–12575, 2003.

[39] M. A. Verschuuren. *Substrate Conformal Imprint Lithography for Nanophotonics*. PhD dissertation, Utrecht University, 2010.

[40] J. Li, C.-H. Wen, S. Gauza, R. Lu, and S.-T. Wu. *Refractive Indices of Liquid Crystals for Display Applications*. Journal of Display Technology, 1(1):51, 2005.

[41] J. Li, S.-T. Wu, S. Brugioni, R. Meucci, and S. Faetti. *Infrared refractive indices of liquid crystals*. Journal of Applied Physics, 97(7):073501, 2005.

7

Electrical properties of thin-film polycrystalline silicon cells

7.1 Introduction

Thin-film polycrystalline silicon (poly-Si) solar cells have much promise as an economical alternative to multi-crystalline, wafer based cells. However, structural deficiencies still limit the performance of these poly-Si cells [1–3]. The presence of intra-grain defects, grain boundary defects and impurities can severely limit the performance of poly-Si solar cells, as compared to their more expensive mono- or multi-crystalline counterparts. The intra-grain defects in poly-Si films are difficult to avoid and they can act as traps and effective carrier recombination sites [4–7].

Recently, it has been shown that poly-Si films fabricated with the Laser Induced Crystallization (LIC) method have a low intra-grain defect concentration though at the expense of having a homogeneous distribution of small grains [8–10]. Unfortunately, a polycrystalline film with small grains would have a lot of grain boundaries which can also act as effective recombination sites of the charge carriers, or could gather impurities [4, 11–14]. Grain boundaries in poly-Si, in particular, cannot be perfectly passivated. To alleviate the problems with grain boundaries, much research and development has been focused on fabrication methods that could achieve larger grains, and hence less grain boundaries.

One such fabrication method that can produce large grains is the Aluminium Induced Crystallization (AIC) method. However at present, there is still much to be desired from the AIC method as it currently leads to a significant density

of intra-grain defects [4, 5]. Additionally, the AIC also tends to result in a large variance of grain sizes [1, 5, 15, 16]; typically the larger the grains produced, the larger the grain size variance in a film [15]. Smaller grains will have a lower local open circuit voltage V_{oc} (this concept will be explained later on in section 7.3) compared to the larger grains, due to the fact that charge carriers easily meet the grain boundaries and recombine there [17, 18]. In an assembly of grains of different sizes, there are concerns that the smaller grains may instead be taking away current from the larger grains instead of contributing to the power generation; this is so because the grains can be thought as connected in parallel with each other (see section 7.3).

In the efforts to select and optimize a fabrication method to produce poly-Si thin-film solar cells with the best performance, targets and guidelines of acceptable film quality are highly desired. We thus study in this chapter poly-Si cells with varying intra-grain diffusion length and grain size distribution, under various conditions through numerical simulations. In particular, we consider also the effect of other parameters such as thickness, doping density, and grain boundary recombination velocity. These calculations show the necessary carrier diffusion length one needs to achieve in order to obtain the desired cell performance and the effect of grain size on the performance of the cell.

In the calculations to obtain the diffusion length and grain size guidelines, we specifically focus on a pn junction solar cell consisting of a stack of planar layers (Figure 7.1): a metal back contact, a p^+ back surface layer which is inherent when AIC is used [2, 19], an extra 0.2-0.5 μm p^+ layer grown on top of it, a p-base with variable thickness, and a thin n^+-emitter. When the emitter is in-diffused, a finger contact is applied directly, but when the emitter consists of a very thin amorphous i/n^+ layer (thus when the cell is a hetero junction with intrinsic thin layer (HIT cell)), an ITO layer is inserted between the emitter and the finger contact.

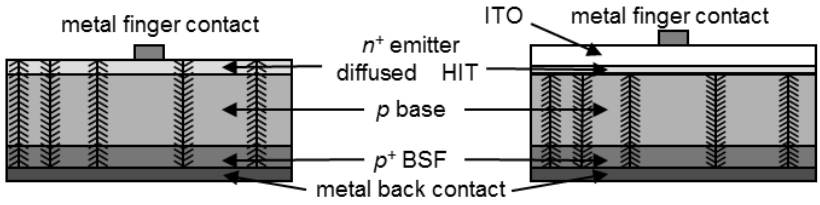

Figure 7.1: Schematic representation of the p^+-p-n^+ solar cell structures studied: with an in-diffused emitter (left) or with a HIT emitter (right). Columnar grains with vertical boundaries are schematically indicated.

The poly-Si film is assumed to only consists of columnar grains with vertical boundaries, as sketched in Figure 7.1. Modern thin-film polycrystalline fabrication methods are able to achieve such grain formation, at least approximately [5, 20–

22]. Our assumption on the vertical grain boundaries leads to a simplified model of the current distribution in the cell: the current is vertical, thus parallel to the grain boundaries, in the base layer and HIT emitter if present, and becomes two-dimensional in the diffused n^+ emitter or ITO layer to be collected in a finger contact. A possible 2D character of the current within a grain will be accounted for by introducing an effective diffusion length that considers recombination at the grain boundaries. It is however additionally assumed that no current crosses the grain boundaries, which is not valid when the doping is extremely high.

To obtain a complete picture of the effects of different parameters, we simulated poly-Si cells for two different cases. (i) First we model cells with homogeneous grain properties by direct analytical solution of the transport equations in section 7.2. (ii) We model a parallel assembly of grains with an inhomogeneous size distribution by setting up and solving an electrical equivalent circuit in section 7.3.

After discussing the general guidelines of the carrier diffusion length and grain size distribution for thin poly-Si cells, we proceed to investigate the comparison between n^+p and p^+n cells in the efforts to ascertain the best doping type for the absorber layers in section 7.4. Traditionally, thin-film pn junction poly-Si cells are made with a p-type absorber layer and thus with electrons as minority carriers in the absorber. It is not evident however, whether cells with a p-type absorber would be better than cells with an n-type absorber. Though the mobility of electrons is larger than that of holes, the nature of the defects, which may facilitate the recombination mechanisms, in the two different absorber layers may be different. How each layer type reacts to defect passivation processes may also be different. To elucidate the potential performance of the two layer types, we show C-V and admittance spectroscopy measurement results of thin-film poly-Si cells with both p-type and n-type absorbers made in IMEC. These measurements enable us to deduce the apparent doping density and defect concentration-energetical distribution of these samples.

Most of the work in this chapter was presented in our paper in Ref. [23]. The work here is done in a collaboration between IMEC, the Micro- and Nanophotonic Materials Group at the University of Mons, and the Solar Cells Group at Ghent University.

Section 7.2 describes simulation results of poly-Si cells with homogeneous grain properties under various conditions. We continue to discuss the effect of grain size inhomogeneity on the cell's performance in section 7.3. Section 7.4 presents the characteristic differences between cells with p-type and n-type absorber layers that is observed in the capacitance measurements. Section 7.5 gives the summary of the chapter.

7.2 Poly-Si solar cells with homogeneous grains

Here we simulate a hypothetical cell consisting of one single grain, which is equivalent to the case of a cell with multiple grains of the same size with homogeneous properties assuming perfectly conducting contacts. Such homogenous grain distribution and characteristics is approximately the case for fabrication methods such as LIC in which the grain diameter variance is small. From this simulation of a homogeneous cell, we will obtain an idea of the intra-grain material properties necessary to achieve a desired efficiency of poly-Si cells with homogeneous grain properties. These results will also be the starting point of our calculation of inhomogeneous grain systems (section 7.3).

7.2.1 Dark current and effective diffusion lengths

The thin-film poly-Si cells considered here are modeled using an extended Shockley model which describes the effect of bulk and space charge layer (SCL) region recombination. The total current J in the cell is assumed to follow the expression:

$$J = J_{01}\left(\exp\left(\frac{qV}{1kT}\right) - 1\right) + J_{02}\left(\exp\left(\frac{qV}{2kT}\right) - 1\right) - J_L \qquad (7.2.1)$$

Here V is the voltage, k is the Boltzmann constant and q the elementary charge, J_{sc} is the short circuit current, J_{01} and J_{02} are the dark diode saturation currents: J_{01} models recombination in the quasi-neutral regions and J_{02} models the recombination in the SCL. The diode saturation currents are described by:

$$J_{01} = \frac{qDn_i^2}{N_d}\frac{1}{L_{poly}} \qquad (7.2.2)$$

$$J_{02} = \frac{q\pi Dn_i V_t}{F_{max}}\frac{1}{L^2} \qquad (7.2.3)$$

with n_i the intrinsic carrier concentration, N_A, D and L are the acceptor doping density, the minority carrier diffusion constant and diffusion length respectively; and F_{max} is the maximum electric field in the SCL. L_{poly} is the effective diffusion length which takes into account grain boundary recombination as mentioned in chapter 3 section 3.5 through the expression [13]:

$$L_{poly} = \frac{L_{mono}}{\sqrt{1 + \frac{2S_{GB}L_{mono}^2}{Dg}}} \qquad (7.2.4)$$

where S_{GB} is the recombination velocity at the grain boundaries and g is the diameter of the grain. L_{mono} is the effective diffusion length which takes into account

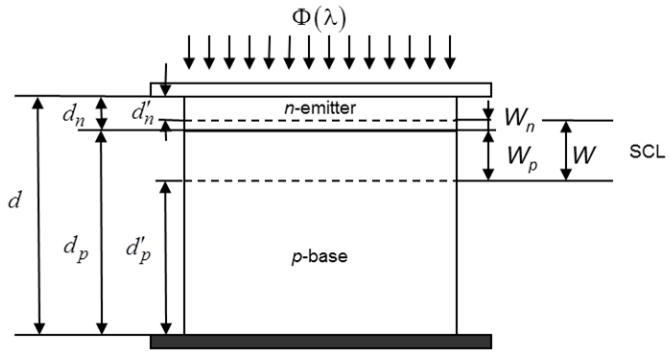

Figure 7.2: Thickness definitions: the total thickness d is divided over emitter thickness d_n and base thickness d_p, with $d = d_n + d_p$. The base is divided over the space charge layer W_p and the neutral base thickness d'_p, with $d_p = W_p + d'_p$, similarly for the emitter, with $d_n = W_n + d'_n$. The total Space Charge Layer (SCL) thickness is $W = W_p + W_n$.

the effects of finite thickness and contact recombination velocity on the spatial distribution of charge carriers. The expression for L_{mono} is restated here [13, 24]:

$$L_{mono} = L\frac{\cosh\left(\frac{d'}{L}\right) + \frac{SL}{D}\sinh\left(\frac{d'}{L}\right)}{\sinh\left(\frac{d'}{L}\right) + \frac{SL}{D}\cosh\left(\frac{d'}{L}\right)} \tag{7.2.5}$$

where d' is the width of the quasi-neutral region as shown in Figure 7.2, D is the diffusion coefficient, L is the diffusion length, and S is the recombination velocity at the contacts.

In describing the effect of intra-grain defects, one can use either of the two diffusion lengths L or L_{mono}. L is a material property, not depending on thickness or surface conditions. However, L_{mono} is more easily obtained from measurements of thin-film cell samples, as done e.g. by Taretto et al. [14], and hence L_{mono} can be a more convenient choice in practice. There are examples of both choices in this work.

In what follows we will utilize the notation L_b and S_b, to emphasize that these are properties of the minority carriers in the base. Although the analytical expressions for J_{01} and L_{mono} assume a simple pn junction solar cell, they can also be used for a p^+pn cell with a p^+ back surface layer by an effective low value S_b at the p^+/p interface instead of the physical high value of S_b at the real contact [24].

As the SCL width is much smaller than the thickness of the quasi-neutral layers, any grain boundary recombination in the space charge layer is neglected. Hence the diffusion length L appearing in (7.2.3) is the bulk minority carrier diffusion length, uncorrected for the effects of contact recombination (not relevant here) and grain boundary recombination (neglected).

7.2.2 Light current

In this homogeneous case, we assume that there is no finger contact, but that the front layer (the diffused n+ emitter or the ITO layer) is fully transparent and has zero resistance. Also, we assume that the light has a double pass through the cell and that the back contact has an internal reflection coefficient R. In a real cell, especially when light trapping is present, the number of effective passes of light in the cell can be substantially higher than two; our treatment will thus give a lower estimate of the light current. The carrier generation $G(\lambda, x)$ is then given by:

$$G(\lambda, x) = \Phi(\lambda)\alpha(\lambda)\left[\exp\left(\alpha\left(\lambda\right)x\right) + R\exp\left(-\alpha\left(\lambda\right)\left(2d - x\right)\right)\right] \qquad (7.2.6)$$

where λ is the wavelength, $\Phi(\lambda)$ is the number of incident photons per area, per time and per unit wavelength bandwidth, α is the absorption coefficient, x is the position in the cell with $x = 0$ being the position of the front interface of the cell, and d is the total thickness of the cell (see Figure 7.2). For the case of multiple passes without considering interference effects, (7.2.6) would be multiplied by a factor of $\frac{T}{1-RR_f\exp(-\alpha(\lambda)2d)}$ where T and R_f are the front side transmittance and internal reflectance respectively. The effect of this factor would mainly change the magnitude of the light current without affecting much the trends in the results presented below.

In the homogeneous grain case, we solve the diffusion equation for the current transport using a standard formulation such as in Sze [25], but modified for the double pass light trajectory.

7.2.3 Input parameters

The absorption coefficient $\alpha(\lambda)$ for silicon is taken from Adachi [26] and is almost identical with that of Green [27]. For the incoming light spectrum $\Phi(\lambda)$ we use the standard AM1.5G spectrum [28]. The geometrical and electronic parameters of the emitter and base are listed in Table 7.1.

These parameters relevant for the AIC poly-Si cells are taken from Van Gestel et al. [5] when available and data for crystalline Si are used if not [27, 29]. In our calculations we did not vary the emitter parameters in order to focus only on the minority carrier effects in the base layer. The emitter thickness is a trade-off between low lateral resistance (requiring high d_n) and low collection loss due to the low value of L_p in the highly doped emitter (requiring low d_n). We further assumed a low value of the surface recombination S_p at the emitter surface, also to concentrate on the influence of the base material. We only take into account the effect of the p^+ back surface layer by assuming a low effective back contact recombination velocity at the p^+/p interface. We neglect any other effects in the p^+ layer, such as optical absorption generating electron hole pairs and free carrier absorption, to keep the analytical model more manageable with less input parameters

property	symbol	unit	n-emitter	p-base
thickness	d	μm	0.5	3 & varied
doping density	N_A or N_D	cm^{-3}	10^{19}	10^{16} & varied
minority carrier diffusion length	L	μm	1	varying
mobility at low doping density	μ_{max}	cm^2/Vs	473	1448
mobility at high doping density	μ_{min}	cm^2/Vs	47.7	55.24
reference doping density	N_{ref}	cm^{-3}	6.3 10^{16}	1.1 10^{17}
exponent	β	-	0.711	0.733
contact recombination velocity	S	cm/s	10^3	10^3
grain size (diameter)	g	mm		0.1 - 100
grain boundary recombination velocity	S_{GB}	cm/s		10^3 - 10^5

Table 7.1: Input parameters for the simulations

to focus on. The space charge layer widths W_n and W_p follow from the doping density and the standard abrupt depletion theory. From the geometrical emitter and base thickness d_n and d_p, the quasi-neutral thicknesses d'_n and d'_p are then found. We assume that the minority carrier mobilities depend on doping density as for crystalline silicon [29–31]:

$$\mu = \mu_{min} + \frac{\mu_{max} - \mu_{min}}{1 + \left[\frac{N}{N_{ref}}\right]^{\beta}} \tag{7.2.7}$$

with the values of μ_{max}, μ_{min}, N_{ref}, β that are used listed in Table 7.1. The diffusion constants then follow from the mobilities and Einstein's relation $D = (kT/q)\mu$. The expected grain boundary recombination velocity S_{GB} for polycrystalline silicon cells can be in the range 5×10^3 - 5×10^4 cm/s [32–35], and the grain size distribution extends from below 1 μm to about 50 μm in AIC poly-Si cells [4]. These ranges are covered in our simulations (Table 7.1).

7.2.4 Dependence of solar cell parameters on poly-Si grain properties

The calculation results presented here provide guidelines and rules of thumb for cell thickness, carrier diffusion length, grain size and the grain boundary recombination velocity that are needed to achieve a desired performance. In Figure 7.3, we plot the solar cell efficiency as a function of base thickness for different values of the base intra-grain diffusion length L_b, grain size g and grain boundary recombination velocity S_{GB}. To reflect different conditions of intra-grain quality, we varied the minority carrier diffusion length L_b in the base layer, instead of the effective value L_{mono}, as the variation of d_p also changes L_{mono} through (7.2.5). It is clear from Figure 7.3 that the diffusion length determines the thickness at which a maximum value of efficiency is reached. In most of the graphs of Figure 7.3,

we see that when the base thickness d_p exceeds its optimal value, the efficiency decreases slightly and then levels off. However, this saturation is not seen for the top blue circles plot as L_b is larger than the d_p range being considered in the graph. This is to be expected in the cells under study, which mainly depend on diffusion to harvest the charge carriers, due to the fact that substantial absorption occurs outside the space charge layer. Beyond a certain thickness, which scales with the diffusion length, the charge carriers generated deep in the base layer cannot reach the junction or the contact, thus the deep or even the middle part of the base thickness becomes useless. The red plot in Figure 7.3 is for the case of $L_b = 5.5$ μm and with infinite grain size $g \to \infty$ or perfectly passivated grain boundaries $S_{GB} = 0$. This red plot gives an idea of the minimal intra-grain film quality (thus L_b) needed to achieve a 10% efficiency in the system under consideration. This necessary value of L_b of course depends on the doping and geometry parameters used here.

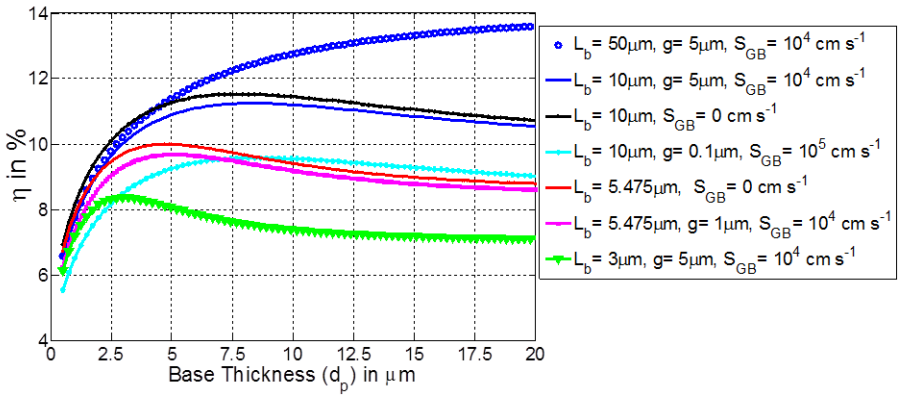

Figure 7.3: Efficiency versus base thickness for different conditions of the base diffusion length L_b, the grain size g and the grain boundary velocity S_{GB}. The other parameters are taken from Table 7.1. For each base thickness d_p, the appropriate value of L_{mono} is calculated with (7.2.5).

Comparing the three plots with $L_b = 10$ μm with each other, we see that the grain boundary recombination mainly shifts the graph vertically, having little effect on the optimum value of the thickness. In the very pessimistic case where the grain diameter g is only 0.1 μm and the grain boundary recombination velocity S_{GB} = 10^5 cm/s is high (cyan curve in Figure 7.3), we see that the grain boundaries cause an efficiency loss of about 2% absolute compared to the case of perfectly passivated grain boundaries (the black curve in Figure 7.3). Note that by comparing the blue and black curve in Figure 7.3, it is seen that there is only an increase of less than 0.5% in efficiency in the thickness regime considered when we enlarge the grain diameter beyond 5 μm. Having grain diameters around this range of sev-

eral μms is thus sufficient for the thickness regime of interest considering common grain boundary recombination parameters.

Similar efficiency loss however can also be caused by reducing the diffusion length from 10 μm to about 5 μm, whilst maintaining perfectly passivated grains (either $g \to \infty$ or S_{GB} = 0): compare the cyan and the red curve in Figure 7.3. It is reported that modern fabrication methods nowadays can avoid such an extreme case of grain diameter g = 0.1 μm and grain boundary recombination velocity S_{GB} = 10^5 cm/s [32-34]. We thus take this grain size and recombination velocity as the worst case and not consider worse circumstances. It is also seen that a decrease of diffusion length from 5.475 μm to 3 μm would still give a significantly lower efficiency performance as we compare the red plot with the green plot in Figure 7.3. However, a value of L_{mono} as low as 1.5 μm due to intra-grain defects has been reported [4]. This indicates the fact that significant attention should be dedicated in decreasing or passivating the intra-grain defects.

Figure 7.4 shows the dependence of open circuit voltage V_{oc} on the effective diffusion length L_{mono} of the base layer for different grain diameters. When $L_{mono} < 3 - 5$ μm, V_{oc} is determined by L_{mono} and is almost independent of the grain size. This holds for a wide range of grain sizes 1 μm $< g <$ 100 μm. This g-range is commonly found in polycrystalline films made with AIC although the grain size is not homogeneous in such films. We expect that the efficiency of AIC poly-Si cells will be limited by the intra-grain diffusion length and not by the grain size or its distribution, as long as $L_{mono} < 3 - 5$ μm. On the other hand, when the intra-grain diffusion length is high, leading to $L_{mono} > 5$ μm, the grain diameter distribution effect would be more pronounced, showing a V_{oc} loss of 60 mV when going from large 100 μm grains to small 1 μm grains. This preliminary conclusion will be confirmed in Section 7.3 on inhomogeneous systems. Figure 7.4 is also relevant for the influence of the grain boundary recombination velocity S_{GB}, since the solar cell behavior actually depends on the g/S_{GB} ratio as is obvious from (7.2.4). We can also see in Figure 7.4 that there is a saturation effect of achievable V_{oc} as we increase L_{mono} depending on the grain size. Although charge carriers can move freely within the grain when L_{mono} is high, the possibility of them recombining at grain boundaries may be significant in sufficiently small grains. Thus, grain size can limit cell performance when L_{mono} is high.

As already mentioned, L_{mono} is an effective value lumping the effects of intra-grain bulk recombination (described by L_b) and surface recombination at the base contact S_b. It follows from (7.2.5) that changing the base thickness d_p keeping the intra-grain quality (L_b and S_b) constant will affect L_{mono}. The effect of varying the base thickness for various combinations of g and L_b, but with constant S_b and S_{GB} is shown in Figure 7.5. The influence of L_b is more apparent when d_p is larger than L_b but the extent to which L_b can influence the V_{oc} at a certain device

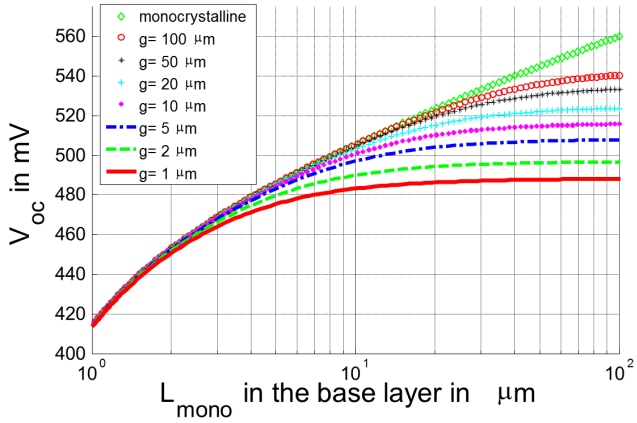

Figure 7.4: Open circuit voltage V_{oc} vs. effective diffusion length L_{mono} for different grain diameters. The base thickness is d_p = 3 μm and the grain boundary recombination velocity S_{GB} = 10^4 cm/s.

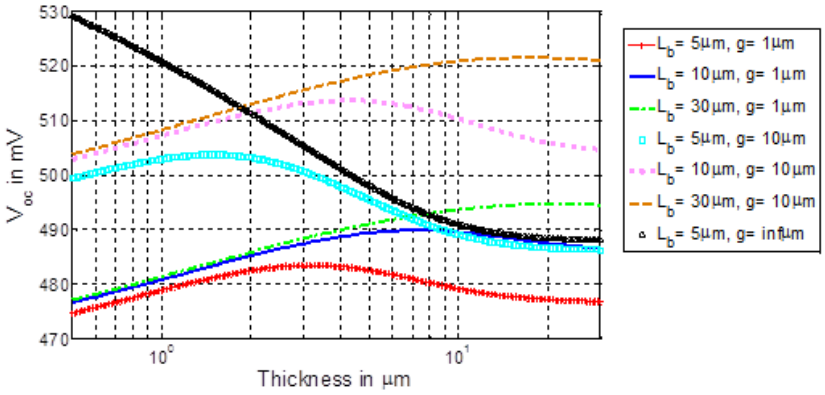

Figure 7.5: Open circuit voltage V_{oc} vs. base thickness d_p for various combinations of grain size g and base diffusion length L_b. $S_{GB} = 10^4$ cm/s and $S_b = 10^3$cm/s.

thickness is still determined by the grain boundary recombination (compare e.g. the three curves of g = 1μm and g = 10μm). It can be seen in Figure 7.5 that L_b affects the V_{oc} more when both d_p and g are larger. At thin cells with $d_p < 5$ μm, V_{oc} is heavily affected by the grain boundaries and having grains with g beyond 10 μm can still help. This is to be expected as the parameters of Figure 7.5 leads to $SL/D \ll 1$ which, according to (7.2.5), implies that L_{mono} increases with decreasing base thickness for the same L_b. Thus, the results of Figure 7.5 for a thin base should correspond to the result of Figure 7.4 for high L_{mono}; indeed, in

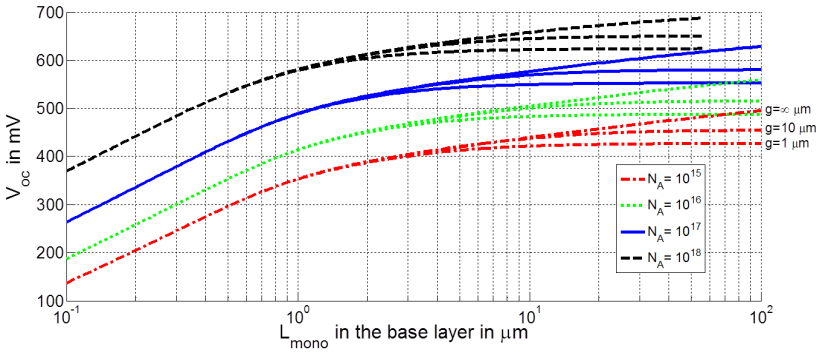

Figure 7.6: Open circuit voltage V_{oc} vs. effective diffusion length L_{mono} in the base. The parameters are the doping density N_A in the base layer and the grain diameter g. The base thickness d_p = 3 μm and the grain boundary recombination velocity is S_{GB} = 10^4 cm/s. The upper curve of each colour (N_A value) corresponds to an infinite grain size $g \to \infty$, the middle one to g = 10 μm and the lower one to g = 1 μm.

both cases the influence of grain size on V_{oc} is manifested.

The doping density N_A of the base is also an important design parameter. Increasing N_A results in an increase of built-in voltage and hence of V_{oc}. However, increasing N_A also decreases L_b, both by decreasing the mobility according to (7.2.7) and by decreasing the minority carrier life time τ_n due to Auger recombination and possible introduction of additional defects. An appropriate value of N_A should consider the trade-offs due to these effects. The Auger processes start to dominate the recombination for high $N_A > 5 \times 10^{17}$ cm^{-3} [31]. We therefore show V_{oc} vs. L_{mono} in Figure 7.6 for different doping densities N_A in the base layer. In these graphs the dependence of mobility on doping density of (7.2.7), and the relation (7.2.5) between L_b and L_{mono} are taken into account. It should be noted that it is in practice much more difficult to reach a high L_b and thus L_{mono} value when the doping density is high.

To get a first estimate of how harmful an inhomogeneous distribution of grain sizes g could be in a real polycrystalline poly-Si cell, we normalize the cell efficiency $\eta(g)$ of a homogeneous cell with grain size g to the efficiency $\eta(50\mu\text{m})$ of a homogeneous cell with g = 50 μm. In other words, we are comparing the generated power per unit area of these cells. The value of 50 μm represents a fairly large grain diameter that would be present in a typical AIC layer.

$$\eta_{rel,50}(g) = \frac{\eta(g)}{\eta(50\mu\text{m})} \tag{7.2.8}$$

In Figure 7.7 we plot $\eta_{rel,50}(g)$ and the voltage at the maximum power point $V_{mpp}(g)$ for a homogeneous cell with base thickness d_p = 3μm and grain boundary recombination velocity S_{GB} = 10^4 or 10^5 cm/s for different L_{mono} as indicated in

the legend. We see in Figure 7.7, that when $L_{mono} \geq 50$ μm and $S_{GB} = 10^4$ cm/s, a grain with $g = 0.5$ μm is producing only about 8% less power (Figure 7.7a) than a grain of 50 μm diameter, and has a V_{mpp} value that is only 40 mV lower (Figure 7.7b). When L_{mono} = 100μm and the grain boundary recombination velocity is an order of magnitude higher, thus $S_{GB} = 10^5$ cm/s, we see that the $g = 0.5$ μm cell is producing only 11% less power than the $g = 50\mu$m cell, and that its maximum power voltage is only around 50 mV lower.

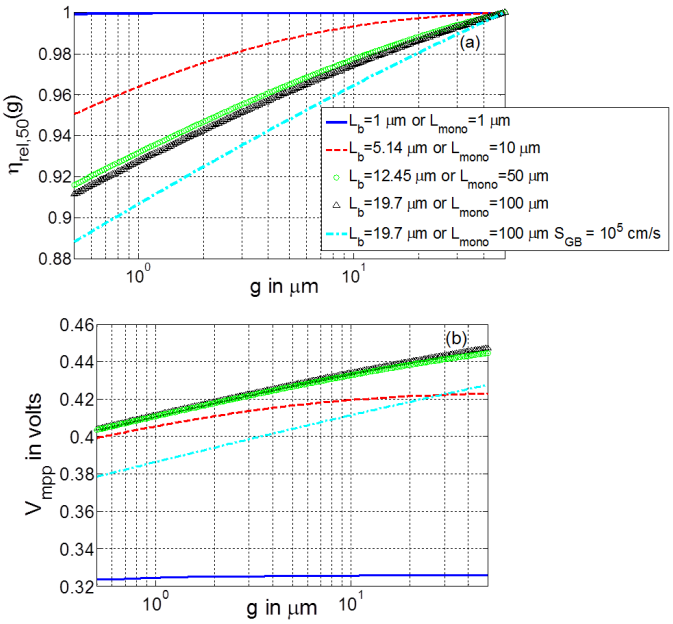

Figure 7.7: (a) Efficiency η of a homogeneous cell with grain diameter g, normalised to a homogeneous cell with g = 50 μm. (b) Maximum power voltage V_{mpp} vs. grain diameter g in a homogeneous cell. We used $S_{GB} = 10^4$ cm/s unless stated otherwise in the legend, base thickness d_p = 3 μm and the other parameters as in Table 7.1.

The results so far indicate that a cell with grain size of several μm already gives a comparable performance to a cell with grain size of 50 μm or even several hundred μm when $L_{mono} \leq 100$ μm, as can be seen in Figure 7.6 and Figure 7.7. When L_{mono} is below 100 μm, it is therefore not crucial to aim for a fabrication method that yields grains larger than several μm. It might be more favorable to develop fabrication methods, such as LIC, that give less intra-grain defects, provided they can consistently produce grain sizes of several μm.

7.3 Poly-Si solar cells with inhomogeneous grains

A real polycrystalline solar cell consists of an assembly of grains which have an inhomogeneous distribution of grain size; in principle, the intra-grain and grain boundary properties could also be distributed inhomogeneously, but this is not considered here. With our assumption of vertical grain boundaries and no current crossing the grain boundaries, the solar cell can be modeled as a network assembly of individual solar cells or sub-cells. Each grain is represented by such a sub-cell, and modeled by (7.2.1) where all parameters are calculated as in the previous section 7.2, however with two exceptions:

1. In (7.2.3), we use L_{poly} instead of L_b, thus

$$J_{02} = \frac{q\pi D n_i V_t}{F_{max}} \frac{1}{L_{poly}^2} \tag{7.3.1}$$

   Taretto et al [11] use (7.3.1) as an approximation to the more correct (7.2.3). Doing so, it suffices to consider the value of one macroscopic quantity L_{mono} to account for the effects of intra-grain defects without assuming values of any other parameters of the cell.

2. The short circuit current is taken to be J_{sc} = 18 mA/cm^2 in all the calculations below.

In a circuit model, (7.2.1) is represented by two dark diodes and a current source that delivers the light current. We did not consider shunt conductance in the sub-cells. The p sides of all these cells are all connected to the p$^+$ BSF layer and the back contact, which we consider as a perfect conductor. The n sides of the individual cells are connected to a finger contact via either the n$^+$ emitter or the ITO layer. We assume that there is lateral current in these n$^+$ or ITO layers that is governed by a sheet resistance R_{sq}. This leads to the equivalent circuit model of Figure 7.8.

Under illumination, each sub-cell i has its own open circuit voltage $V'_{oc,i}$ short circuit current $J'_{sc,i}$, and maximum power point voltage $V_{mpp,i}$ and it carries a voltage v_i (Figure 7.8); we call these properties the 'local' V_{oc}, J_{sc}, V_{mpp} and V. One influence of the sheet resistance R_{sq} of the connecting layer is clear: if R_{sq} were zero, all sub-cells would be at the same applied voltage V. Under open circuit, this $V = V_{oc}$ would be higher than the local $V'_{oc,i}$ of the smallest grains. These grains would then consume part of the power generated by the larger grains, the latter with a local $V'_{oc,i}$ above V_{oc} of the whole cell. This detrimental effect can be masked to a large extent by a non-zero R_{sq}. We assumed, both for an n$^+$ emitter and for an ITO layer a value $R_{sq} = 70\ \Omega$ which is a rather low sheet resistance such that grain size inhomogeneity effects should be more pronounced. The contact fingers are 50 μm wide, and are placed with a periodicity of 2.5 mm

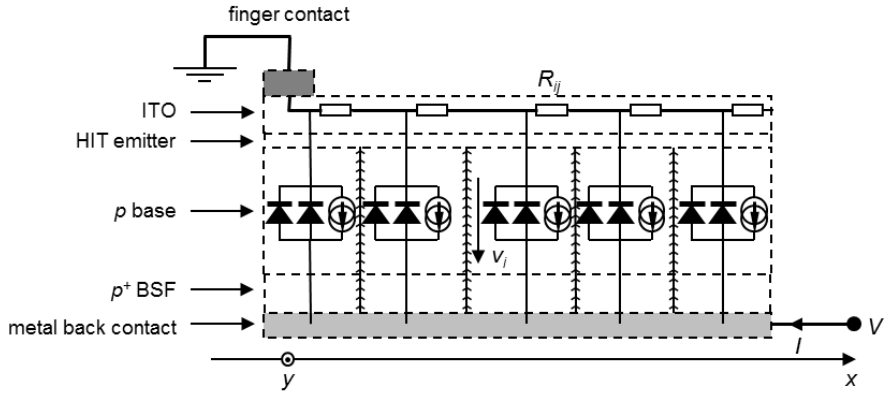

Figure 7.8: Electrical circuit model for the polycrystalline solar cell. Each grain is represented by a sub-circuit of two diodes and a current source. V is the external (applied) voltage, and v_i the voltage over sub-cell i. The resistance R_{ij} between sub-cell i and j is proportional to the sheet resistance R_{sq} of the connecting layer (here the ITO layer)

in the x-direction of Figure 7.8. Usually we consider 200 μm in the y-direction perpendicular to the plane of Figure 7.8, so our calculation area is 2500×200 μm^2. For simplicity we assume that the finger contact is transparent; however, as the contact fingers only occupy 2% of the cell area, this assumption is not severe.

To set-up the equivalent circuit we start from a given distribution of grain sizes. Like in the homogeneous case, we characterize the grain size by specifying an "effective" grain diameter, thus implicitly assuming a more or less circular shape; most reports of grain size distribution also use a grain diameter as the single parameter. Grains of different sizes are placed randomly in the plane of the cell to model the polycrystalline structure until they occupy a certain predetermined area. In our placement algorithm, a slight overlap between two grains is allowed, but not more than 1/5 of the smallest of the two grain diameters concerned. This is done to take into account that the actual shape of the grains might not be perfectly cylindrical and is rather polygonal than spherical. Two grains are electrical connected when they either overlap or are separated by a small gap only; here a gap is considered small if it is smaller than 0.25 μm or if it is smaller than 1/40 of the diameter of the largest grain of the two. The value of the resistance that then connects two grains i and j depends on the distances d_i and d_j travelled in each grain, the grain diameters g_i and g_j and R_{sq} of the connecting layer as

$$R_{ij} = R_{sq}\left(\frac{d_i}{g_i} + \frac{d_j}{g_j}\right) \tag{7.3.2}$$

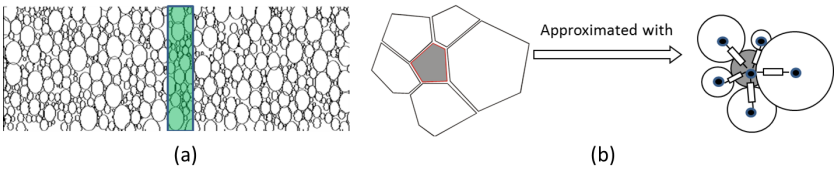

Figure 7.9: Setting up the electrical circuit. (a) Placement of cylindrical grains; the green stripe is the contact finger. (b) Neighbouring grains are connected by resistors in the connecting top layer.

These connecting resistances R_{ij} are placed between the centers of the grains. A sketch of the electrical circuit set-up described here is shown in Figure 7.9. Our placement algorithm ensures that larger grains will on average have more neighbors than smaller grains, as would be found in real situations. However, we will see that these grain placement considerations are not crucial with the assumed low sheet resistance value. The electrical circuit set-up in this way is solved with the commercial software tool Cadence.

7.3.1 Statistical sampling area; local voltage map

To obtain a statistically meaningful description of the inhomogeneity effects, we need to consider the current flow, the contact size and placements and the distribution of grain size. To understand how the current flows, we show an example of the voltage map in the ITO layer in Figure 7.10. The result is taken from a simulation of a cell with 2500×200 μm^2 area with a front finger contact in the middle, and biased at the maximum power point of the whole cell. The grains in this example cell follows an exponential distribution law for their diameter with average of $g_{av} = 5$ μm and the details will follow in the next section.

We see that there is only a significant voltage variation in the x-direction, even though the grain connection is quite random. The absence of a significant voltage variation in the y-direction indicates not only that the current is mainly travelling in the x-direction, but also that increasing the width of the cell or of the calculation area in the y-direction only serves to increase the statistical sampling. The y-width is kept at 200 μm for all our next simulations. The voltage drop ΔV over the unit cell is only a few mV, which is to be expected for this combination of low sheet resistance and low inter-finger distance [36]:

$$\Delta V = \frac{1}{3} R_{sq} l^2 J_{sc} \tag{7.3.3}$$

Where l is half of the finger period, or half of the inter-finger distance if the fingers are not transparent.

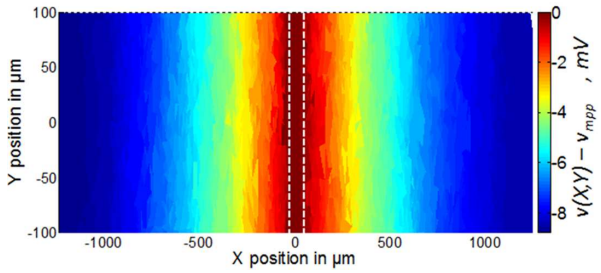

Figure 7.10: Map of the local voltage $v(x, y)$ in the connecting layer of a polycrystalline cell, biased at its maximum power point (V_{mpp}); the deviation $v(x, y)$ - V_{mpp} is shown. The cell area is $2500\ \mu m \times 200\ \mu m$ and the dashed lines around x = 0 indicate the position of the transparent finger contact. Here, the grains have diameters which follow an exponential distribution law with average of 5 μm (Figure 7.11a).

The voltage drop is small compared to the spread in V_{oc} arising from the grain size distribution and varying intra-grain diffusion conditions, which in Figure 7.4 can be seen to be in the range of 400 to 550 mV. Under these circumstances, the simulation results are hardly affected by the precise choice of the sheet resistance. The positioning of the grains is not important then, as every grain experiences about the same local applied voltage. This also means that the discrepancy between a grain's local $V_{mpp,i}$ and the applied $V = V_{mpp}$ at maximum power can be substantial. In other words, under these circumstances the smallest grains are expected to affect the total cell properties in the worst way. When the sheet resistance and/or the finger period would be substantially larger, the simulation would be in the sheet resistance regime in which the grain placement and positioning would become important. However, this simulation is less relevant as it means we would be considering a bad cell with low fill factor. The main features of the voltage map shown here are independent of the grain size distribution as long as the grains in the cell have individual area that are much smaller than the area in one finger contact period (here $50 \times 200\ \mu\text{m}^2$).

7.3.1.1 Contribution strength $Cs(g)$

The total current of the polycrystalline cell assembly determines the solar cell performance. However, a study of the local current coming in or out of each grain and of the local voltage over each grain is needed to explain the influence of a distribution of grain sizes on the total cell performance. We define here a figure of merit that we call "contribution strength" Cs, defined as:

$$Cs(g) = \frac{\sum_{i=1}^{N(g)} P_i(g)}{P_{max}} \tag{7.3.4}$$

Here, $P_i(g)$ is the power delivered by each grain with diameter g in a cell with inhomogeneous grain size distribution, and P_{max} is the total power that would be generated if the cell would only consists of identical grains with the maximum grain size available in the distribution g_{max} with the same total cell area. This contribution strength Cs basically measures the contribution of grains of size g to the power generated by a polycrystalline solar cell with a given distribution of grain sizes, normalized to a fictitious cell that only consist of grains of equal size g_{max}, the maximal g available in the distribution. Thus Cs is averaging out the local operation conditions of the sub-cell or grains with size g, i.e. how the local voltage $v(x, y)$ of a grain i with this grain size g is positioned against its local open circuit voltage $V_{oc}(g)$ and local maximum power voltage $V_{mpp}(g)$, both only depend on the grain size g and not on the position (x, y) of grain i.

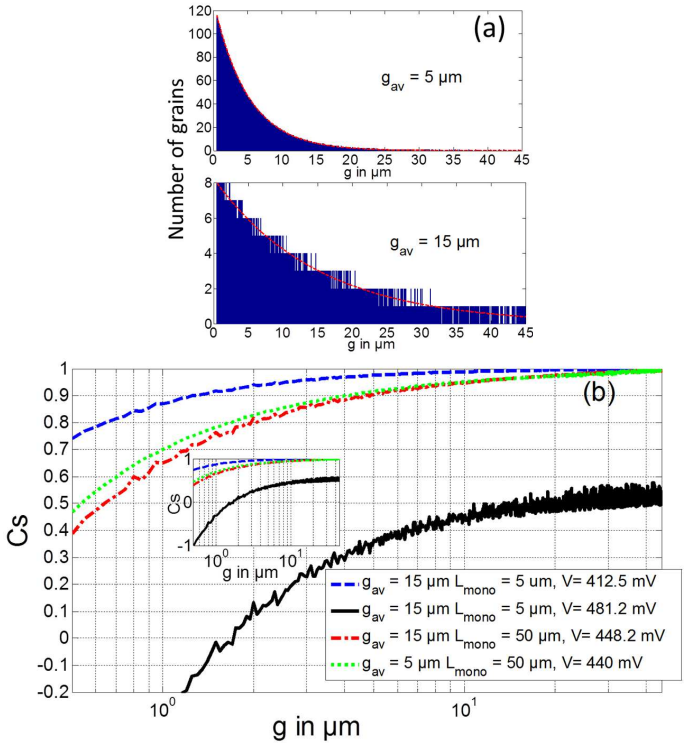

Figure 7.11: (a) The two grain diameter distributions used, one with g_{av} = 5 μm and one with g_{av} = 15 μm; the distributions are exponential. (b) The contribution strength $Cs(g)$ for cells with g-distribution as in (a). V is the voltage at which $Cs(g)$ is evaluated. In the blue, red and green curves, the cell is biased at $V = V_{mpp}$. In the black curve, the cell bias is higher than V_{mpp} = 448.2 mV, and only slightly lower than V_{oc} = 498.3 mV. The inset shows the same graph with a full Cs scale.

In Figure 7.11b we show the contribution strength $Cs(g)$ of a cell with an exponential-like distribution of the grain diameters g. Such a distribution can approximately model polycrystalline films made with the AIC method with low annealing temperature, in which there are more small grains compared to large grains [12, 13]. The g-distributions shown in Figure 7.11a follow an exponential distribution law with average diameter g_{av} = 15 μm and g_{av} = 5 μm respectively, but both are cut-off for $g < 0.5$ μm and for $g > 45$ μm. We introduced the cut-off at g_{max} = 45 μm to avoid an overly optimistic calculation dominated by a few exceptionally large grains. The introduction of the cut-off at g_{min} = 0.5 μm is motivated by the fact that the fabrication method can be controlled so that there are very few grains smaller than 1 μm [3, 32]. There are 2259 grains used in the simulation for the cell with g_{av} = 15 μm and 11665 grains for the cell with g_{av} = 5 μm.

As already shown before, the effect of grain size will become more pronounced when L_{mono} is large: compare the blue curve with the red curve in Figure 7.11b; both curves are for the same distribution with g_{av} = 15 μm. In both conditions, the cell is biased at maximum power, but the red curve with L_{mono} = 50 μm depends stronger on g than the blue curve with L_{mono} = 5 μm. This indicates for the blue curve, that the local voltage $v(x, y)$ felt by each individual grain i is close to its individual maximum power voltage $V_{mpp,i}$. The black solid curve in Figure 7.11b shows $Cs(g)$ at a bias voltage V higher than V_{mpp} and only slightly below V_{oc}. The smaller grains with $g < 1.5$ μm are seen to have a negative Cs. This is so because they are now feeling a local voltage bias above their local open circuit voltage $V'_{oc,i}$, and hence consume instead of generate power. In this case the open circuit voltage V_{oc} of the total cell will be lower than the local $V'_{oc,i}$ of the largest grains in the cell. As can be seen in the $Cs(g)$ graphs evaluated at maximum power point of the whole cell (blue, green and red curves in Figure 7.11b), larger grains have a Cs close to unity. This indicates that when the total cell is at its maximum power point, most of the larger grains are very close to their local bias $V_{mpp,i}$.

7.3.2 Grain area statistics

The results in the previous section indicate that it is more useful to consider grain area distribution than grain diameter counting. To demonstrate this we show in Figure 7.12a the area occupied by grains of different size g from the distributions in Figure 7.11a, and in Figure 7.12b the cumulative area occupation. It is seen that larger grains occupy most of the cell area for g_{av} = 15 μm. It is apparent that the statistical distribution of grain area $\pi g^2/4$ gives more direct information to predict the cell characteristics than the distribution of the grain size g itself as in the area statistics we can truly see that large grains dominate the cell occupation. Furthermore, for large grains, the local maximum power voltage is less sensitive to the grain size unlike for smaller grains as seen in Figure 7.7b for $g > 10$ μm.

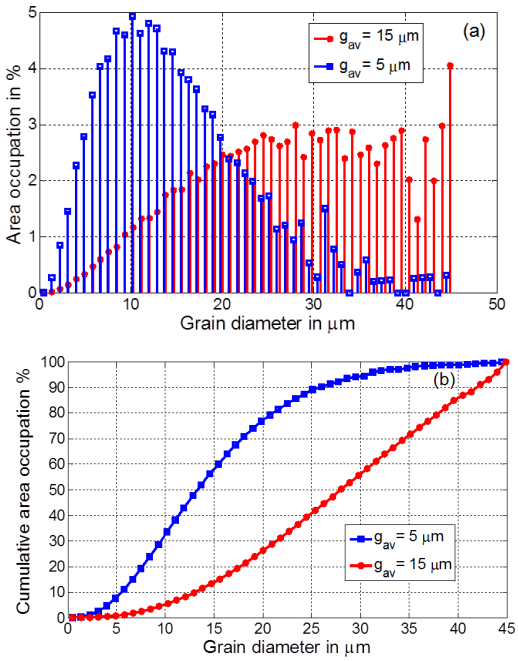

Figure 7.12: (a) Area occupation as a function of grain size g for the two distributions shown Figure 7.11(a). (b) Cumulative area occupation.

To see how strongly the smallest grains are limiting the cell, we combine the information of $Cs(g)$ calculated at V_{mpp} in Figure 7.11b with the cumulative area distribution of Figure 7.12b. By inspection of the red curve in Figure 7.11b, calculated for g_{av} = 15 μm and L_{mono} = 50 μm, we see that small grains with $g < 10\mu$m contribute less than 95% of the optimum. These suboptimal grains however occupy merely 6% of the total area (the red curve in Figure 7.12b): thus, 94% of the area is filled with grains performing better than 95% of the optimum. Combining the green curve in Figure 7.11b, calculated for g_{av} = 5 μm and L_{mono} = 50 μm, with the blue curve of Figure 7.12(b), the conclusion is that around 30% of the total area is contributing below 95% capability but less than 5% of the total area is contributing below 90%.

We come to the conclusion that even in the ”worst” circumstances studied in which grain size effect is eminent, less than 5% of the total cell area is poorly contributing to the energy production of the solar cell. Here, ”poorly” is defined as less than 90% of what the largest grains are producing. These worst circumstances are: a fairly large diffusion length $L_{mono} = 50$ μm, and a distribution containing relatively many small grains: exponential with g_{av} = 5 μm; most AIC layers exhibit a more favourable grain size distribution. Even in such conditions, the large

grains are still operating close to their optimum and the small grains are still contributing to current when the total device is biased at maximum power point. These results, together with the results of $\eta_{rel,50}$ discussed in section 7.2.4 under (7.2.8), indicate that the influence of grain size inhomogeneity will only be minor in the grain diameter range under consideration.

7.4 Characterization of poly-Si cells with n-type and p-type absorbers

C-V measurements were performed on poly-Si thin-film solar cell samples made in IMEC with both n-type and p-type absorbers to measure their apparent doping densities. arsenic (As) and boron (B) are used as dopant atoms for the n-type and p-type layers respectively. The doping densities of the samples were controled by managing the As or B containing doping gas intake in the fabrication process. These C-V measurements were done to see whether the apparent doping corresponds to the expected values and check the effect of hydrogenation on the active doping of the samples. The measurements were done with an AC voltage signal frequency of 100 kHz to minimize deeper level defect state contribution to the capacitance.

The defects in the poly-Si solar cell devices with p-type and n-type absorbers are probed with admittance spectroscopy. The type of defects in the two layers can be expected to be different as the introduced impurities are also different. Studying the defect states in the two layer types is the first step in deducing which type of layer would be best fitted for solar cells.

7.4.1 Apparent doping characteristics

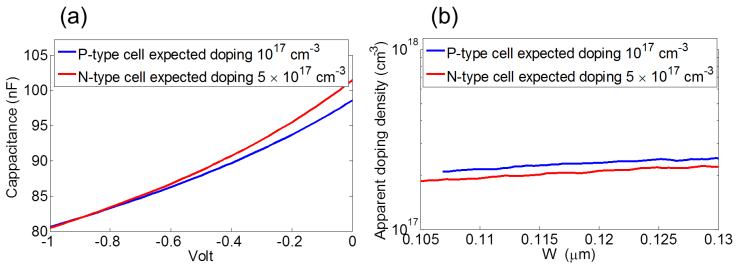

Figure 7.13: (a) Example C-V spectra of hydrogenated p-type and n-type absorber cell samples. (b) Deduced extracted doping profiles for the p-type and n-type absorber cell samples.

An example of the C-V spectra and the extracted doping profiles are shown in

Figure 7.13 for two of our samples. A fairly uniform doping profile is seen for these two samples and in fact the same is true for all the others.

Absorber type	Expected Doping in cm^{-3}	Hydrogenated	Measured Doping in cm^{-3}
p	10^{16}	no	7.41×10^{15}
p	10^{17}	no	9.26×10^{16}
p	10^{18}	no	1.19×10^{18}
p	10^{17}	yes	2.33×10^{17}
p	10^{18}	yes	9.46×10^{17}
n	10^{16}	yes	2.43×10^{15}
n	5×10^{16}	yes	1.97×10^{16}
n	5×10^{17}	yes	1.81×10^{17}

Table 7.2: Doping measurement results summary.

The extracted average doping densities taken from C-V analysis at reverse voltage for both sample types are summarized in Table 7.2. We plot Figure 7.14 to graphically depict the content of Table 7.2 for ease in reference. For cells with p-type absorbers (red data points in Figure 7.14), the measured apparent doping agrees fairly well with the expected value from gas flow control especially for the unhydrogenated samples. Hydrogenation is found to not significantly impact the active doping concentration of p-type absorber samples, though in some cells, a small increase is actually observed. Significant and consistent differences are however seen in the apparent doping density of cells with n-type absorbers(blue data points in Figure 7.14). The apparent doping is typically found to be several times smaller than the expected doping density. This reduction of apparent doping can be associated to arsenic segregation and charge trapping at grain boundaries [37, 38].

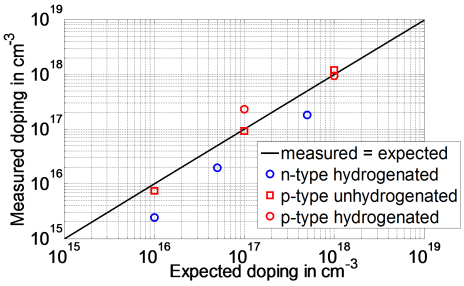

Figure 7.14: Doping density measurement results for n-type and p-type thin film polycrystalline silicon cell samples.

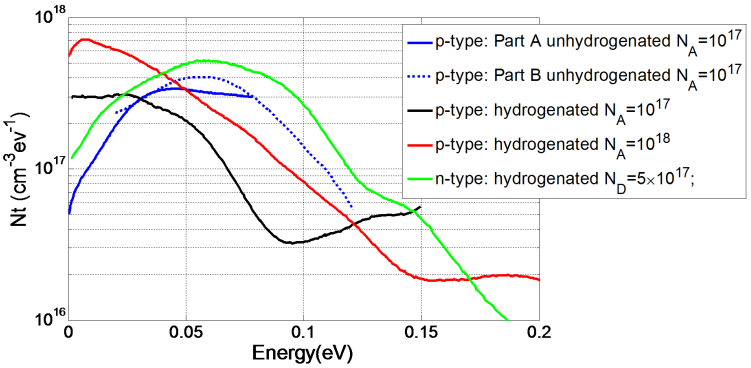

Figure 7.15: Averaged defect distribution deduced from C-f-T measurements for various solar cell samples with boron doped p-type absorber and arsenic doped n-type absorber.

7.4.2 Defect characteristics

Admittance spectroscopy measurements were done in the applied voltage frequency range of 100 Hz - 10 MHz, and temperature range of 100-360 K. The applied voltage in the measurements has an oscillation amplitude of 30 mV with zero DC bias. An example of the analysis required to deduce the defect distribution from C-f-T measurements is given in chapter 3 section 3.4 for the case of unhydrogenated poly-Si cell with p-type absorber. Here we show only the smoothed defect distribution spectra which is obtained from the raw spectra with a method described by Decock et al. [39]. Figure 7.15 shows the averaged deduced defect distribution of three p-type absorber samples with doping density of $N_A \approx 10^{17}$ cm^{-3} and $N_A \approx 10^{18}$ cm^{-3} and one n-type absorber sample with $N_D \approx 5 \times 10^{17}$ cm^{-3}. The defect distribution is deduced assuming a parabolic $E_C(x)$ behaviour in the junction, where E_C is the conduction band minimum, which is the case for our cells.

We first discuss the measured defect distribution for p-type samples with expected doping concentration 10^{17} cm^{-3} to identify the effect of hydrogen passivation. Unhydrogenated p-type samples were found to exhibit more shallow defect concentration compared to its hydrogenated counterpart in the energy range $>$ 50 meV. Note that the unhydrogenated sample exhibit two distinct defects (A and B) with different ω_{esc} but having close energy ranges as discussed in chapter 3 section 3.5. In the smoothed spectra, defect A is around 45 meV and defect B is around 55 meV. The defect A energy level matches with the expected boron doping level in Si at around 45 meV from the valence band (page 23 of [25]) and thus defect A may well be due to the boron doping level. The hydrogenated p-type samples do not exhibit a multi peak shallow trap spectrum as the unhydrogenated sample in

the energy range < 100 meV. This indicates there is effective passivation of defects by the hydrogenation process.

In general, the results show that hydrogenation can indeed reduce certain trap states in the p-type absorber poly-Si sample. However, the existence of a deeper level defect peak is hinted in the hydrogenated p-type absorber samples. One can see in Figure 7.15 a rise of defect density at higher energies for hydrogenated p-type samples (black and red curves). A clear observation of this deeper level defect is unfortunately not attainable as it requires admittance measurements at AC voltage signal frequencies lower than 100 Hz which is not accessible in our setup. It could also be that the trap concentration at higher energies is too low to be detectable by the admittance spectroscopy measurements. A complete identification of the observed defect states cannot be reached for the moment and requires more work.

The defect concentration is observed to increase along with the doping density, as can be seen by comparing the observed defect distribution of p-type absorber samples with doping densities of $N_A \approx 10^{17}$ cm^{-3} (black plot) and 10^{18} cm^{-3} (red plot). This indicates that the observed defects are connected to the dopants or the doping process, which is to be expected as dopant atom introduction also means inducing imperfections in the lattice. Note that the shapes of the defect spectra for the two absorber doping densities are similar. This indicates that there are no new defect states emerging when the doping concentration is increased. A similar trend is also seen for unhydrogenated p-type absorber samples (not shown).

The admittance spectroscopy results of hydrogenated n-type samples indicate the presence of only one main shallow defect peak around 60 meV as can be seen from the green plot of Figure 7.15. This observed defect state is close to the expected arsenic doping level in Si at 54 meV (page 23 of [25]) below the conduction band and may well be attributed to this. As for p-type samples, change of doping concentration in n-type absorber samples does not affect the shape of the observed defect distribution spectrum but only the concentration (not shown). Judging from the type of observed shallow defect states alone, the hydrogenated n-type samples can be considered to be better than p-type samples as only the doping level is observed without additional defect states.

7.5 Summary

We present here an in-depth study of thin-film poly-Si solar cells, which gives target values for recombination parameters and grain size g that should be met to obtain a targeted cell efficiency. More specifically, the target values of the most relevant parameters in dependence with other design parameters such as the base doping density and thickness, are deduced for cells with homogeneous grain properties. It is found that, with $L_{mono} \leq 100$ μm and $S_{GB} \leq 10^4$ cm/s, achieving a

larger grain size beyond several μm does not bring a significant benefit and more efforts should be dedicated instead in improving intra-grain quality. In such condtions, it is found that the discrepancy of generated power and maximum power point voltage between grains with diameter of 0.5 μm and 50 μm are roughly $\leq$ 10% even when S_{GB} = 10^5 cm/s.

The analysis was extended to poly-Si cells with exponential grain diameter distributions and realistic recombination parameters. It is found through network modelling that the small grains would still contribute to power generation while the large grains biased close to optimum at the maximum power point bias of the whole device. Our results show that grain size inhomogeneity is not expected to limit the solar cell efficiency severely. This is due to the fact that grains of different size still have similar optimum operation voltage.

Here, we also describe a comparative experimental study of thin-film poly-Si cells with boron doped p-type and arsenic doped n-type absorber layers. C-V measurements were performed to study the apparent doping concentration of the samples. C-f-T measurements were subsequently used to deduce the defect density distribution in both samples. Hydrogenation is found to be able to reduce the defect concentration in the p-type absorber cells. The p-type absorber cells exhibit more defect states than n-type cells. Judging from the type of observed defect states alone, n-type absorbers may carry more promise than p-type absorbers. More studies, however, are still needed to conclude whether p-type doping or n-type doing would be fundamentally better for the absorber layer of Si solar cells as they both carry different challenges.

References

[1] I. Gordon, D. Van Gestel, K. Van Nieuwenhuysen, L. Carnel, G. Beaucarne, and J. Poortmans. *Thin-film polycrystalline silicon solar cells on ceramic substrates by aluminium-induced crystallization*. Thin Solid Films, 487(1-2):113–117, 2005.

[2] I. Gordon, L. Carnel, D. Van Gestel, G. Beaucarne, and J. Poortmans. *8% efficient thin-film polycrystalline-silicon solar cells based on aluminum-induced crystallization and thermal CVD*. Progress in Photovoltaics, 15(7):575–586, 2007.

[3] I. Gordon, L. Carnel, D. Van Gestel, G. Beaucarne, and J. Poortmans. *Fabrication and characterization of highly efficient thin-filin polycrystalline-silicon solar cells based on aluminium-induced crystallization*. Thin Solid Films, 516(20):6984–6988, 2008.

[4] D. Van Gestel, I. Gordon, and J. Poortmans. *EBIC investigation of the influence of hydrogen passivation on thin-film polycrystalline silicon solar cells obtained by aluminium induced crystallization and epitaxy*. Solid State Phenomena, 156-158:413–418, 2010.

[5] D. Van Gestel, I. Gordon, H. Bender, D. Saurel, J. Vanacken, G. Beaucarne, and J. Poortmans. *Intragrain defects in polycrystalline silicon layers grown by aluminum-induced crystallization and epitaxy for thin-film solar cells*. Journal of Applied Physics, 105(11), 2009.

[6] D. Van Gestel, M. J. Romero, I. Gordon, L. Carnel, J. D'Haen, G. Beaucarne, M. Al-Jassim, and J. Poortmans. *Electrical activity of intragrain defects in polycrystalline silicon layers obtained by aluminum-induced crystallization and epitaxy*. Applied Physics Letters, 90(9):092103–3, 2007.

[7] G. Mathian, H. Amzil, M. Zehaf, J. P. Crest, E. Psaila, and S. Martinuzzi. *Dependence of electronic-properties of polysilicon grain-size and intragrain defects*. Solid-State Electronics, 26(2):131–141, 1983.

[8] D. Van Gestel, M. Chahal, P. C. van der Wilt, Y. Qiu, I. Gordon, J. S. Im, J. Poortmans, and Ieee. *Thin-film polycrystalline silicon solar cells with low intragrain defect density made via laser crystallization and epitaxial growth*, pages 279–282. IEEE Photovoltaic Specialists Conference. 2010.

[9] M. L. Taheri, S. McGowan, L. Nikolova, J. E. Evans, N. Teslich, J. P. Lu, T. LaGrange, F. Rosei, B. J. Siwick, and N. D. Browning. *In situ laser crystallization of amorphous silicon: Controlled nanosecond studies in the*

dynamic transmission electron microscope. Applied Physics Letters, 97(3), 2010.

[10] M. Weizman, C. Klimm, N. H. Nickel, and B. Rech. *Origin of preferential grain orientation in excimer laser-induced crystallization of silicon thin films*. Applied Physics Letters, 100(16):161906–3, 2012.

[11] C. H. Seager. *Grain-boundaries in polycrystalline silicon*. Annual Review of Materials Science, 15:271–302, 1985.

[12] C. H. Seager. *The determination of grain-boundary recombination rates by scanned spot excitation methods*. Journal of Applied Physics, 53(8):5968–5971, 1982.

[13] R. Brendel and U. Rau. *Injection and collection diffusion lengths of polycrystalline thin-film solar cells*. Solid State Phenomena, 67-8:81–86, 1999.

[14] K. Taretto, U. Rau, and J. H. Werner. *Method to extract diffusion length from solar cell parameters—Application to polycrystalline silicon*. Journal of Applied Physics, 93(9):5447–5455, 2003.

[15] E. Pihan, A. Slaoui, and C. Maurice. *Polysilicon films formed on alumina by aluminium induced crystallization of amorphous silicon*. Materials Research Society Symposium Proceedings, 2006.

[16] O. Tüzün, J. M. Auger, I. Gordon, A. Focsa, P. C. Montgomery, C. Maurice, A. Slaoui, G. Beaucarne, and J. Poortmans. *EBSD analysis of polysilicon films formed by aluminium induced crystallization of amorphous silicon*. Thin Solid Films, 516(20):6882–6887, 2008.

[17] M. Imaizumi, T. Ito, M. Yamaguchi, and K. Kaneko. *Effect of grain size and dislocation density on the performance of thin film polycrystalline silicon solar cells*. Journal of Applied Physics, 81(11):7635–7640, 1997.

[18] V. G. Karpov, A. D. Compaan, and D. Shvydka. *Random diode arrays and mesoscale physics of large-area semiconductor devices*. Physical Review B, 69(4), 2004.

[19] S. Gall, J. Schneider, J. Klein, M. Muske, B. Rau, E. Conrad, I. Sieber, W. Fuhs, D. Van Gestel, I. Gordon, K. Van Nieuwenhuysen, L. Carnel, G. Beaucarne, J. Poortmans, M. Stoger-Pollach, and P. Schattschneider. *Large-grained polycrystalline silicon thin-film solar cells using AIC seed layers*, pages 975–978. IEEE Photovoltaic Specialists Conference. 2005.

[20] A. Focsa, A. Slaoui, E. Pihan, F. Snijkers, P. Leempoel, G. Beaucarne, and J. Poortmans. *Poly-Si films prepared by rapid thermal CVD on boron*

and phosphorus silicate glass coated ceramic substrates. Thin Solid Films, 511:404–410, 2006.

[21] A. Straub, D. Inns, M. L. Terry, Y. Huang, P. I. Widenborg, and A. G. Aberle. *Optimisation of low-temperature silicon epitaxy on seeded glass substrates by ion-assisted deposition*. Journal of Crystal Growth, 280(3-4):385–400, 2005.

[22] J. H. Wang, S. Y. Lien, C. F. Chen, and W. T. Whang. *Large-Grain Polycrystalline Silicon Solar Cell on Epitaxial Thickening of AIC Seed Layer by Hot Wire CVD*. IEEE Electron Device Letters, 31(1):38–40, 2010.

[23] A. Abass, D. Van Gestel, K. Van Wichelen, B. Maes, and M. Burgelman. *On the diffusion length and grain size homogeneity requirements for efficient thin-film polycrystalline silicon solar cells*. Journal of Physics D: Applied Physics, 46(4):045105, 2013.

[24] P. A. Basore. *Extended spectral-analysis of internal quantum efficiency*, pages 147–152. IEEE Photovoltaic Specialists Conference. IEEE, New York, 1993.

[25] S. Sze and K. K. Ng. *Physics of semiconductor devices*. Wiley & Sons, 3rd edition, 2007.

[26] S. Adachi. *Optical constants of crystalline and amorphous semiconductors*. Kluwer Academic Publishers, Boston, 1999.

[27] M. Green. *Silicon solar cells - Operational Principles, technology and System Applications*. The University of South Wales, 1998.

[28] R. Hulstrom, R. Bird, and C. Riordan. *Spectral solar irradiance data sets for selected terrestrial conditions*. Solar Cells, 15(4):365–391, 1985.

[29] S. Selberherr. *Analysis and Simulation of Semiconductor Devices*. Springer Verlag, 1984.

[30] D. A. Antoniadis, A. G. Gonzalez, and R. W. Dutton. *Boron in near-intrinsic (100) and (111) silicon under inert and oxidizing ambients - diffusion and segregation*. Journal of the Electrochemical Society, 125(5):813–819, 1978.

[31] N. D. Arora, J. R. Hauser, and D. J. Roulston. *Electron and hole mobilities in silicon as a function of concentration and temperature*. IEEE Transactions on Electron Devices, 29(2):292–295, 1982.

[32] D. P. Bhatt and D. P. Joshi. *Theoretical study of the influence of doping concentration on the performance of polycrystalline silicon solar cells*. Journal of Applied Physics, 71(9):4594–4603, 1992.

[33] T. Kojima, Y. Ohshita, T. Tachibana, A. Ogura, and M. Yamaguchi. *Electrical properties and boundary structures in cast-grown polycrystalline silicon*. In Photovoltaic Specialists Conference (PVSC), 2010 35th IEEE, pages 001419–001422, 2010.

[34] P. Panayotatos, E. S. Yang, and W. Hwang. *Determination of the grain-boundary recombination velocity in polycrystalline silicon as a function of illumination from photoconductance measurements*. Solid-State Electronics, 25(5):417–422, 1982.

[35] K. Nishioka, T. Yagi, Y. Uraoka, and T. Fuyuki. *Effect of hydrogen plasma treatment on grain boundaries in polycrystalline silicon solar cell evaluated by laser-beam-induced current*. Solar Energy Materials and Solar Cells, 91(1):1–5, 2007.

[36] A. De Vos and P. De Visschere. *Diagnosis of a large distributed series resistance in solar cells*. Solar Cells, 10(1):12, 1983.

[37] C. Y. Wong, C. R. M. Grovenor, P. E. Batson, and D. A. Smith. *Effect of arsenic segregation on the electrical properties of grain boundaries in polycrystalline silicon*. Journal of Applied Physics, 57(2):438–442, 1985.

[38] B. Swaminathan, E. Demoulin, T. Sigmon, R. Dutton, and R. Reif. *Segregation of Arsenic To the Grain-Boundaries in Polycrystaline Silicon*. Journal Of The Electrochemical Society, 127(10):2227–2229, 1980.

[39] K. Decock, S. Khelifi, and M. Burgelman. *An automated method to reduce noise of admittance spectra allowing assessment of a large number of complicated spectra*. In EU PVSEC Proceedings, pages 2922–2925. WIP Wirtschaft und Infrastruktur. Planungs KG, 2011.

8
Conclusions and outlook

8.1 Conclusions

In the photonics part of our work we showed how coupling various photonic components and phenomena can achieve a certain goal. Conflicting requirements for certain functionalities can be untangled. This was demonstrated in the context of enhancing both light absorption and emission.

First, we discussed the challenges one faces in achieving a broad band absorption enhancement, in which multiple photonic phenomena are needed to cover the broad wavelength range of interest. If possible one would wish to excite as many absorption enhancing photonic phenomena as possible: waveguide modes, scattering, Fabry-Perot effects for field enhancement and antireflection effects, and plasmonic modes. Often, the requirements for optimum excitation of one mode can be at the expense of another. Even more troubling, there are already conflicting requirements to excite the same type of resonance in different wavelength ranges. To alleviate these problems we propose the usage of combined gratings and diffuser-grating structures. The former enhances absorption by relying on guided mode excitation, while the latter focusses on antireflection and scattering management. In such structures, we split the responsibility of different optical components, enabling more flexibility in optimizing each.

Different variants of the dual interface grating structures were explored. One main point of discussion is the light trapping capability of multiperiodic dual interface gratings, which have a rich Fourier spectrum, while maintaining a straight-

forward geometry. In effect, multiperiodic DIGs can be tailored to give stronger coupling to higher-order guided modes, without sacrificing the coupling efficiency to lower order modes. Moreover, inducing a weak blazing in a triangular DIG system was shown to open access to dark modes with very high coupling efficiency at normal incidence, without sacrificing the absorption at other wavelengths and at larger angles. Blazing of the front and back grating provides specific access to guided modes, e.g. blazing at the front dominantly influences the dielectric waveguide modes and not the plasmonic mode at the back contact. Weakly blazed DIG structures can outperform their symmetric counterparts throughout a broad angle of incidence range.

To efficiently address combined diffuser-grating structures, we developed the one pass coherent (OPC) calculation method, which can also handle more general structures with other wave and ray optics segments. The OPC calculations take wave effects into account where they matter the most, while evading a large computational domain to model rough structures. A general rough diffuser is handled directly via the reflected wavefront instead of its geometry. A single plane wave calculation sweep provides all the information to calculate any kind of bottom diffuser or even any kind of ray optics segment. Combined front grating-back diffuser structures have stronger light trapping capabilities than single element devices in an important range of active material thicknesses.

With the OPC method, we also demonstrate that limited coherence can lead to a stronger absorption on average over a fairly broad wavelength range for an important range of Si thicknesses. A loss of phase relation between waves incoming and waves reflected from the back in effect exchanges a discrete set of leaky waveguide states in the active material film with a broadband continuum of allowable states. Though one loses the strong absorption provided by leaky guided modes at resonant wavelengths, a more broadband absorption enhancement becomes possible and can on average improve the absorption performance. Therefore, the back reflector in advanced thin-film devices needs careful consideration.

In the context of light emission we study the nature of hybrid plasmonic-photonic modes in metallic nanoantenna arrays arising from the interaction between the localized surface plasmon resonance (LSPR) of the individual nanoparticles and the Rayleigh anomaly (RA) diffraction or waveguide mode. Numerical simulations were done for driven and undriven systems, with the latter revealing the SLR eigenmode properties for the first time. Such hybrid modes give rise to much interest, since desirable attributes of the interacting bare resonances can be mixed in the hybrid resonance. One can in effect have a mode with a relatively strong near field enhancement while maintaining an extended field distribution and low loss. The dispersion, linewidth, and associated stop-gap of a hybrid plasmonic-photonic mode was shown to be widely tunable by controlling the energy detuning between the interacting bare resonances. This energy detuning can

be controlled through the geometry of the nanoantennas. In the case of plasmonic surface lattice resonances (SLRs), both the radiative loss and the near field confinement (and thus ohmic loss) are enhanced as the LSPR energy approaches the RA energy. Depending on their momentum SLRs may have more than one radiative decay channel.

We further proceed to demonstrate active tuning of the emission enhancement resonance wavelength and directionality provided by a hybrid plasmonic-photonic mode. The hybrid mode in question arises from the interaction between a thin QD layer film with an aluminum nanodisk array placed on top of the layer. This system supports radiative coupling between the LSPR of each nanodisk and a waveguide mode in the quantum dot emitter layer resulting in the hybrid mode. The tunability was achieved by covering the array with liquid crystal (LC) molecules whose orientation can be tuned via a voltage or temperature change. By controlling the LC molecule orientation, one can thus control the refractive index of the LC layer. The dispersion, linewidth, and excitation strength of this hybrid mode are all affected by the LC molecule orientation, which we control via temperature. We show that the tuning depends on the relative orientation of the dominant mode polarization with the LC optical axis.

In the electrical part of our work, we provide an in-depth study of thin-film poly-Si solar cells, which gives target values for recombination parameters and grain size g that should be met to obtain a targeted cell efficiency. More specifically, the target values of the most relevant parameters in dependence with other design parameters (such as the base doping density and thickness) are deduced. It is found that, with $L_{mono} \leq 100$ μm and $S_{GB} \leq 10^4$ cm/s, achieving a larger grain size beyond several μm does not bring a significant benefit, and more efforts should be dedicated instead on improving intra-grain quality. Simulations of cells with exponential grain diameter distributions and realistic recombination parameters were done through network modelling to examine the performance of each individual grain under nonhomogeneous conditions. It is found through network modelling that the small grains would still contribute to power generation while the large grains biased close to optimum at the maximum power point bias of the whole device. Our results show that grain size inhomogeneity is not expected to severely limit the solar cell efficiency.

A comparative experimental study was also done on thin-film poly-Si cells with boron doped p-type and arsenic doped n-type absorber layers. C-V measurements were performed to study the apparent doping concentration of the samples. C-f-T measurements were subsequently used to deduce the defect density distribution in both samples. Hydrogenation is found to be able to reduce the defect concentration in the p-type absorber cells. The p-type absorber cells exhibit more defect states than n-type cells. Judging from the type of observed defect states alone, n-type absorbers may carry more promise than p-type absorbers.

8.2 Outlook and future work

Different light trapping strategies were presented that involve combinations of various photonic elements. These studies can be used as a stepping stone to develop an optimized structure suitable for diverse solar cell materials. For practical purposes, full 3D structures should be considered. Though most of the calculations done here are for 2D structures for a single polarization, the physics behind the interaction between different components is adequately described and can be used as guidelines for the optimization.

Simultaneous usage of various photonic phenomena to boost absorption, which also involves plasmonic modes, was demonstrated. To date, however, using plasmonic near field enhancement to enhance absorption does not optimally translate to increase of photocurrent due to the carriers being generated relatively close to the metal surface. Surface recombination near the metal interface has traditionally been avoided by introducing a thin back surface field (BSF) layer, which has a very high doping. Due to the high doping however, carriers generated in the BSF region also quickly recombine. Thus having a BSF near a patterned metal back contact does little to improve the translation of plasmonic near field absorption enhancement to an increase of photocurrent. Direct proper passivation of the metal/active material interface is of great importance and remains a hard challenge. Much research still needs to be done to tackle this challenge.

The developed OPC calculation method provides an efficient way to accurately handle structures with both wave and ray optics components. This method can also be used to study and optimize LED structures that have components with similar characteristics. We envisage the usage of this method for optimizing the outcoupling of light in such LED structures.

The current designs of DIGs presented in chapter 4 have a small geometrical error tolerance. This is an inherent problem one encounters when utilizing resonant photonic phenomena with relatively sharp linewidths. The coupling efficiency to leaky guided modes is found to be sensitive to the relative orientation of the top and bottom grating and the tilt of the blazed gratings. Different relative orientation of the top and bottom gratings may lead to less modes being excited efficiently. One possible remedy of this small geometrical tolerance is to have more photonic resonances available in the targeted wavelength range for absorption enhancement. A decrease of coupling efficiency to one leaky guided mode resonance can be compensated by the presence of another resonance. Research on more geometrically insensitive designs of DIG structures will be of great importance for the practical realization of commercial solar cells with DIG structures.

Unlike the DIGs, light trapping with combined grating and diffuser structures discussed in chapter 5 have less geometrical tolerance problems. This is so as grating-diffuser structures do not rely on resonant photonic phenomena to enhance

absorption. Imperfections of the top grating geometry may lead to changes in the efficiency of different diffraction orders and anti-reflection properties. However, one will still obtain similar scattering characteristics even if there is a significant change from the intended shape.

The work on hybrid plasmonic-photonic modes demonstrates the vast possibilities in tailoring their properties by simple geometrical design, providing insight into the interplay between the bare resonances. The results can be used as grounds for further research on the applications of such hybrid modes for different purposes such as sensing, lighting and lasers. We have also established for the first time the suitability of these modes for active control of light-emission enhancement. Further improvements of the tuning capability and enhancement factors can still be achieved by tailoring the field overlap with the liquid crystal and emitter layer. The utilization of different LCs with larger contrast between the extraordinary and ordinary index can also help to increase the tuning range. With temperature tuning demonstrated we further envisage the implementation of a voltage tuning mechanism on the structure, which is the next step towards smart lighting applications.

The simulation work on poly-Si grains currently assumes that the grains are not lumped on top of each other and thus that the grain boundaries are all oriented vertically. This may not be possible for all fabrication techniques, especially for thicker cells. Simulations of cells with horizontally oriented grains, with current being able to travel through the grain boundaries, will also be of interest.

In addition, more studies are needed to determine whether p-type doping or n-type doping in the absorber layer would be fundamentally better for Si solar cells as they both carry different challenges. In particular, one still needs to determine the nature of the observed defects and the dominant carrier recombination processes.